Order Number 8805691

Interannual variability of the California Current System: A numerical model

Pares-Sierra, Alejandro, Ph.D.

The Florida State University, 1987

U·M·I
300 N. Zeeb Rd.
Ann Arbor, MI 48106

PLEASE NOTE:

In all cases this material has been filmed in the best possible way from the available copy. Problems encountered with this document have been identified here with a check mark __✓__.

1. Glossy photographs or pages _____
2. Colored illustrations, paper or print _____
3. Photographs with dark background _____
4. Illustrations are poor copy __✓__
5. Pages with black marks, not original copy _____
6. Print shows through as there is text on both sides of page _____
7. Indistinct, broken or small print on several pages __✓__
8. Print exceeds margin requirements _____
9. Tightly bound copy with print lost in spine _____
10. Computer printout pages with indistinct print _____
11. Page(s) _____ lacking when material received, and not available from school or author.
12. Page(s) _____ seem to be missing in numbering only as text follows.
13. Two pages numbered _____. Text follows.
14. Curling and wrinkled pages _____
15. Dissertation contains pages with print at a slant, filmed as received __✓__
16. Other _____

_____

_____

THE FLORIDA STATE UNIVERSITY

COLLEGE OF ARTS AND SCIENCES

INTERANNUAL VARIABILITY OF THE CALIFORNIA CURRENT SYSTEM: A NUMERICAL MODEL

by

ALEJANDRO PARES-SIERRA

A Dissertation submitted to the
Department of Oceanography
in partial fulfillment of the
requirements for the degree of
Doctor of Philosophy

Approved:

James J. O'Brien
Professor Directing Dissertation

George Weatherly

Christopher Tam

Joseph W. Winchester

C. J. Clarke

W. Sturges
Chairman, Department of Oceanography

Fall, 1987

ABSTRACT

A reduced gravity model that incorporates the geometry of western North America has been used to study the dynamics of the California Current System (CCS). Three experiments were implemented: first the model was run using 19 years of wind stress from the Comprehensive Ocean-Atmosphere Data Set (local model); a second experiment (remote model) consisted of forcing the model through its southern boundary using the results of a similar reduced gravity equatorial model; in a third experiment, both forcings were used simultaneously (local+remote model). The main objective of this work was to analyze the low frequency variability on the CCS in terms of its contributions from remote and local forcing.

Away from the coast, the basic state of the model is determined by the predominantly negative wind curl through an Sverdrup balance. The general seasonal cycle (eg. set-up of Davidson Current, formation and position of Southern California eddy, etc.) is in agreement to what has been described by other authors. Through cross correlation and cross spectral analysis between the model results and observed sea-level data, it was established that most of the interannual variability in sea-level height at the coast is due to disturbances of equatorial origin that propagate into the region in the form of coastally trapped Kelvin waves. For the annual frequency variability,

on the other hand, it was found that both local, as well as remotely forced variability, contribute to the total variance.

A Paco y Luci

A Irma

ACKNOWLEDGEMENT

This work was supported by the National Science Foundation grant OCE-84-15986. Additional support was provided by the Consejo Nacional de Ciencia y Tecnologia of Mexico.

I wish to express my deep gratitude to Dr. James J. O'Brien, my major professor and thesis advisor. His guidance, motivation and support throughout the course of this research are sincerely appreciated. I am also grateful for the time taken by Drs. Christopher K. Tam, Georges L. Weatherly, John W. Winchester and Allan J. Clarke while serving on my doctoral committee. Thanks are extended to Dr. K. Wyrtki for providing the sea level data used to validate our model. This study would have been impossible without such data. Computations were performed on the Florida State University's Cyber 205 Supercomputer. Portions of the computer time were granted by the Florida State University Computer Center.

I also wish to thank my colleages at the Mesoscale Air-Sea Interaction Group for their useful comments and suggestions. Special thanks go to Dr. Mark Luther for his help during the initial stages of the model development and the many hours of enlightening discussion. Also, I wish to thank Mr. James Merritt whose help was vital to the solution of many computer problems. I also thank Rita Kuÿper who typed the different versions of this thesis with skill and patience.

To Edgar Pavia, Manuel Lopez, Irma Olguin and all my friends at the Florida State University, thanks for their help and for making my stay at Florida State University and Tallahassee a most enjoyable and unforgettable one.

Finally, it is with the deepest affection that I thank my parents and my wife Irma for their patience, love and unconditional support.

TABLE OF CONTENTS

LIST OF TABLES

LIST OF FIGURES

I. INTRODUCTION

a) Motivation and Objectives

During the 1982-1983 El Niño event, waters several degrees warmer than normal were observed at the Northeastern Pacific Ocean. The biological and economic implications of this phenomenon are enormous. The distribution and abundance of fish and invertebrates changed remarkably in the coastal waters of the Northeastern Pacific Ocean (NEPO) (Wooster and Fluharty, 1985). Pearcy and Schoener (1986) for example, report the appearance in the waters of Oregon and Alaska of thirteen marine species that had never before been reported north of California. Simpson (1984a) showed that the anomalous warm waters in the California Current during August 1982 were accompanied by negative salinity anomalies as well as oxygen anomalies. Although it is accepted that the 1982-1983 episode was an exceptionally strong El Niño (eg. Pearcy and Schoener, 1986), it certainly was not an isolated phenomenon. Other anomalous warm events have been observed, for example in 1940-41, 57-58, 1969, 1972 (Enfield and Allen, 1980; Quinn et al, 1984), and linked to tropical El Niño-SO phenomenon.

In recent years, a great amount of research relevant to the interannual oceanic variability in the northeastern Pacific has been done (eg. Enfield and Allen, 1980; Chelton and Davis, 1982; Christensen et al., 1983; Simpson, 1984 among others). In spite of

all this work, fundamental questions about the generation of this variability still remain unanswered in the literature.

Emery and Hamilton (1985) cite two basic ways to explain the connection between the anomalous warming of the northeastern Pacific Ocean and the tropical El Niño phenomenon, one oceanic and the other atmospheric.

For the first, poleward propagating waves generated in the tropics during an ENSO episode carry the information to the extratopical regions. Theoretical works of Moore (1968), Anderson and Rowlands (1976), and Clarke (1983), have demonstrated that an equatorial wave can generate, upon reflecting on an eastern boundary, a poleward propagating water disturbance in the form of coastal Kelvin waves. Observational evidences (eg. Enfield and Allen, 1980; Chelton and Davis, 1982) suggest that much of the oceanic low frequency variability along the western coast of North America can be accounted for by this mechanism.

A second, nonexclusive explanation for the co-occurrence between equatorial and mid-latitude anomalies invokes an atmospheric teleconnection (Emery and Hamilton, 1985). Under this hypothesis, first presented by Bjerkness (1966), an atmospheric link is achieved between the tropical Pacific SST anomalies and the mid-latitude Pacific anomalies via a momentum transfer from a variable Hadley cell. A number of observations and theoretical studies supports the importance of such an interaction (eg. Namias, 1976; Emery and

Hamilton, 1985; Simpson, 1983, 1984a, b). For the California Current region in particular, Simpson (1983, 1984a, b) concluded that the intensification and expansion of the Aleutian low and the decrease in strength of the Pacific high directly produced, through an enhanced basin wide atmospheric circulation, some of the Californian El Niños, especially the 1940-41 and 1982-83.

The main objective of this thesis is to investigate the dynamics of the California Current system and its oceanic connection with the equatorial region, not only in its anomalous El Niño state, but also the regular average circulation. This research helps to answer questions such as: how much of the interannual variability in the NEPO is due to variability in the local forcing (either in the wind stress or its curl) and how much is due to equatorial variability propagated to the region as equatorial-coastal Kelvin waves? In other words, is the observed coherence in the interannual frequency band between the NEPO and the equatorial ENSO events due to atmospheric or oceanic teleconnections or both? How much of the low frequency energy found (in sea surface temperature time series, for example) in the north Pacific comes from the eastern coast radiated to the region as planetary waves, and what part of this was generated at the coast by the variation of the wind stress compared to relaxation of coastally transmitted equatorial disturbances?

The thesis is divided into 6 chapters. A brief review of the climatology of the California Current is given in the next section.

The model and its numerical implementation, boundary conditions, and characteristics of the forcing are explained in the second chapter. In the third chapter we present a simple theory of the dynamics of the circulation on an eastern boundary in general and its application in particular to the California Current. In the fourth chapter, general results of the numerical model are presented; large scale mean maps of upper layer thickness and current are given in this chapter. Comparison of model results with observations in the annual and interannual frequency range and evidence of westward relaxation of coastal disturbances are also given in chapter IV. A summary of the results is presented in chapter V, while in chapter VI the results are discussed and the conclusions presented.

b) The California Current System

The California Current (CC) is a wide and slow current that flows in a general north-east to south-west direction following the coast of northwestern America. Its average speed is typically less than 25 cm/s (Reid and Schwartzlose, 1962). The CC is the eastern limb of the anticyclonic north Pacific gyre, and as such it is the north Pacific representative of an Eastern Boundary Current (EBC). Other EBC are the Peru and Chile Currents, the Canary Current and the Benguela Current. A review of EBC and its associated upwelling regions was given by Wooster and Reid (1963), who examined its common features in terms of source water, surface characteristics and upwelling phenomenon resulting from local atmospheric circulations and the

presence of a boundary. There is a considerably large range of time and length scales associated with the variability of an EBC system, from fine structure (eg. Bang and Andrews, 1974) to very larger scale interannual variability (eg. Enfield and Allen, 1980; Chelton and Davis, 1982; Christensen et al., 1983). A general comprehensive theory of EBC is not available, but a summary of the various aspects that have been studied is presented by Gill (1982).

The California Current System, (CCS) is probably the EBC that has been most studied and monitored; the California Cooperative Oceanic Fisheries Investigations (CalCOFI) program has been systematically monitoring it since 1949. Early description of the CCS was given by Sverdrup et al. (1942) and Reid et al. (1958). A recent and more detailed description of its characteristics is that of Hickey (1979), since then reviews of different aspects and time scales have been made by numerous authors. McCreary et al. (1987) studied the dynamics of the CCS using two ocean models, one with shelf and one without.

The CC (an equatorward flow, see Fig. 1) together with the Davidson Current (a poleward countercurrent that occurs near the coast) and the California undercurrent (a poleward underflow over the continental slope) form the CCS (Hickey, 1979). Hickey (1979); shows that the strongest equatorward flow (CC) appears in spring and summer, whereas the strongest poleward coastal counterflow (IC) appears in fall and winter. During spring and early summer the prevailing winds near the north American coast are north-northwesterly, giving rise to

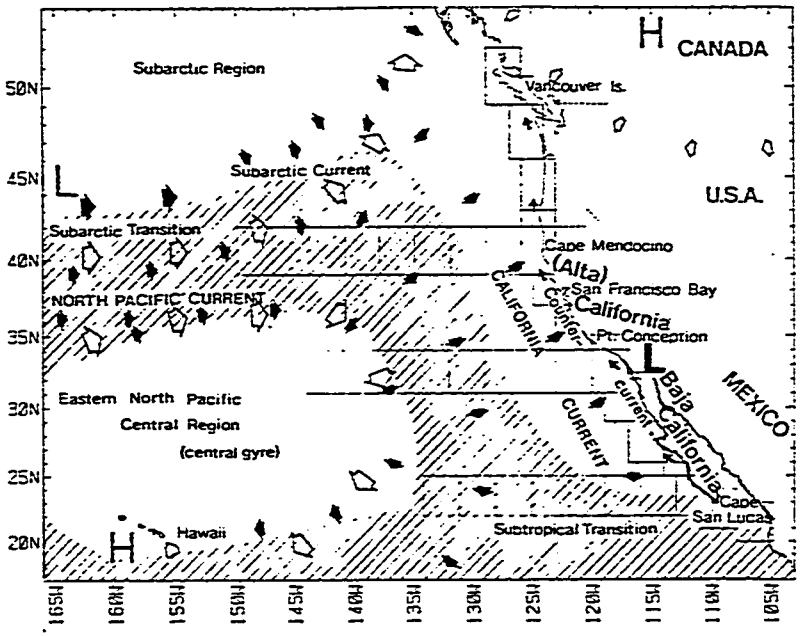

Fig. 1: Schematic representation of the northeastern Pacific Ocean climatology showing surface winds (open arrows), surface currents (solid arrows), and dominant atmospheric pressure systems: Aleutian low, North Pacific High, Californian continental thermal low, and the North American High (from Norton et al., 1985).

upwelling events that on the average and with characteristic spatial variability, last from March to July (Sverdrup et al., 1942). In areas of intense upwelling the spring water temperature is even lower than that of winter. Earlier studies have shown that, from these areas of intense upwelling, tongues of cold waters emanate in a southwardly direction moving rich coastal water to the ocean interior (Hickey, 1979). Some theoretical studies suggest that the mechanism for the relaxation of the cold upwelling region is in the form of westward radiation of Rossby waves (eg. McCreary, 1976; Mysak, 1983).

Towards the end of the summer, due to changing wind directions, the upwelling gradually ceases, the cold tongues break away in the form of small eddies that sometimes carry coastal waters very far from the coast (Hickey, 1979). After upwelling ceases in the fall, a surface layer countercurrent develops (the Davidson or Inshore countercurrent) which in November, December, and January runs north along the coast to at least latitude 48°N (Sverdrup et al., 1942).

In addition to this annual cycle, an interannual variability of anomalous cold or warm years occurs, an example of which is the record breaking event of 1982-1983. Although there are several possible causes for the interannual variability in an EBC (eg. Gill, 1982; pp. 425-428) two mechanisms seem the most important: local anomalous Ekman pumping and remotely forced equatorial-coastal Kelvin waves. In section III a brief review of the mechanisms for EBC variability is presented.

II. THE MODEL

a) Model Description

We used a non-linear, reduced gravity model in spherical coordinates to model the California Current system. The model consists of one dynamically active layer of density ρ and depth H (see Fig. 2) on top of an infinitely deep layer of slightly higher density $\rho+\Delta\rho$, the interface between these two layers being a proxy of the ocean pycnocline. The equations were used in the transport mode to facilitate some of the numerical implementation. It was more convenient to use spherical coordinates, due to the large latitudinal extent of the model and since the forcing function as well as the coordinates defining the boundaries were given in degrees of latitude and longitude. The equations defining the model are:

$$\frac{\partial U}{\partial t} + \frac{1}{a\cos\theta}\frac{\partial}{\partial\phi}\left(\frac{U^2}{H}\right) + \frac{1}{a}\frac{\partial}{\partial\theta}\left(\frac{UV}{H}\right) - (2\Omega\sin\theta)V$$

$$= \frac{-g'}{2a\cos\theta}\frac{\partial H^2}{\partial\phi} + \frac{\tau^{\phi}}{\rho} + A\nabla^2 U \qquad 1.a$$

$$\frac{\partial V}{\partial t} + \frac{1}{a\cos\theta}\frac{\partial}{\partial\phi}\left(\frac{UV}{H}\right) + \frac{1}{a}\frac{\partial}{\partial\theta}\left(\frac{V^2}{H}\right) + (2\Omega\sin\theta)U$$

$$= \frac{-g'}{2a}\frac{\partial H^2}{\partial\theta} + \frac{\tau^{(\theta)}}{\rho} + A\nabla^2 V \qquad 1.b$$

and

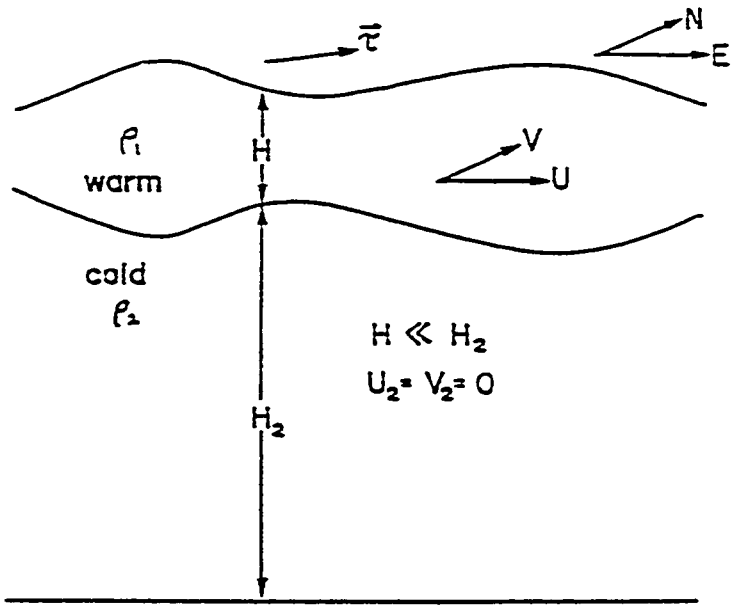

Fig. 2: Typical geometry for a reduced gravity model ($H \ll H_2 \to \infty$). Only the top layer is dynamically active.

$$\frac{\partial H}{\partial t} + \frac{1}{a \cos\theta}\left\{\frac{\partial U}{\partial \phi} + \frac{\partial}{\partial \theta}(v \cos\theta)\right\} = 0 \qquad 1.c$$

where θ, ϕ are the latitude and longitude respectively; U, V are the transport [i.e. $(U,V) = H(u,v)$] in the east-west and north-south direction respectively; H is the depth of the upper layer; $g' = \frac{\Delta\rho}{\rho} g$ is the reduced gravity; $(\tau^{\theta},\tau^{\phi})$ are the wind stresses applied throughout the upper layer as a body force; A is an eddy viscosity coefficient; a the radius of the earth; and Ω the angular velocity of rotation of the earth. The values used for each coefficient are given in appendix A. This model had been used before to simulate the wind driven circulation in the Indian Ocean (Luther et al., 1985) and the equatorial Pacific (Kubota and O'Brien, 1984). Equations 1 were solved numerically on a 301 x 220 grid covering the northeastern Pacific Ocean from 18°N to 50°N and from 155°W to the American west coast (see Figure 3). The equations were discretized into a staggered grid (Arakawa C-grid) as shown in Figure 4. This arrangement of variables reduces by 1/4 the amount of storage used, while maintaining a good resolution. A 1/12 of a degree resolution was used in both zonal and meridional directions.

A leap-frog scheme was used for the time integration with 20 minute time steps. Every 99th time step, a forward time differencing was employed to avoid the computational mode. The viscous terms were treated using a DuFort-Frankel scheme. The non-linear and the Coriolis terms were averaged using adjacent points to get values at

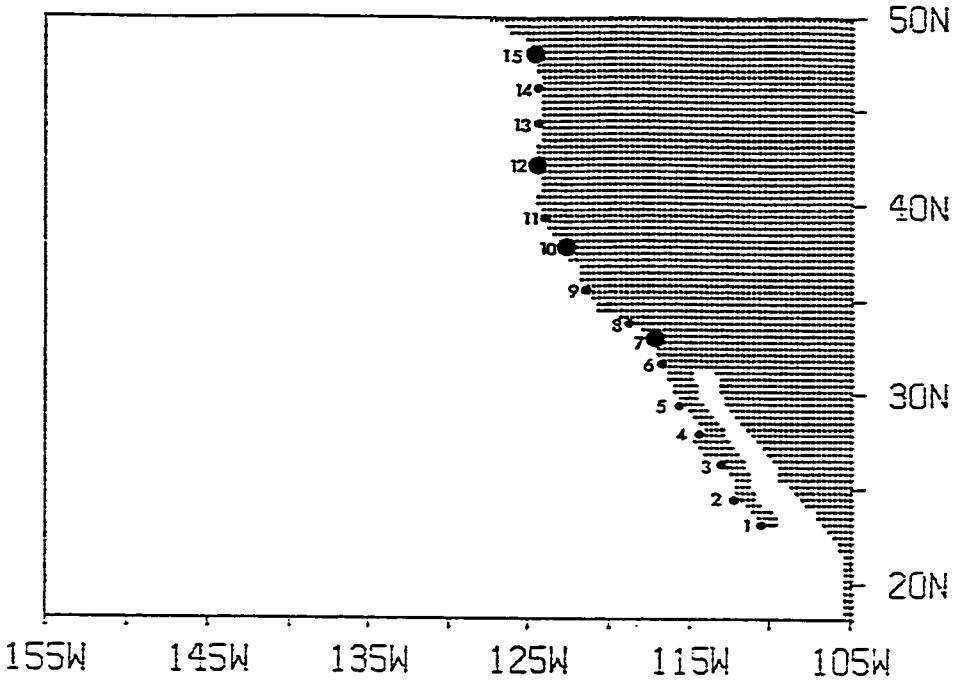

Fig. 3: Model domain. The western, northern and southern boundaries are open. Dots mark the location of the station used by the alongshore variation analysis (# identified in table 1). Larger dots mark the stations used in the westward propagation analysis.

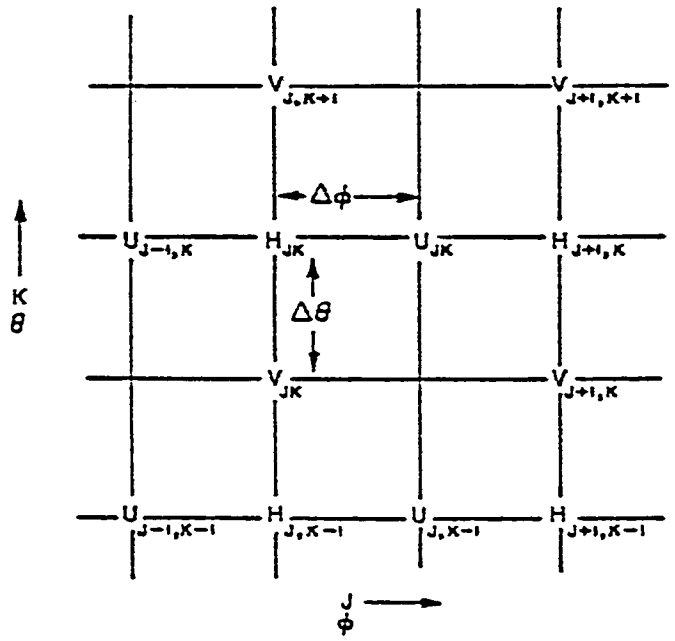

ARAKAWA C-GRID

Fig. 4: Staggered mesh used in finite difference discretization of the governing equations, showing relative location of U, V and H.

the required meshpoints prior to computing standard second order centered finite differences. This procedure helps supress the non-linear growth of numerical noise in the model (Luther et al., 1985).

Along the eastern boundary of the model, which follows the geometry of the North American coast, a non-slip boundary condition was imposed, i.e.

$$u = v = 0$$

The northern, southern and eastern boundaries are open boundaries. A variation of the Sommerfeld radiation condition implemented numerically, as described by Camerlingo and O'Brien (1980), was imposed on the open boundaries.

b) The Forcing

Three experiments were run: first, the model was forced by monthly averaged wind stress data from the Comprehensive Ocean-Atmosphere Data Set (COADS). A second experiment was done in which the wind stress was set to zero and the model was forced only through the southern boundary by imposing the results of a similar wind-forced equatorial model. In a third experiment both forcings were imposed simultaneously. In the three cases, the same parameters (time step, viscosity coefficient, etc.) and time of integration were used so that the results were directly comparable. All experiments were initiated from a state of rest and with an initial upper layer of 200 meters.

For the wind forced model and the combined wind plus boundary forced model, an initial four year spin-up period was run using the

long time monthly wind average. This time is enough for the coastal region to reach its average upper layer thickness and current values and also to set up the main east-west pressure gradient and Sverdrup balanced meridional currents over most of the domain.

After the initial spin-up period, the three models were integrated in time with a time step of 20 minutes from January 1, 1961 to December 30, 1979.

A brief description of the forcings follows:

1) The Wind:

Nineteen years of wind stress data from the COADS were used. This data for wind stress consists of ship of opportunity observations averaged in time and space every month and every 2 x 2 longitude-latitude degree squares. The values are given in units of pseudo-wind stress i.e.

$$\frac{\bar{\tau}}{\rho_o C_D} = \frac{\text{wind stress}}{\rho_o C_D} = \bar{\bar{v}}|\bar{v}|$$

where ρ_o and C_D are the density of the air and drag coefficient respectively. A value of 1.5×10^{-3} was used for C_D. Fortunately, the area of interest has been well covered by commerical ship lines, and the data presents few holes. These were filled by linearaly interpolating from its eight neighbors. After filling up the gaps for each month, the data was smoothed using a 1-2-1 Hanning filter in both directions to suppress the small scale noise in the COADS data due to

the method of data averaging into individual boxes. Fig. 5a and 5b show an example of the raw and smooth wind data respectively. Finally an IMSL 2-Dimensional spline was used to interpolate to the resolution (1/12 degrees) of the model. In time the wind was linearly interpolated to a 20 minute resolution.

The large scale winds over the California Current region are driven primarily by 2 synoptic scale, semi-permanent atmospheric pressure systems: the north Pacific high and the continental thermal low over California (Reid, et al., 1958).

During the summer northwesterly winds strengthen due to a stronger pressure gradient brought by a deepening of the continental low (Hickey, 1979). The winds are mostly parallel to the coast and northwesterly at all latitudes. This is a strongly favorable upwelling condition. Figure 6a shows the 19 year averaged July winds used in this study. In the winter season the low weakens, the north Pacific high moves closer to the coast, and the presssure gradient is reduced weakening the northwesterly wind south of about 40°N and reversing the direction north of that latitude. During this season, the winds are typically south-westerlies off Oregon and Washington (Hickey, 1979). This is a favorable downwelling situation. Figure 6b shows the 19 year averaged January winds.

A time-latitude plot of the northward component of the wind, compiled from 122 years of ship of opportunity data is shown in Figure 7 (as presented by Hickey, 1979). It is this annual strengthening and

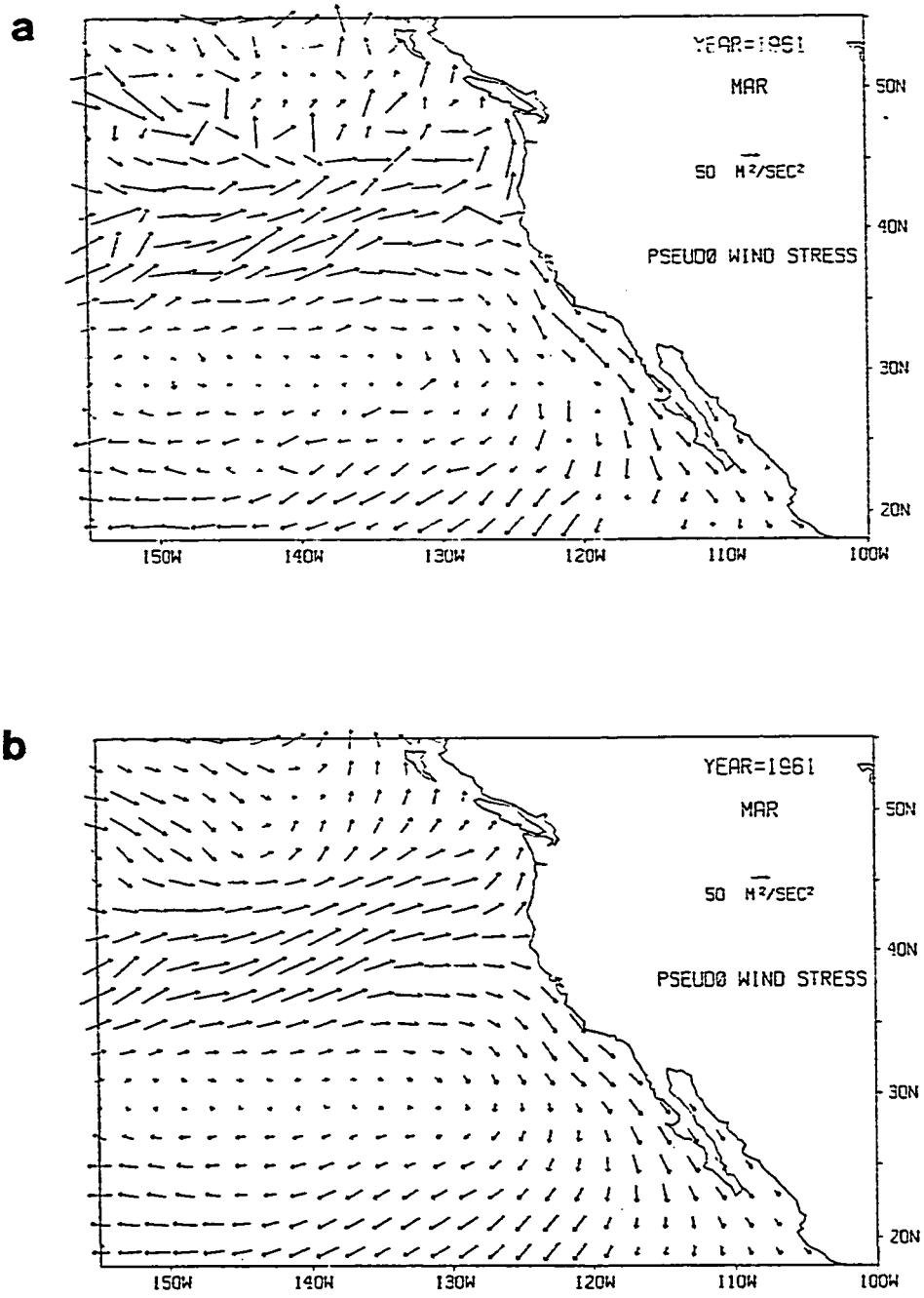

Fig. 5: Example of a) raw and b) smoothed pseudo wind stress data used to force the local model. The winds were linearly interpolated to a 1/12 by 1/12 degree mesh. Units are m^2/s^2.

a

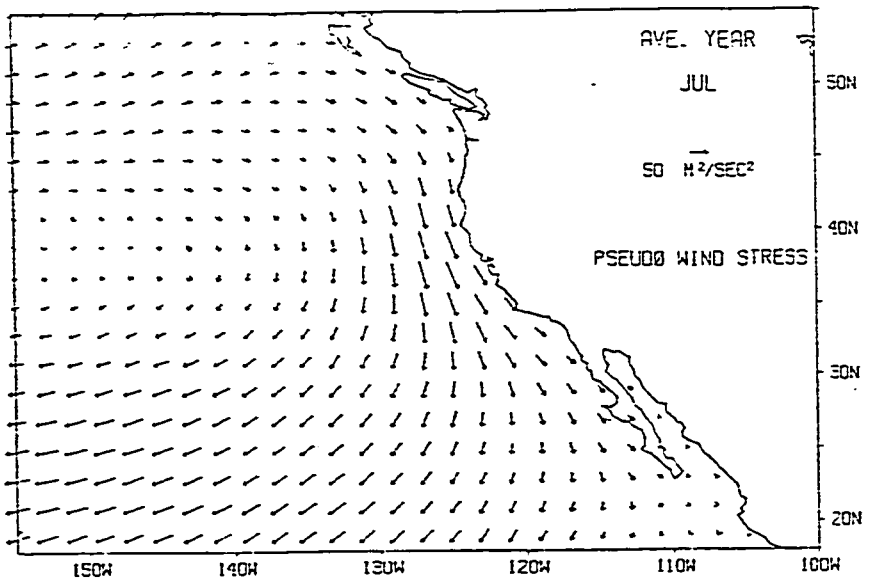

b

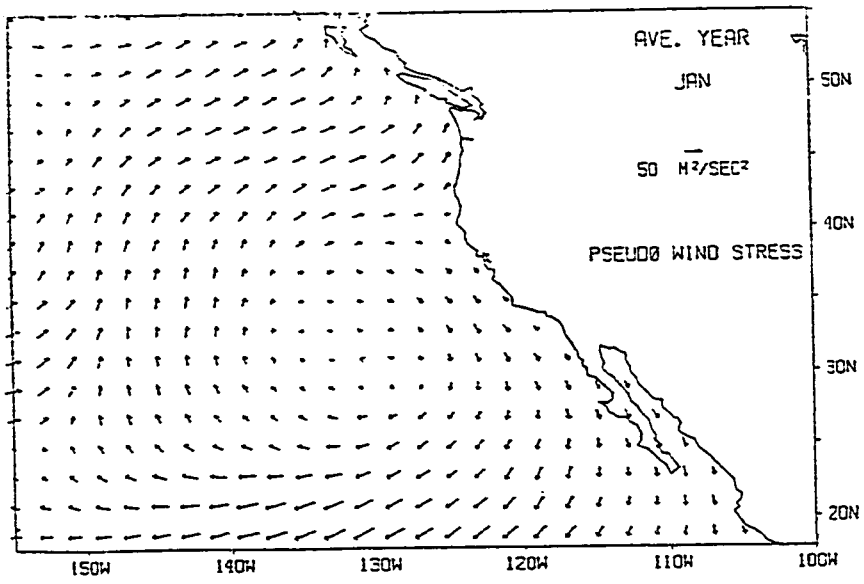

Fig. 6: Long term averaged pseudo wind stress for a) July and b) January.

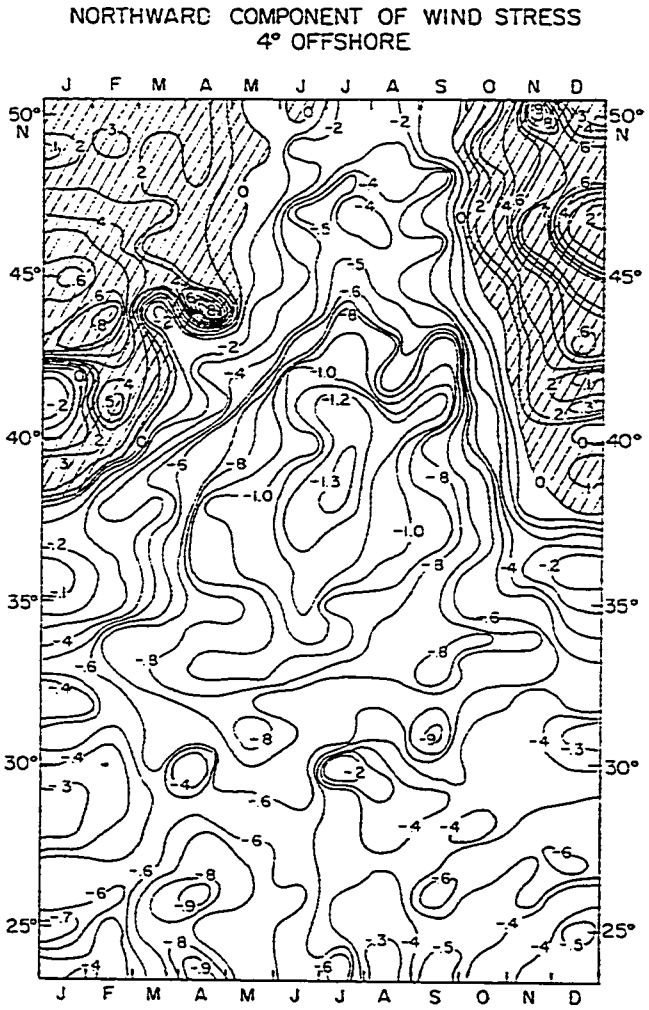

Fig. 7: The seasonal cycle of the northward component of the wind at a location four degrees off the west coast of North America from 50°N to 24°N. Units are dynamic centimeters. The contours interval is 0.1 dyn cm^{-2}. Regions of positive (northward) wind are shaded (from Hickey, 1979).

weakening, and actual reversal of the winds near the coast, that produces most of the variability in our locally forced model. A dominant feature of the winds along the coast is that the maximum magnitude and variance occurs near Cape Mendocino (40°N) (Halliwell and Allen, 1984). The standard deviation at Cape Mendocino is four to five times larger than it is along the coast of northern Baja California, southern California, or Washington (Halliwell and Allen, 1984). The large scale features of the curl of the wind stress are characterized by being negative offshore of the California Current region. This is associated with the large scale anticyclonic atmospheric circulation over the mid-Pacific Ocean. The weakening of the equatorward winds toward the coast creates a typically positive wind curl near the coast. Nelson (1977), using 122 years of wind data, compiled an annual cycle of wind stress curl. He shows that positive wind curl occurs along the coast throughout most of the year (Nelson, 1977). This band of positive wind curl has been associated with upwelling events at the coast and with the onset and sustainment of the Davidson Current (eg. Munk, 1950; McCreary, et al., 1987) and the California undercurrent (eg. Pedlosky, 1974).

2) Equatorial Model

The relevance of poleward propagating disturbances in the sea level variability along the western coast of North America has been made evident by the works of Enfield and Allen (1980) and Chelton (1980). As argued by Mooers and Philander (1977) and Clarke (1983),

some of this energy can be accounted for by coastal Kelvin waves generated when an easterly propagating equatorial Kelvin wave reaches the coast. In order to include this mechanism, our model was forced through its southern boundary near the coast (see Fig. 8) by imposing the results of a wind forced, reduced gravity equatorial model (Kubota and O'Brien, 1984). Kubota and O'Brien's model domain includes the equatorial Pacific from 20°S to 20°N and was run from January 1961 through December 1984. Values of U, V and H were taken from this model along a band of 15 degrees of longitude at latitude 18°N every 6 days. The data was interpolated in space and time to the resolution of our model.

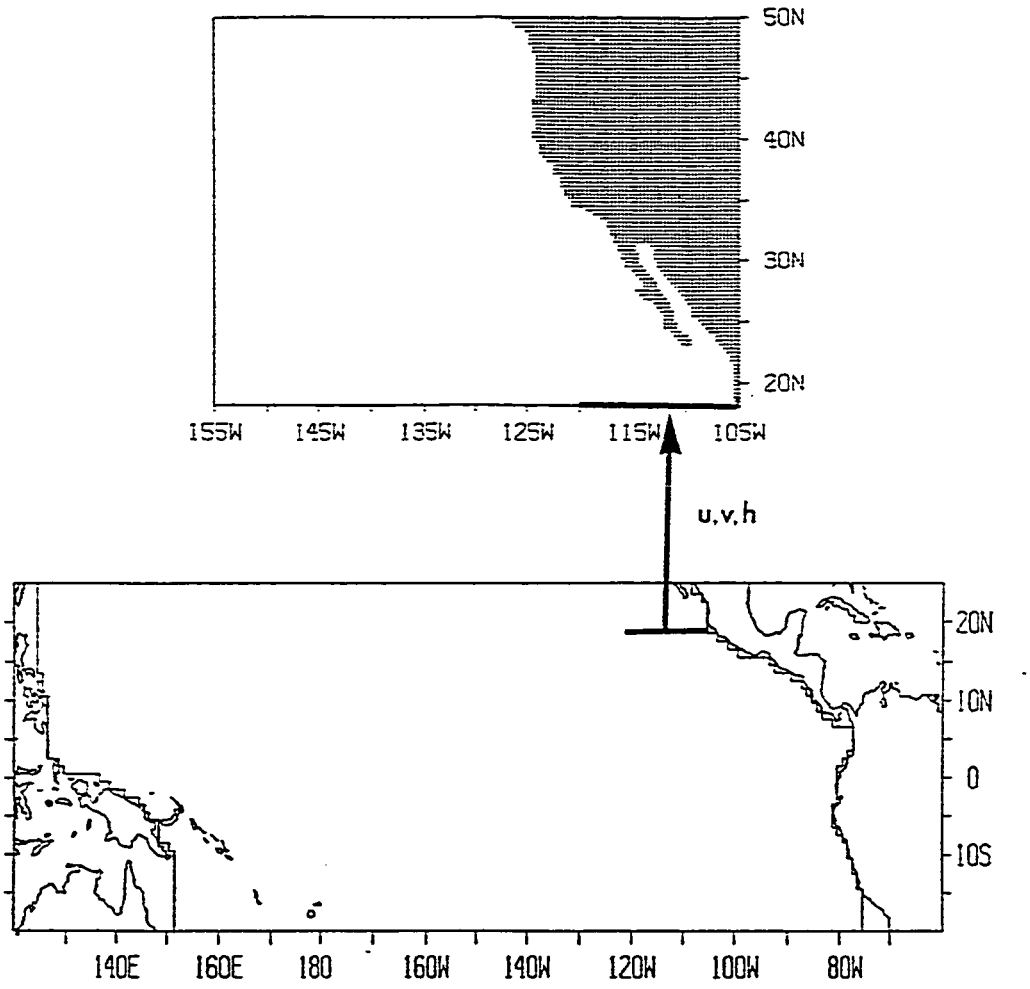

Fig. 8: Domain of the Kubota and O'Brien (1984) equatorial model used to force the remote model. U, V and H values were taken from a 15 degree transect at 18°N and imposed into our model southern boundary (heavy line).

III. SEA LEVEL VARIABILITY IN AN EASTERN BOUNDARY

In this section we present a summary of the physical mechanisms relevant to the large scale currents and sea level variability on an eastern boundary. Our goal is to provide a background for the discussion of the results in the following chapters; hence, we discuss the dynamics in terms of the reduced gravity equations (eq. 1). For simplicity we start with the linear, β-plane approximation of eq. 1, i.e.

$$U_t - fV = -C_o^2 H_x + \tau^x \qquad 2.a$$

$$V_t + fU = -C_o^2 H_g + \tau^y \qquad 2.b$$

$$H_t + U_x + V_z = 0 \qquad 2.c$$

where $f = f_o + \beta y$; $C_o^2 = g'H_o$. Away from boundaries, the main balance is between the Coriolis and pressure gradient forces, i.e. the geostrophic balance.

$$fV_g = C_o^2 H_x \qquad 3.a$$

$$fU_g = -C_o^2 H_y \qquad 3.b$$

A rotating fluid under gravity tends to this equilibrium rather than to a state of rest, and to a first approximation most of the ocean is in geostrophic balance.

Taking the curl of eq. 2.a and 2.b and using the continuity equation for the divergence of the transport, one obtains the linearized version of the potential vorticity equation; i.e.,

$$(V_y - U_x)_t + \beta V = \text{curl}\ \bar{\tau} + fH_t \qquad 4$$

This equation represents a balance between the change of local and planetary vorticity in the LHS of (4) and that imposed to the system by the wind and the vorticity change due to vortex stretching in the RHS. A balance of forced, steady motion can be achieved, i.e.

$$\beta V = \text{curl}\ \bar{\tau} \qquad 5$$

which of course is the Sverdrup balance and represents a balance between the vorticity imposed by the wind stress and the vorticity gained by the water parcel by moving meridionally to a different ambient vorticity. At midlatitude, the curl of the wind stress is mostly negative, thus producing a negative (equatorward) meridional transport (eq. 5). This mechanism drives the main large-scale gyres in the ocean and produces the main equatorward current at the eastern north Pacific. Through geostrophy, this current in turn implies an east-west pressure gradient. This characteristic is a fundamental ingredient in our model and determines the basic state in our model results. Variations around this large scale Sverdrup balance are produced by anomalous wind patterns, Ekman transports, and/or propagating disturbances.

Another possible balance in (3) is between the last two terms:

$$H_t = -\frac{1}{f}\ \text{curl}\ \bar{\tau} \qquad 6$$

Numerical experiments have shown that this mechanism (Ekman pumping)

is important at an eastern boundary. Munk (1950) suggested the positive wind curl off the California Coast as being the driving mechanism for the Davidson Current. Hurlburt and Thomson (1973) showed that a positive curl in the coastal upwelling region significantly reduces the equatorward surface current and enhances the poleward undercurrent.

Near the coast, wind driven Ekman transport is a major driver mechanism. A simple explanation of it and its associated upwelling region can be given in terms of Ekman transport [$\bar{V}_E = \frac{1}{f} \hat{k} \times \bar{\tau}$]. Due to the earth's rotation, longshore winds force surface waters away (or toward) the coast; by continuity this offshore flux requires some form of compensating vertical flow. The most important case is of course when the Ekman transport is away from the coast, since this requires an upwelling of nutrient rich water to the surface.

To illustrate the upwelling mechanism, we follow Anderson and Gill (1975) who studied the oceanic adjustment to a suddenly applied wind stress. Consider a meridional boundary and a north-south wind stress with no meridional variation. The equations are ($\frac{\partial}{\partial y} = 0$, $\tau^x = 0$ in 2):

$$\frac{\partial U}{\partial t} - fV = - C_o^2 H_x \qquad 7.a$$

$$\frac{\partial V}{\partial t} + fU = \tau^y \qquad 7.b$$

$$H_t + U_x = 0 \qquad 7.c$$

a single equation for U can be obtained, i.e.

$$U_{tt} + f^2U - C_o^2 U_{xx} = + f\tau^y \qquad 8$$

Solutions of equation 8 can be expressed as a sum of a steady part, to satisfy the boundary conditions (u=0 at x=o) and transient solutions to satisfy the initial conditions (eg. Gill and Clarke, 1974; Anderson and Gill, 1975). The steady part is:

$$U = -\frac{\tau^y}{f}\left[e^{x/R} - 1\right] \qquad 9$$

where $R=C_o/f$ is the baroclinic radius of deformation. Far from the coast this solution tends to the Ekman transport $U = \tau^y/f$. Near the coast it represents a piling up (or removing) of water. From the continuity equation, this steady flow gives

$$H = \frac{\tau^y}{Rf} e^{x/R}\, t \qquad 10$$

i.e. a linear increase (or decrease) in the ULT for a positive (negative) longshore wind stress. This increase in H is balanced by a geostrophic alongshore acceleration,

$$V = \frac{C_o^2\, \tau^y}{R^2 f} e^{x/R} t \qquad 11$$

The linear increase eventually stops due to friction and by westward radiation of energy in the form of planetary waves. Indeed, the response is not purely local. If a disturbance is generated by some mechanism at one latitude, the information is carried poleward by coastally trapped waves (eg. Gill, 1982) or westward by planetary waves (eg. Mysak, 1983). Anderson and Gill (1975) give a complete description of the transient solution of (8) needed to satisfy the initial conditions. They show that this consists basically of planetary Rossby waves that carry the coastal upwelling (or downwelling) westward. This part of the solution is more easily obtainable by going back to (2). From the unforced version of (2), equations for the horizonal transport can easily be obtained:

$$LU = -C_o^2[H_{xt} + fH_y] \qquad 12.a$$

$$LV = -C_o^2[H_{yt} - fH_x] \qquad 12.b$$

where $L \equiv \frac{\partial^2}{\partial t^2} + f^2$; for low frequency variations ($\delta t >> f^{-1}$) and assuming alongshore variations of a much larger scale than acrosshore variations (i.e. long wave approximation, $\delta y >> \delta x$), an equation for H can be obtained

$$[\frac{\partial^2 H}{\partial x^2} - \frac{f^2}{C_o^2} H]_t + \beta H_x = 0 \qquad 13$$

Wavelike solutions of this equation of the form

$$H = A \exp [i(kx - \omega t)] \qquad 14.a$$

exist where

$$\omega = \frac{-\beta k}{k^2 + f^2/C_o^2} \qquad 14.b$$

These are, of course, Rossby waves. For long waves (k small) the group velocity as well as the phase velocity are negative so that energy is propagated westward. By means of this mechanism, due to the meridional variation of the Coriolis parameter ($\beta \neq 0$), upwelling regions and, in fact, any disturbance originated at the coast are not necessarily confined to a radius of deformation as implied for example by eq. 9-11, but can propagate westward and contribute to the ocean interior variability. Observational evidence of baroclinic Rossby waves has been found in the north Pacific Ocean (eg. Price and Magaard, 1980).

A further wavelike solution is possible due to the presence of the boundary. Setting U=0 in equation 2

$$fV = -C_o^2 H_x \qquad 15.a$$

$$V_t = -C_o^2 H_y \qquad 15.b$$

$$H_t = V_y \qquad 15.c$$

Solution of these equations are of the form:

$$V = V_o e^{x/R} \exp\left(i(ky - \omega t)\right) \qquad 16$$

$$H = \frac{\omega}{k} V_o \, e^{x/R} \exp\left(i(ky - \omega t)\right) \qquad 17$$

where $R = C_o/f$ and $\omega = C_o k$.

In the northern hemisphere these waves (Kelvin waves) propagate poleward on an eastern boundary and are confined to the coast to a scale R. Kelvin waves are important for the coastal solution because they carry information away from the source region. Disturbances generated by any cause, for example by direct wind forcing, Ekman divergence, or disturbances of equatorial origin, can be radiated poleward through the coast by this mechanism. Using sea level observations along the American west coast, Enfield et al. (1980), Chelton (1980) and Christensen et al. (1983) have demonstrated the existence of poleward energy propagation with characteristics of first baroclinic Kelvin waves (i.e. eq. 16-17).

IV. RESULTS

a) Locally Wind Forced Model

1) General Overview of Model Results

Figure 9 shows a typical result from our locally forced model. The model was run for five years. Fig. 9 corresponds to a snap-shot at day June 21, 1965. The most conspicuous feature is the general decrease of ULT from west to east and its associated equatorward current. This of course is an expression of the dominating Sverdrup balance (eq. 5). Typical model currents are about 10-20 cm/s. Near the coast and to the north of 45°N, the ULT is shallower than the initial depth (200m). At the coast this is an indication of the prevailing equatoward wind stress and associated large scale coastal upwelling (eq. 10). In the northern region, this upwelling is most probably due to Ekman pumping due to a positive wind stress curl (eq. 6). Fig. 9 corresponds to a typical summer situation, i.e. strongly upwelling favorable winds. It shows that along the coast, the strongest upwelling occurs from 40°N to 50°N. A strong feature of our model is the splitting of the equatorward current at about 30N-125W into a southward and an eastward current. The eastward current, upon reaching the boundary, continues south with some turning north, closing what is the model representation of the southern California semi-permanent eddy. The position and axis of separation change somehow through the year and from year to year, but

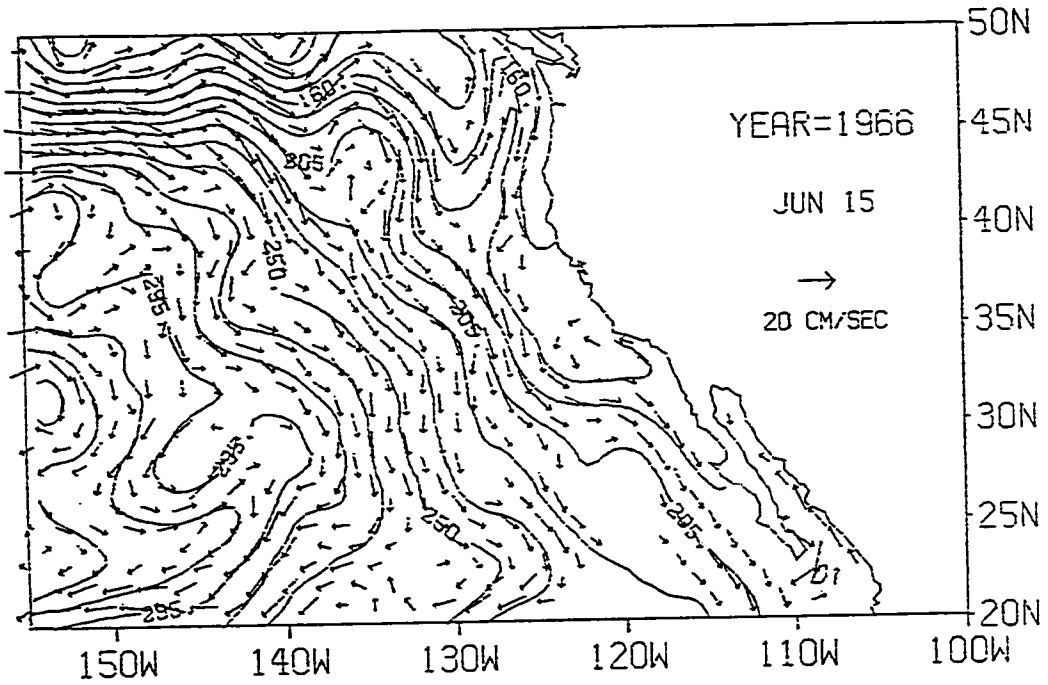

Fig. 9: Upper layer thickness (contours) and velocity (arrows). Typical output from the wind forced model. Arrows represent currents scaled according to the key in the figure. Contours are in meters. Contour interval is 15m. Currents slower than 1 cm/s are not plotted. Note area of ULT less than the initial 200m along the coast and in the northern region.

the fact that the main equatorward current changes direction around 30-35°N is very consistent result.

The global, large scale characteristics of the locally forced model are shown in figures 10 and 11: the 19 year long term mean and variance of ULT respectively. The dominant curl-of-the-wind driven mechanism is evident in figure 10. Deepest ULT occurs west of 140°W and from 20 to 35°N where the curl of the wind is most negative. ULT decreases to the east and north of this region creating an east-west pressure gradient south of about 45°N and east of 140°W. West of 140°N and north of about 25°N there is a general north-south pressure gradient. It is this pressure gradient pattern which geostrophically drives the main gyre in our model [North Pacific Gyre].

The ULT is shallower than the initial depth north of about 45°N where the curl of the wind is prevalently positive and along the coast. Maximum upwelling occurs at 40°N consistently with the latitude of maximum northwesterly winds in summer. Conspicuously, the region of maximum upwelling is not right at the coast but a few degrees from it. This is an indication of the persistence of a negative pressure gradient just at the coast which drives the coastal interior countercurrent (IC). Besides the influence of a positive wind curl near the coast, this pressure gradient could be due to the fact that the reduction of the wind stress from its maximum southwestward direction or actually reversed has a faster time scale than the relaxation of the upwelling event.

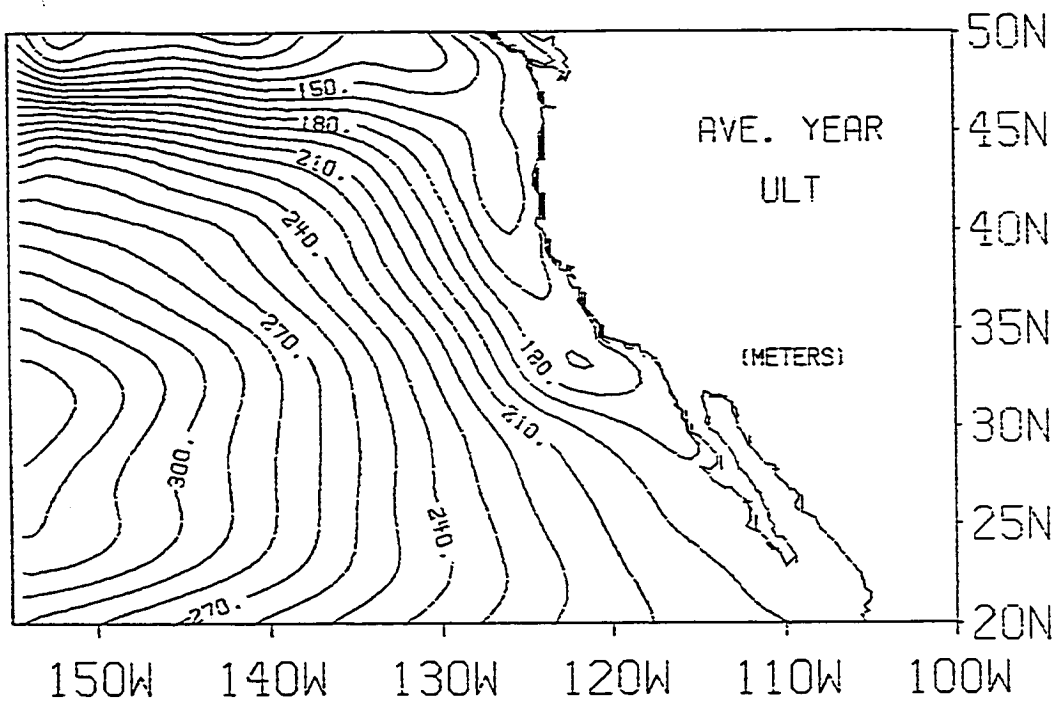

Fig. 10: Long term averaged ULT (meters) from the local wind driven model. Contour interval is 10m.

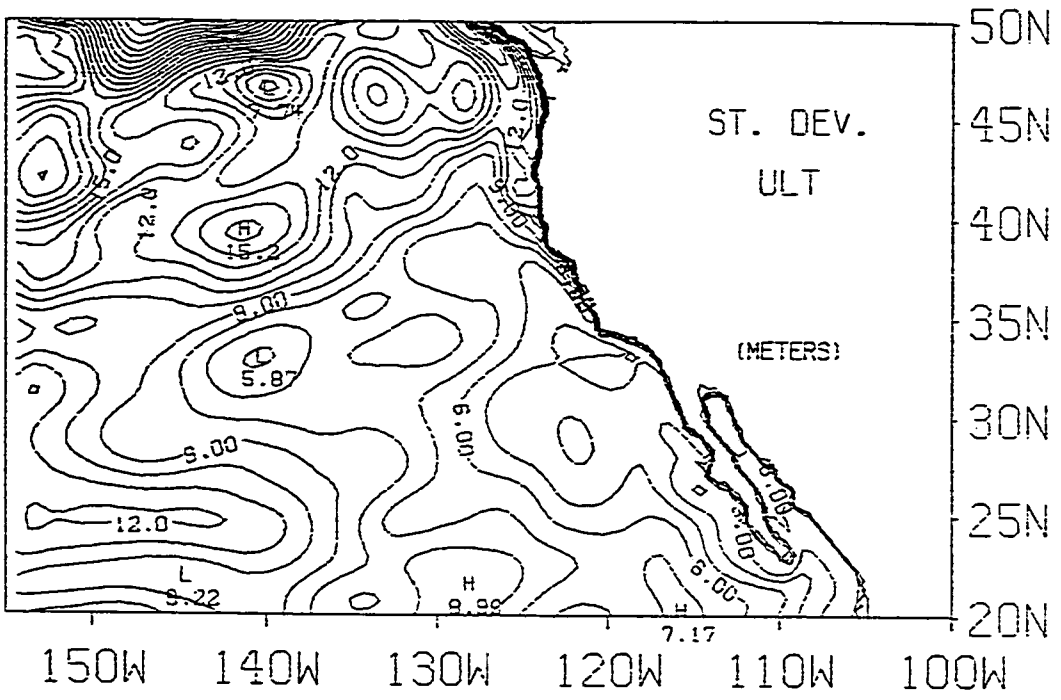

Fig. 11: Long term ULT standard deviations (meters). Units are meters. Contour interval is 1m.

Variations about the steady forced Sverdrup balance are small away from the coast except in the northern region, as shown in Figure 11. Maximum variability occurs north of 45°N which corresponds to the region of maximum variability in the winds but also is probably related to the path of waves generated at the coast at regions of strong wind reversals (eg. Mysak, 1983). Along the coast, maximum variability occurs north of 40°N. An important characteristic of Figure 11 is the monotonic increase in the variability to the north along the coast. This feature again is in part due to the fact that the winds are more variable (on a yearly scale) in the north, but also hints at the need for inclusion of the equatorially generated variability. As shown in eq. 17, disturbances generated at one region can propagate poleward so that at a given latitude, the variability is due to the locally forced variability plus the remotely forced one coming from equatorward. The further north, the more contribution from a remote forced variability a given station can have.

2) Seasonal Variability

As a typical year, we use 1966 results to describe the seasonal variability in our model. Four months, representative of the four seasons are shown in Figure 12. Figure 12a shows the ULT and velocity for March 1966. In this season, the winds at the coast are getting stronger, the regions of upwelling are developing all along the coast with a maximum at about 45°N. The eastward sweep of the southwesterly currents is evident at 30°N-121°W, but most of the easterly current

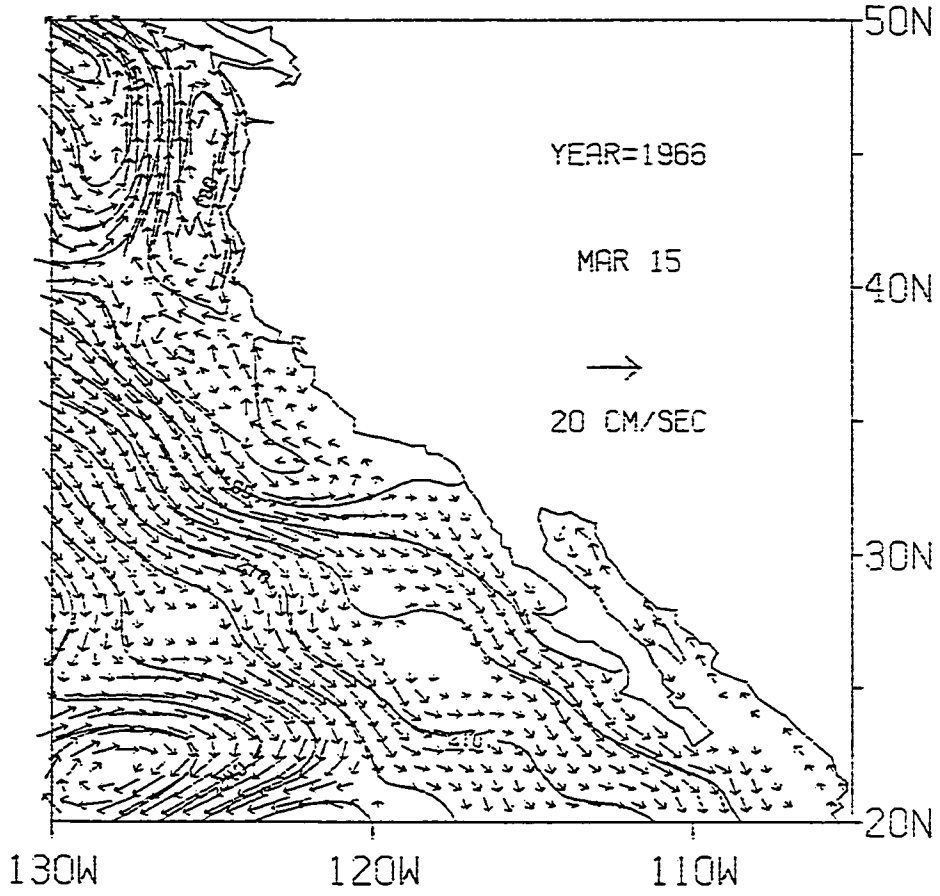

Fig. 12a: Upper layer thickness (contours) and velocity (arrows) from local model for March 1966 (typical March situation). Only the western 25 degrees are plotted. Note the eastward sweep of the southeasterly currents at around 120°W-32°N. Contour in meters with contour interval of 10m. Arrows scaled as key in figure.

turns south along the coast without forming a gyre. The current along the coast is equatorward. There is a large gyre circulation near the coast from 40°N to 50°N due to the presence of an elongated region of relatively higher ULT. This is due to a downwelling event from the previous year. By June (Fig. 12b), northwesterly winds are strong around 45°N, and strong upwelling and equatorial currents have developed in the north. Near the southern California bight, the upwelling is already relaxing, and some countercurrent is beginning to develop. The splitting point for the equatorward current has moved some degrees to the west. By September (Fig. 12c), the strong upwelling has ceased and the ULT minimum advected away from the coast. There is a well developed negative pressure gradient near the coast and the interior countercurrent (Davidson Current) is also well developed from southern Baja California to the northern part of the domain with strong poleward current around 41°N where the negative pressure gradient is strongest. The December results show (Fig. 12d) that the poleward countercurrent persists only north of 30°N where the southern sections of the California eddy marks the southern reach and the eastern turning of the equatorward current. The initial split of the equatorward current is now further west at about 128-129°W, and a new splitting region is developing where the southern section of the California Eddy is forming. A strong low ULT area persists at around 40°N, but this has propagated westward some degrees. An interesting big eddy has formed at the tip of Baja California and is detaching

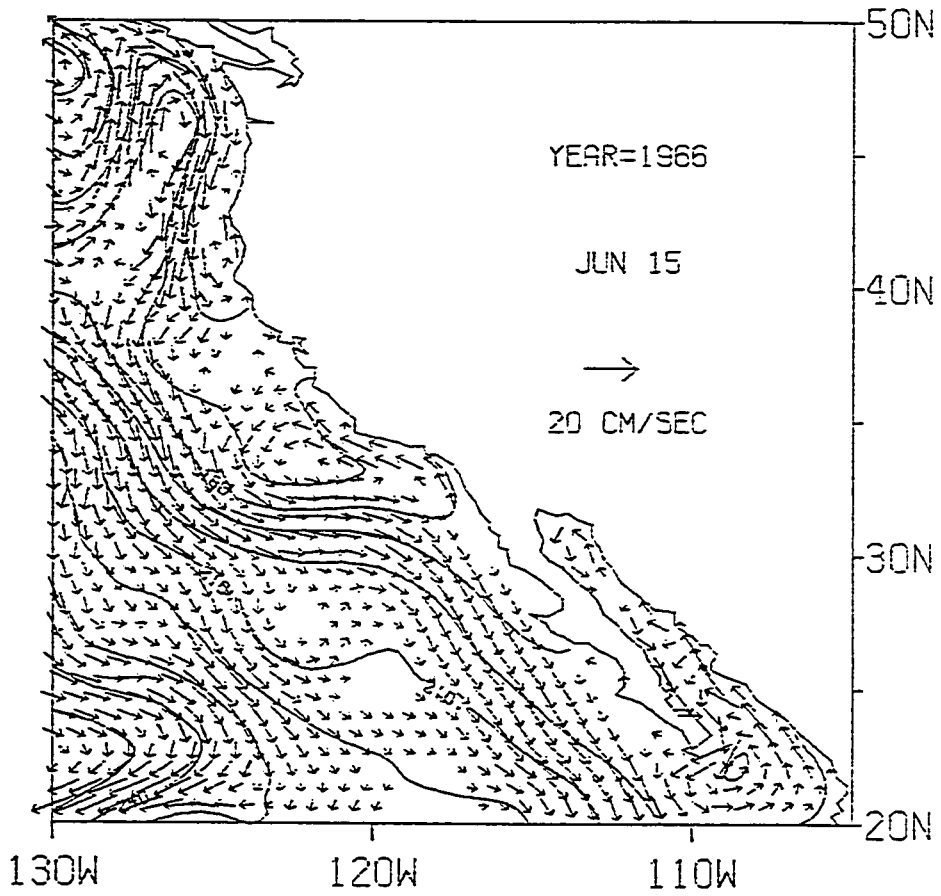

Fig. 12b: Same as 12a but for June 1966. Maximum equatorward current has moved westward compared to 12a.

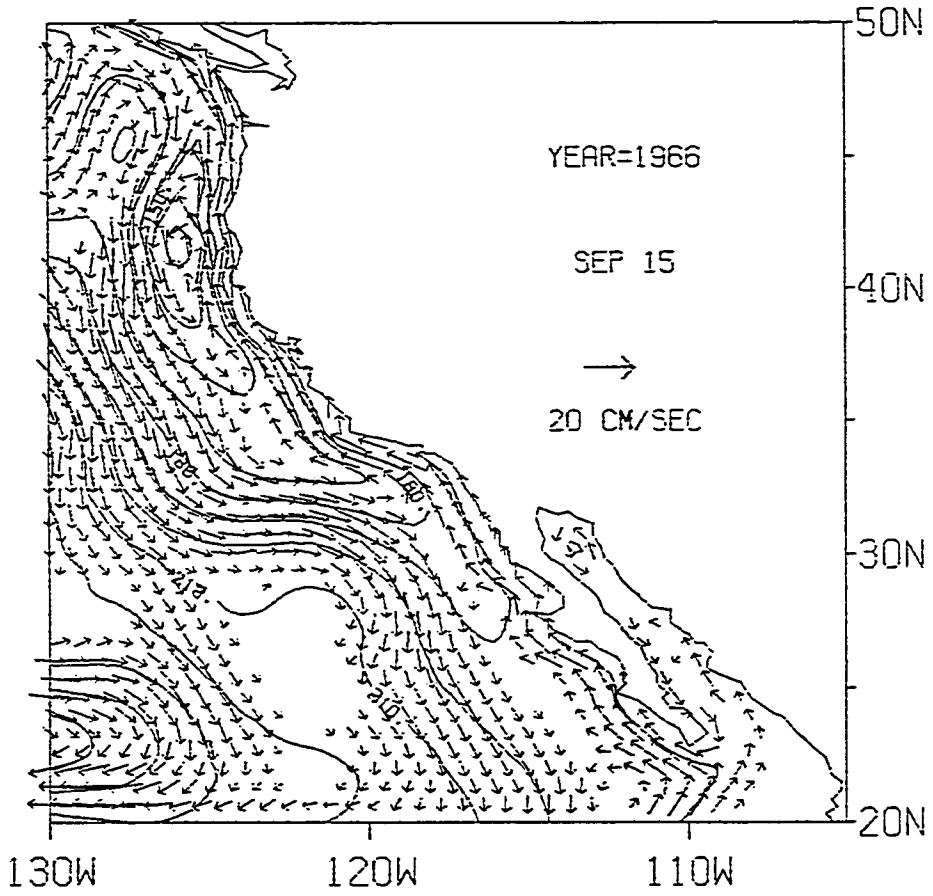

Fig. 12c: Same as 12b but for September 1966. Countercurrent is well developed all along the coast. Note the splitting of the southerly current has propagated westward.

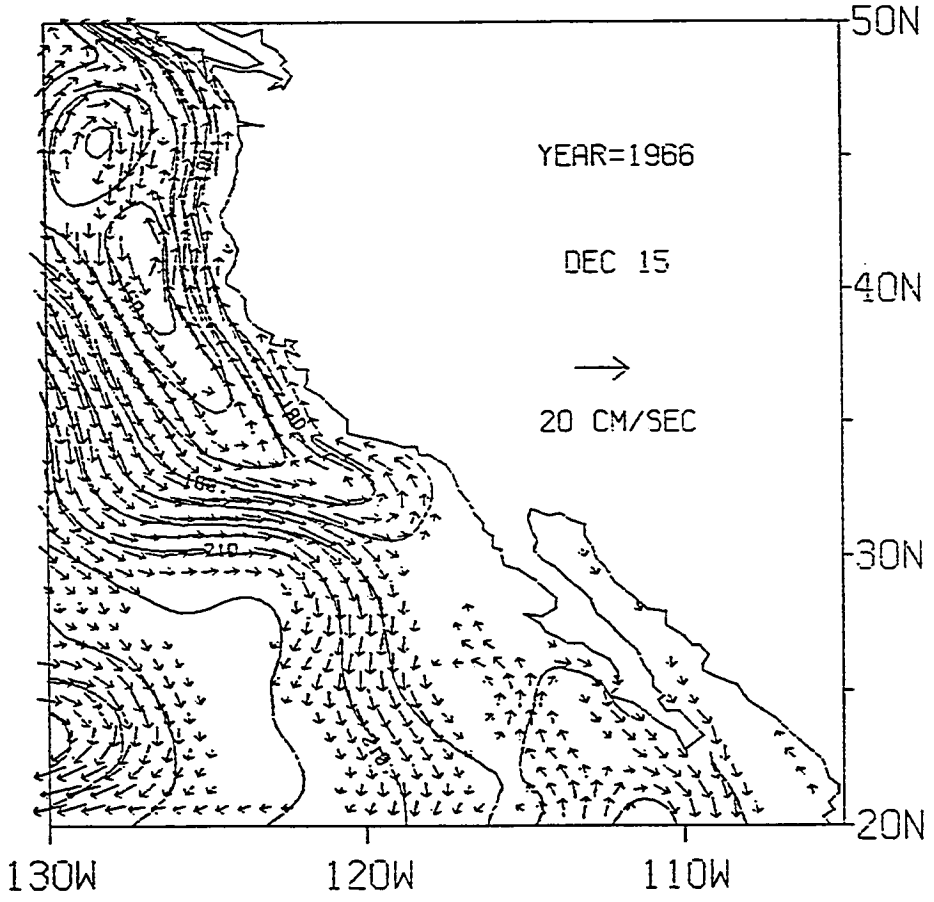

Fig. 12d: Like 12a but for December 1966. The bifurcation that was near the coast in March has propagated to about 130°W, and a new splitting has developed. The countercurrent has retreated to north of the California bight. Note that a big eddy has developed and is detaching from the tip of Baja California.

from it and propagating westward.

There are two areas of preferential eddy formation, at the mouth of the Gulf (20°N) and at the region of strong wind reversal (40°N). A third area of generation of westward propagating disturbances seem to be the regions south of the southern California Eddy (i.e. south of the California bight). By differential relaxing of the upwelling events north and south of around 30°N, a splitting of the equatorward current is formed, with the eastward branch closing the southern California eddy and the rest continuing southward. The splitting itself seems to propagate westward with the characteristics of a westward propagating annual Rossby wave. To analyze this point further, long term averaged monthly anomalies of ULT with respect to the long term annual mean are plotted in Figure 13.

Positive anomalies along the coast occur from October to March while negative anomalies occur from April through August or September. The larger negative anomaly is in June; ULT starts increasing ($h_t>0$) until it reaches the maximum in January. From January to June, the ULT decreases ($H_t<0$). It is clear from Fig. 13 that this relaxation is not in the way of a standing wave at the coast but by westward relaxations of the disturbance. Although this process happens all along the coast, as mentioned before, two regions seem dominant. Fig. 13 clearly shows most of the annual energy emanating from 40°-45°N and from around 20°N. The 20°N waves is due to the effect of the Gulf. These two source regions coincide with what has

Fig. 13: Long term monthly ULT anomaly from local model. The long term average was subtracted from the long term monthly means. Contour interval is 2m. Strongest anomalies generated near 40°N and from the mouth of the Gulf of California. Note the westward propagation of anomalies through the year.

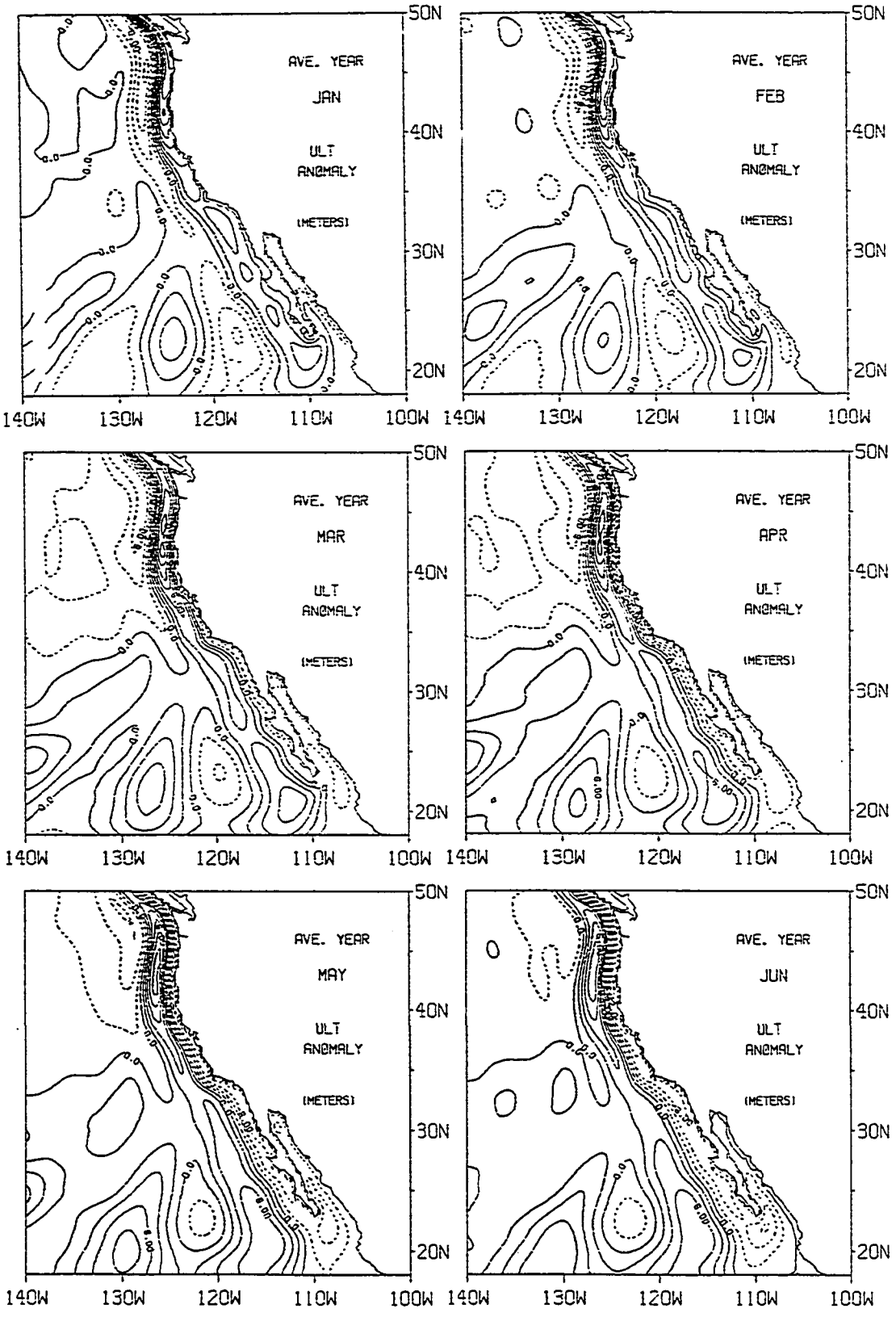
AVE. YEAR
JAN
ULT
ANOMALY
(METERS)
AVE. YEAR
FEB
ULT
ANOMALY
(METERS)
AVE. YEAR
MAR
ULT
ANOMALY
(METERS)
AVE. YEAR
APR
ULT
ANOMALY
(METERS)
AVE. YEAR
MAY
ULT
ANOMALY
(METERS)
AVE. YEAR
JUN
ULT
ANOMALY
(METERS)
50N
40N
30N
20N
140W
130W
120W
110W
100W

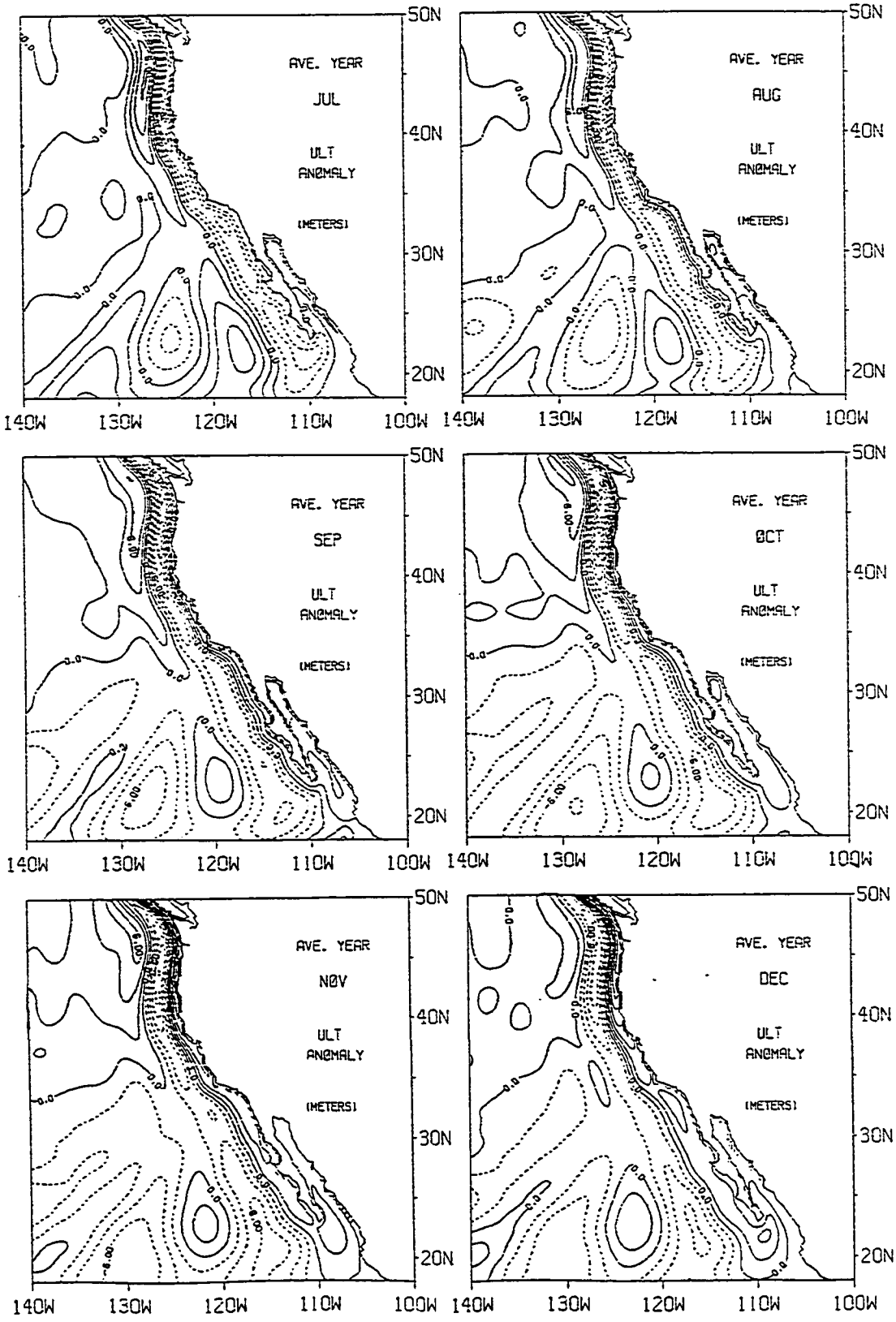
AVE. YEAR
JUL
ULT
ANOMALY
(METERS)
AVE. YEAR
AUG
ULT
ANOMALY
(METERS)
AVE. YEAR
SEP
ULT
ANOMALY
(METERS)
AVE. YEAR
OCT
ULT
ANOMALY
(METERS)
AVE. YEAR
NOV
ULT
ANOMALY
(METERS)
AVE. YEAR
DEC
ULT
ANOMALY
(METERS)
50N
40N
30N
20N
140W
130W
120W
110W
100W

been identified by other authors (eg. Cummins et al., 1986; White and Saur, 1981). An interesting feature is the absence of waves of significant amplitude emanating from the latitude band 30-35°N. This later characteristic has been noted before in Cummins et al. (1986) analysis.

3) Large Scale Variability of ULT and Wind Stress Along the Coast

Time series of ULT and wind stress were constructed for the 15 stations shown in Table 1. The wind series are of the alongshore component parallel to the general direction of the coast at each station (Table 1). Fig. 14a and 14b show the monthly averaged time-latitude plots for winds and ULT respectively. The dominance of an annual cycle is evident. There are strong equatorward winds during summer and weak equatorward or (in the north) even poleward winds in winter. The strongest equatorward winds occur between 35°N and 40°N and the strongest poleward at 48°N. The long term mean wind magnitude versus latitude (Fig. 15) shows a net annual poleward wind ($\approx 2\ m^2/s^2$) only for the two northern most stations. The variability represented by the average deviation from the mean [i.e. $\frac{1}{N} \sum |x_i - \bar{x}|$] in Fig. 16, increases from 16 m^2/s^2 at 48°N to a maximum of 22 m^2/s^2 at 40°N and a sharp drop to about 6 m^2/s^2 at 35°N. The variability stays more or less constant from 35°N (the California bight) to the south.

Direct wind driven Ekman drift and associated upwelling is manifest in the ULT time series (Fig. 14b). The ULT is at all times

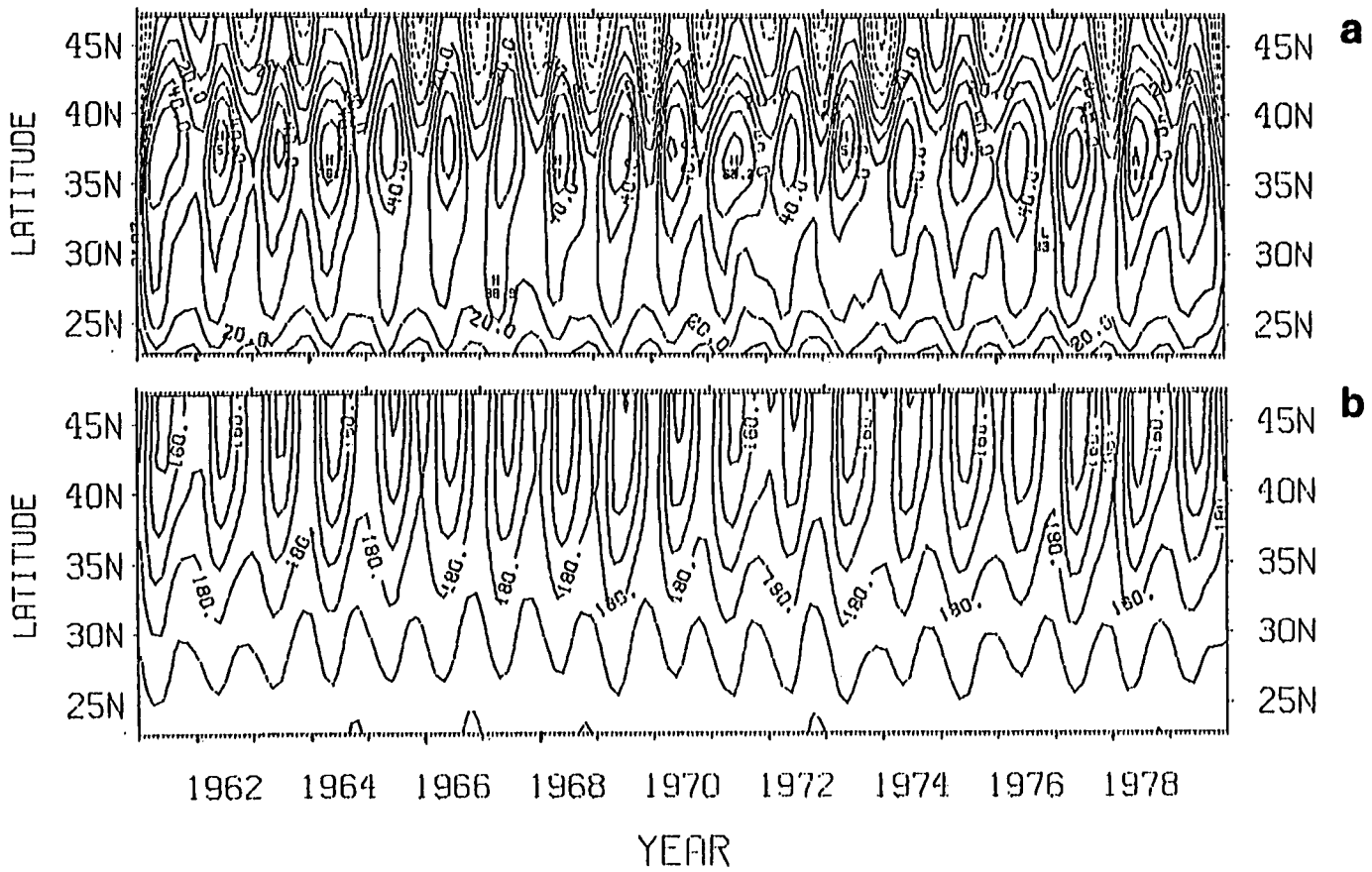

Fig. 14: Time-latitude (alongshore) plots of a) the projection of the pseudo wind stress vector to the general direction of the coast. Units are m^2/s^2; contour intervals are 10 m^2/s^2. Continuous line (positive contours) represent equatorward winds and b) ULT from the local model units in meters. Contour intervals in 10m. These plots were constructed from the time series at the stations indicated in Table 1 and marked in Fig. 3.

TABLE # 1

STATION NUMBER	STATION NAME	KEY	LATITUDE	DIST. FROM CSL (KM)	DIRECTION OF COAST, CLOCKWISE FROM EAST
1	CAPE SAN LUCAS	CSL	23.0°N	0	0°
2	SAN CARLOS	SC	24.1°N	249	36°
3	*	*	26.1°N	537	43°
4	SEVASTIAN VISCAINO BAY	SVB	27.6°N	797	90°
5	*	*	29.3°N	995	34°
6	ENSENADA	EN	31.5°N	1224	62°
7	SAN DIEGO	SD	32.7°N	1397	62°
8	LONG BEACH	LB	33.6°N	1566	24°
9	AVILA BEACH	AB	35.2°N	1878	56°
10	SAN FRANCISCO	SF	37.8°N	2234	40°
11	*	*	39.3°N	2468	70°
12	CRESCENT CITY	CS	41.8°N	2727	73°
13	SOUTH BEACH	SB	44.1°N	3003	90°
14	ASTORIA	AS	46.1°N	3208	90°
15	NEAH BAY	NB	48.4°N	3481	69°

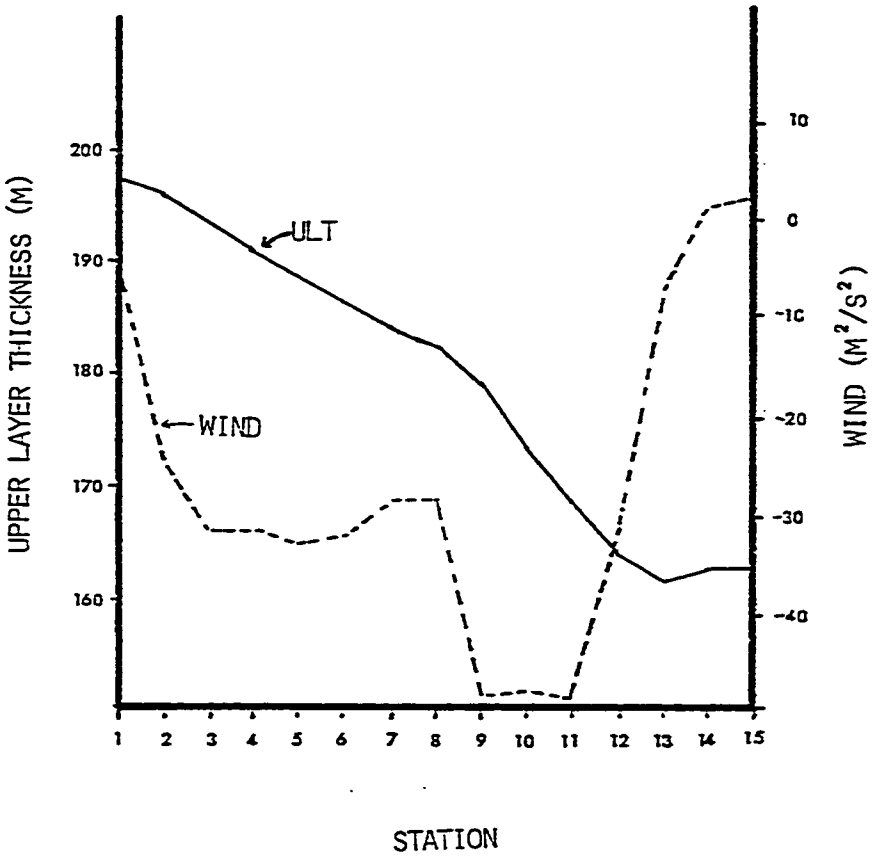

Fig. 15: Long term mean ULT (continuous line) and alongshore wind magnitude (dotted line) on the alongshore transect from station 1 to 15. Numbers identify the stations along the coast according to Table 1. Units are: meters for ULT and m^2/s^2 for wind.

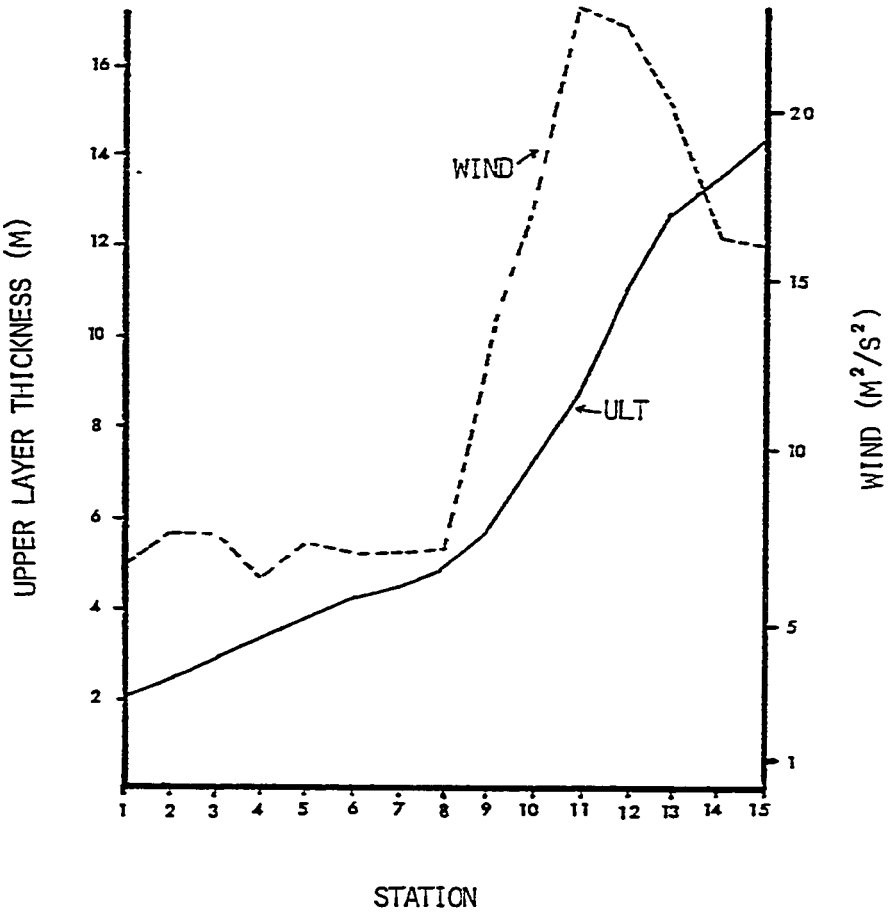

Fig. 16: Same as 15 but for the averaged deviation [i.e. $\frac{1}{N} \sum_{i=1}^{N} |X_i - \bar{X}|$].

and latitudes less than the initial depth of 200 m which of course is indicative of the prevalence of equatorward winds along the coast. During summer, the strong southerly winds in the north produce a maximum north-south ULT gradient with almost 50 m difference between the northern and southernmost stations. In the winter, the difference is reduced to about 15-20 m due to the relaxation and reversal of the winds. In contrast to the winds, variability of ULT (Fig. 16) increases monotonically from south to north, although there is a change in its gradient at the latitudes where the wind stress variability increases (i.e. 35°N). This fact is in accordance with Kelvin wave theory. ULT variability generated at a given latitude contributes to that latitude energy budget plus to that of all stations to the north. The form of the long term coastal ULT as function of latitude (Fig. 16) is consistent with the mean annual sea elevation determined by steric height as presented by Reid and Mantyla (1976).

There is some interannual variation in the winds and ULT series. For example, for the winter of '68-'69, '69-'70, and '77-'78 the positive wind anomalies extend further south than the average, and for '73-'74 the duration of positive wind is longer than average. The ULT and wind interannual variation are plotted in Figures 17a-17b. These long term variations were calculated using a 13 month running mean filter in the time series. Positive anomalous wind events (i.e. weaker equatorward winds or stronger than average poleward winds) are

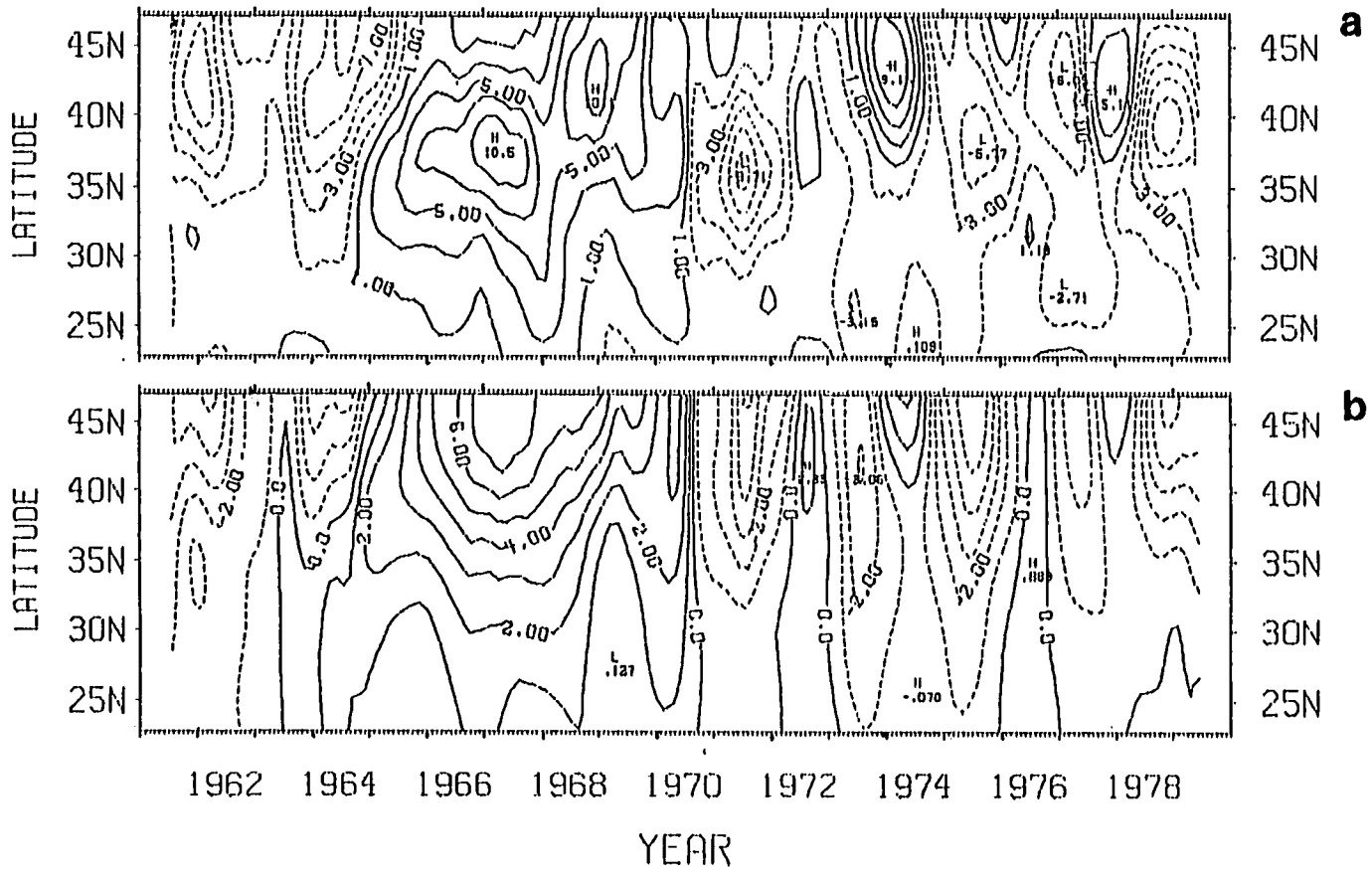

Fig. 17: Latitude-time plot interannual variability for a) wind stress and b) ULT from local model. Positive contours indicate stronger than average poleward winds and deeper than average ULT. Units are m^2/s^2 for winds and m for ULT. Countour intervals are 2 m^2/s^2 and 1 m for the wind and ULT respectively.

present mainly at 1965-1969, 1974, and 1978. All these years are characterized by positive anomalies of ULT (i.e. deeper than average). The occurrance of several continuous years of positive anomalies in the winds (1965-1969) produces a relatively strong ULT positive anomaly at the coast. On average, the ULT for the 70's is deeper than for the 60's. The positive anomalous event in this wind driven model ULT does not seem to be particularly well correlated to identified El Niño events.

To investigate the form of the ULT response to the applied winds, we calculated cross-correlation matrices from the latitude time series. From Fig. 18a it is evident that there is high correlation at all latitudes. The maximum correlation shifts to negatives values as the station separation increases, i.e. events happening first in the south than in the north. The orientation of the ridge of maximum correlation indicates a propagation of the ULT signal to the north; however, the implied speed (average approximately 3200 km in about 2 months) is too slow to represent coastal wave propagation. By comparing the ULT cross-correlation matrix with that of the wind (Fig. 18b), it is clear that the propagation implied in Fig. 18a is due to a direct local response of ULT to slowly propagating winds patterns. Indeed, both correlation matrices are qualitatively very similar, with the actual values smaller for the winds than for the ULT series due to a shorter decorrelation scale for the former. The structure of the wind correlation matrix (and that of ULT) indicates a slow

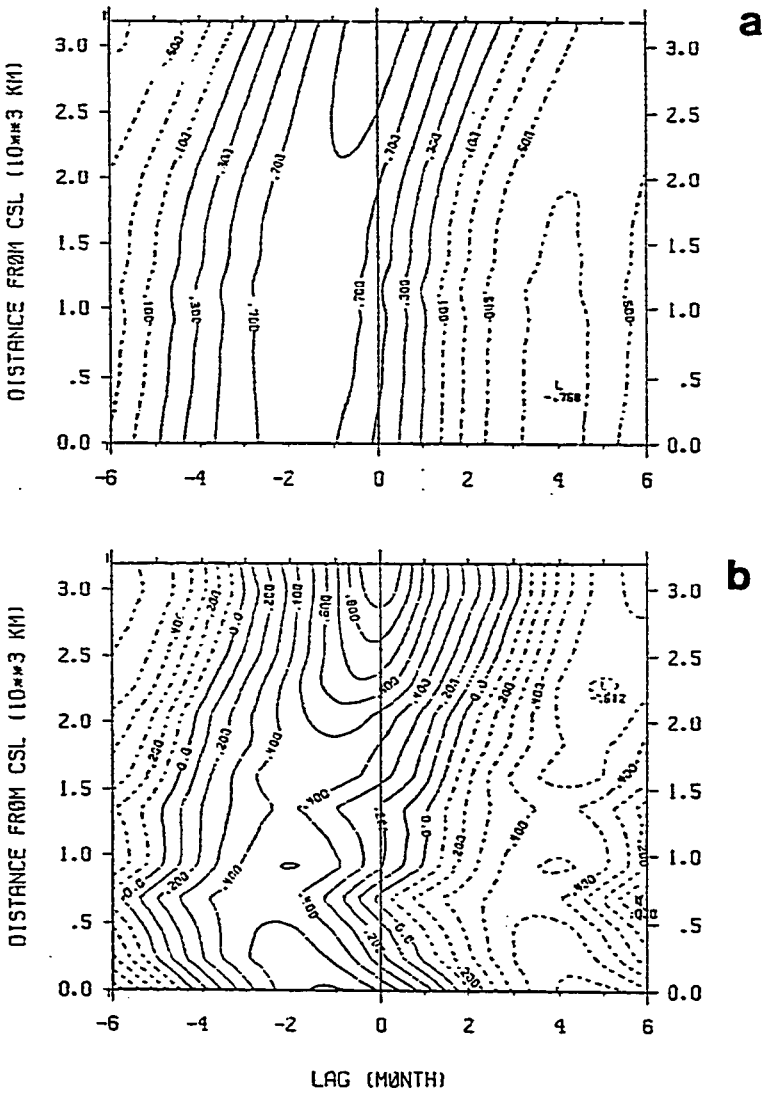

Fig. 18: Crosscorrelation matrix of a) ULT and b) winds between time series at station 15 and all other stations (Table 1). The scale at left is the distance in thousandth km. From Cape San Lucas, southern Baja California (ST 1). Positive lag means station 15 leading.

propagation of events from south to north. Figure 18a represents the overall (all year) correlation matrix. Halliwell and Allan (1987), from an analysis of wind series (higher frequencies) along the western North American coast, concluded that there is poleward propagation of wind events only during the summer months, with equatorward propagation for the winter. The fact that the overall correlation indicates poleward propagation is probably due to the dominance of the more energetic summer events. Brink (1987) acknowledges the dificulty of discriminating between observed locally forced variability and that due to remote forcing. Due to the large scales of the wind patterns, a high correlation between local wind and sea surface elevation (SSE) for example, does not necessarily mean that the SSE is locally driven; rather it could be due to a SSE forced by winds at a remote station, which in turn is coherent with the local winds (Brink, 1987).

The correlation matrix between ULT time series at station 15 versus the time series of the winds at all other stations (Fig. 19) demonstrates the fact that the ULT is best correlated with the winds earlier in time (at negative lags) and with stations further south of it. In particular the maximum at about 2,500 km from CSL shows that station 15 ULT series is best correlated with the wind at about 500 km to the south and earlier in time. In Fig. 20 we plotted the maximum correlation matrix (regardless of the lag) between the ULT time series at all the stations and the time series of the winds. For example, station 15 ULT shows a correlation of about .8 with the time series of

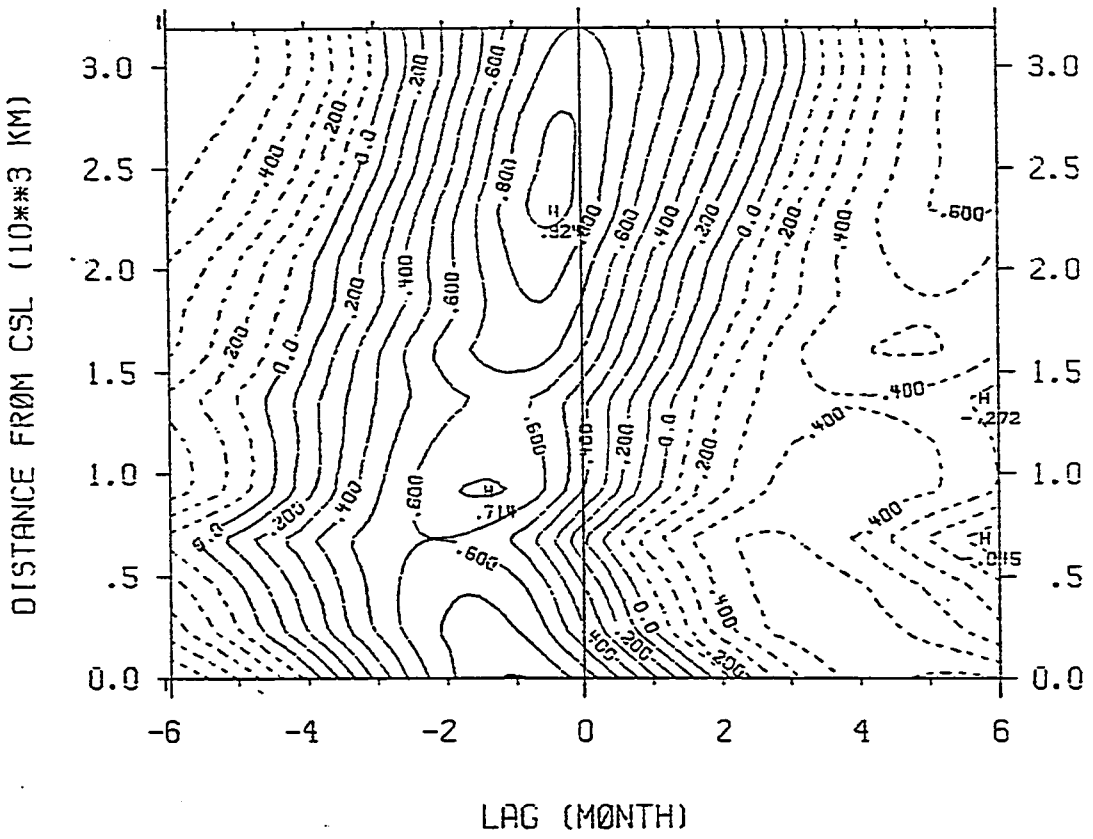

Fig. 19: Crosscorrelation matrix between time series of ULT at station 15 versus time series of wind at all other stations. Positive lag means ULT series leads the wind. Note the maximum correlation of ULT at station 15 is with the time series of the wind a few days earlier and about 500-600 km to the south.

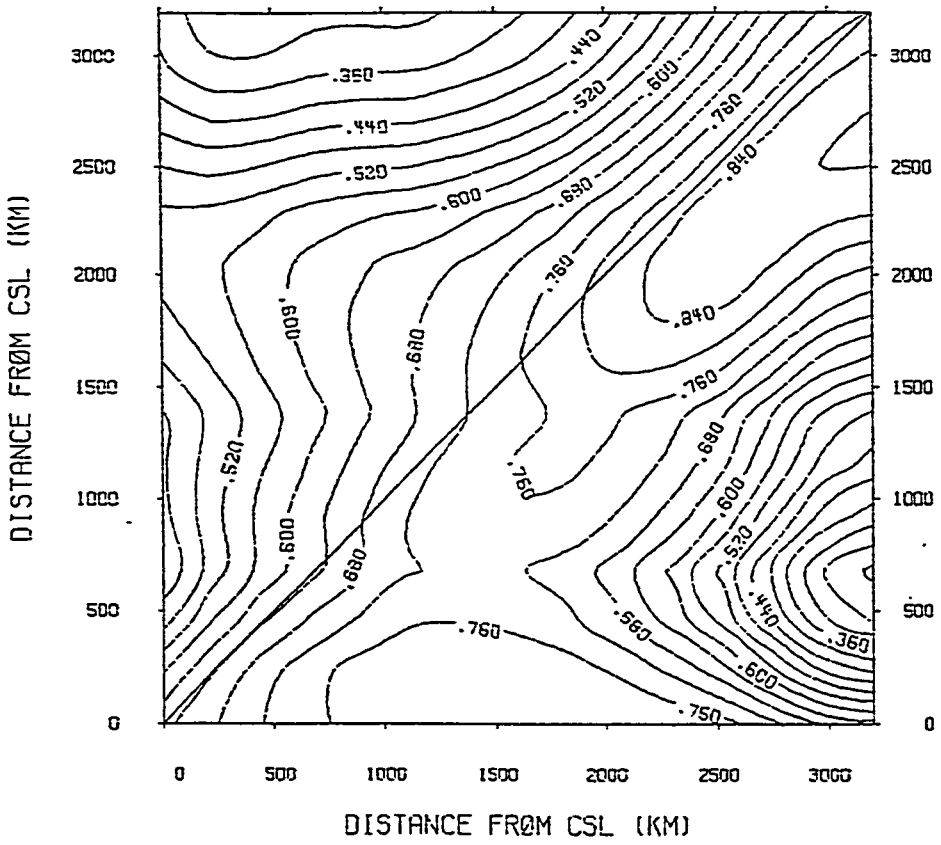

Fig. 20: Maximum correlation matrix between ULT and winds time series. Figure displays the maximum correlation, regardless of time lag, occurring between time series of ULT (abscissas) and the wind (ordinates). The 45 dcegree line marks the maximum correlation between time series of ULT and the wind at the same station. For example, station 15 (northernmost) shows a correlation of about .8 with the time series of the wind at the same station (value at the top right corner of plot), but a maximum correlation of .9 with the wind about 500 km to the south of it.

the wind at the same station (value at right top corner of plot), but it has a stronger correlation (.9) with the winds about 500 km to the south of it. A maximum along the 45 degree line would indicate a direct ULT response to local wind with no propagation. The presence of a ridge below and mostly parallel to the 45 degree line indicates that ULT correlation to the winds further south, at a fixed distance, occurs at all the stations. This characteristic is again just the result of waves spreading information only in the poleward direction, i.e. the direction of free wave propagation. Wind stress variability leading coastal sea level variability in time and space has been found by several authors (e.g. Halliwell and Allen, 1987; Allen and Denbo, 1984). Halliwell and Allen (1987) showed the sea level response at a given location along the western North American coast to be most highly correlated with the winds at lag distances 300 to 400 kilometers equatorward of that location.

b) Remotely Forced Model

As explained in chapter II, a second model was run in which the eastern most 5 degrees of the southern boundary were forced by imposing values of U, V and H taken from an equatorial model. The results, described in this section, are qualitatively different than those from the locally forced model. The most conspicuous difference between the long term mean of the remote model and the local model is the absence of an east-west ULT gradient. This of course is not surprising, since the remotely forced model lacks the mechanism for

its generation, i.e. the large scale negative wind curl. The basic mechanism driving this second model is graphically illustrated in Figure 21. This figure shows snap-shots of ULT and currents at six day intervals, from January 15 to February 3. The figure presents the results for 1962, the second year of integration. An upwelling event has entered the domain through the southern boundary and reached 27°N by January 15; six days later, at January 21, the low ULT signal has propagated north to about 35°N (Fig. 21b), 43°N by January 27 (Fig. 21c) and 50°N by February 3 (Fig. 21d). At the same time, a downwelling event that was inside the Gulf in its western side at January 15 propagates around it and north along the coast, reaching 35°N in the 24 day interval. The offshore decaying scale and speed of propagation indicate, of course, that this propagation corresponds to first baroclinic coastal Kelvin waves described by (16-17). The theoretical offshore scale, given by the baroclinic Rossby of deformation ($\sqrt{g'H}/f$) is approximately 30 km and 10 km for latitudes 24° and 40°N respectively, and the speed of propagation ($\sqrt{g'H}$) is about 2.5 m/s. Also shown in Figure 21 are the upwelling-downwelling associated geostrophic currents. An upwelling event (negative pressure gradient at the coast) drives an equatorward current, while poleward currents are associated with downwelling events.

The succession of annual upwelling and downwelling events, appearing at the southern boundary and propagating along the coast, constitute most of the response of the remotely forced model as proven

Fig. 21: Upper layer thickness minus 200m (contours) and velocity (arrows) from the remote forced model. Figure shows four snap-shots of the results six days apart a) January 15, b) January 21, c) January 27 and d) February 3. Arrows are scaled according to the key in the figure. ULT deeper than 10m is shaded darker and ULT shallower than -10m is shaded lighter.

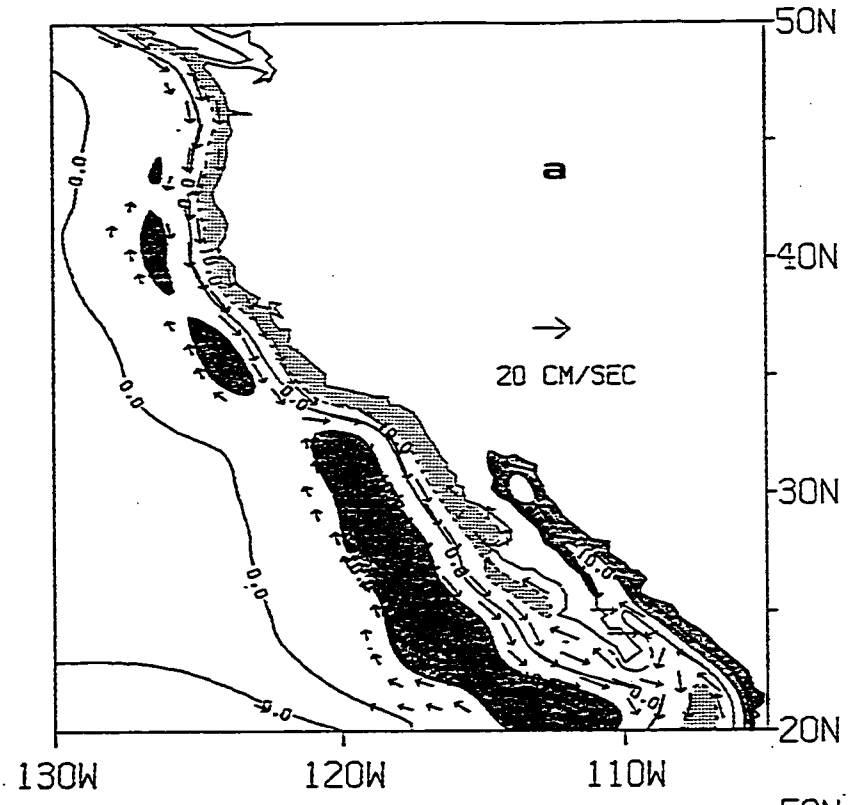
a
20 CM/SEC
50N
40N
30N
20N
130W
120W
110W
0.0

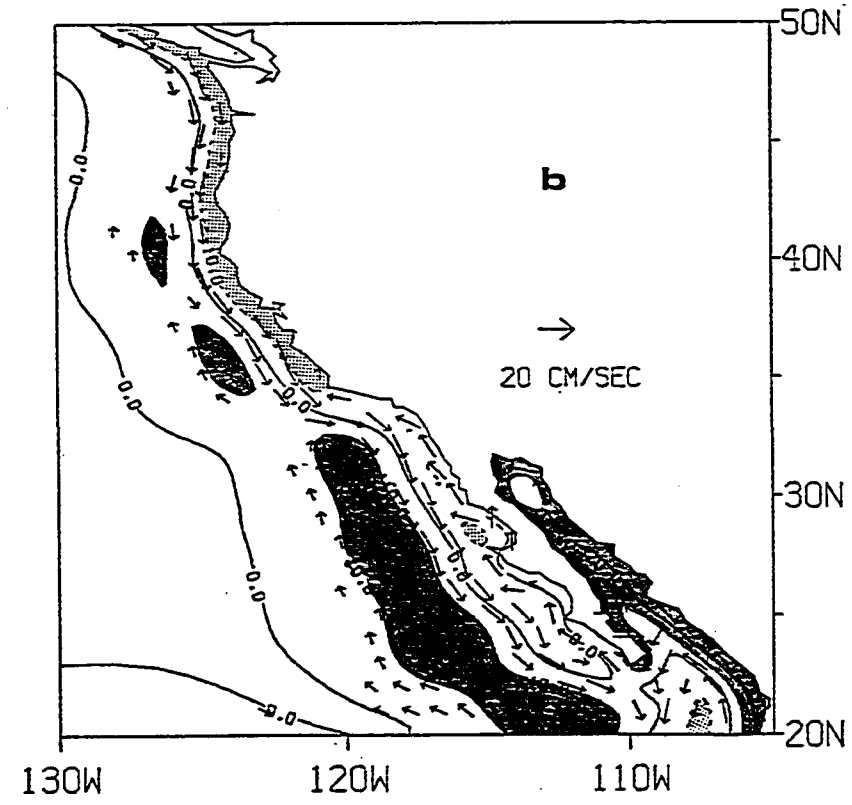
b
20 CM/SEC
50N
40N
30N
20N
130W
120W
110W
0.0

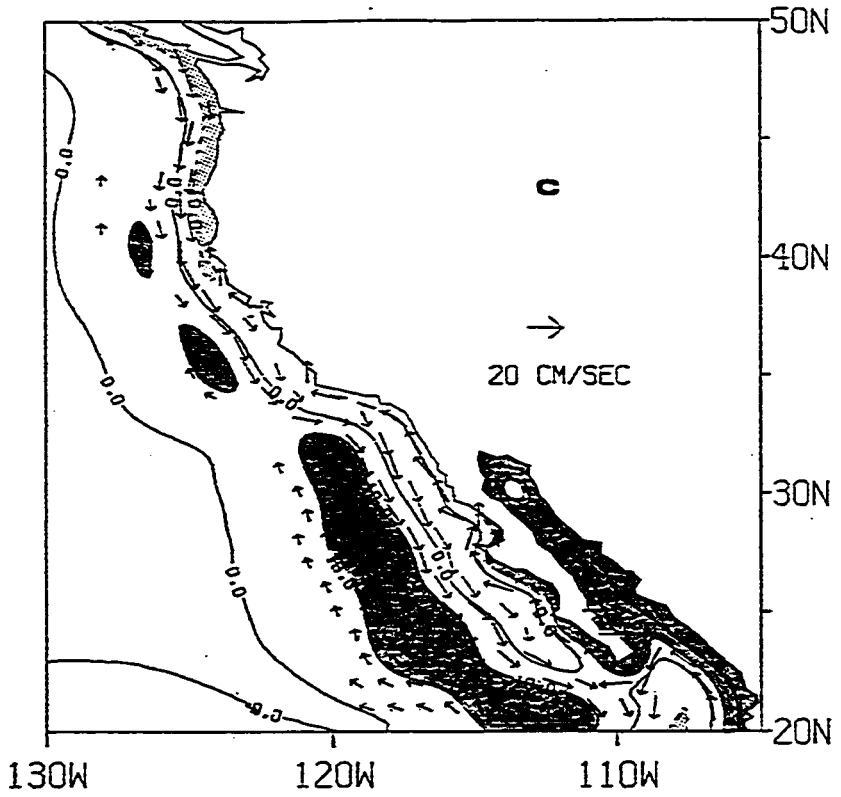
c
20 CM/SEC
50N
40N
30N
20N
130W
120W
110W

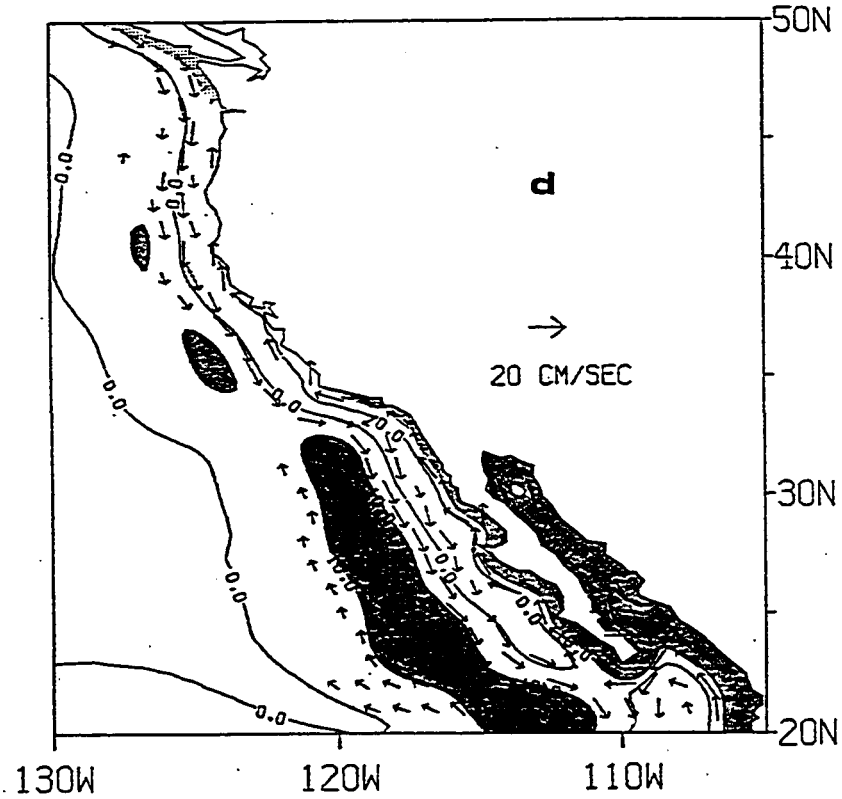
d
20 CM/SEC
50N
40N
30N
20N
130W
120W
110W

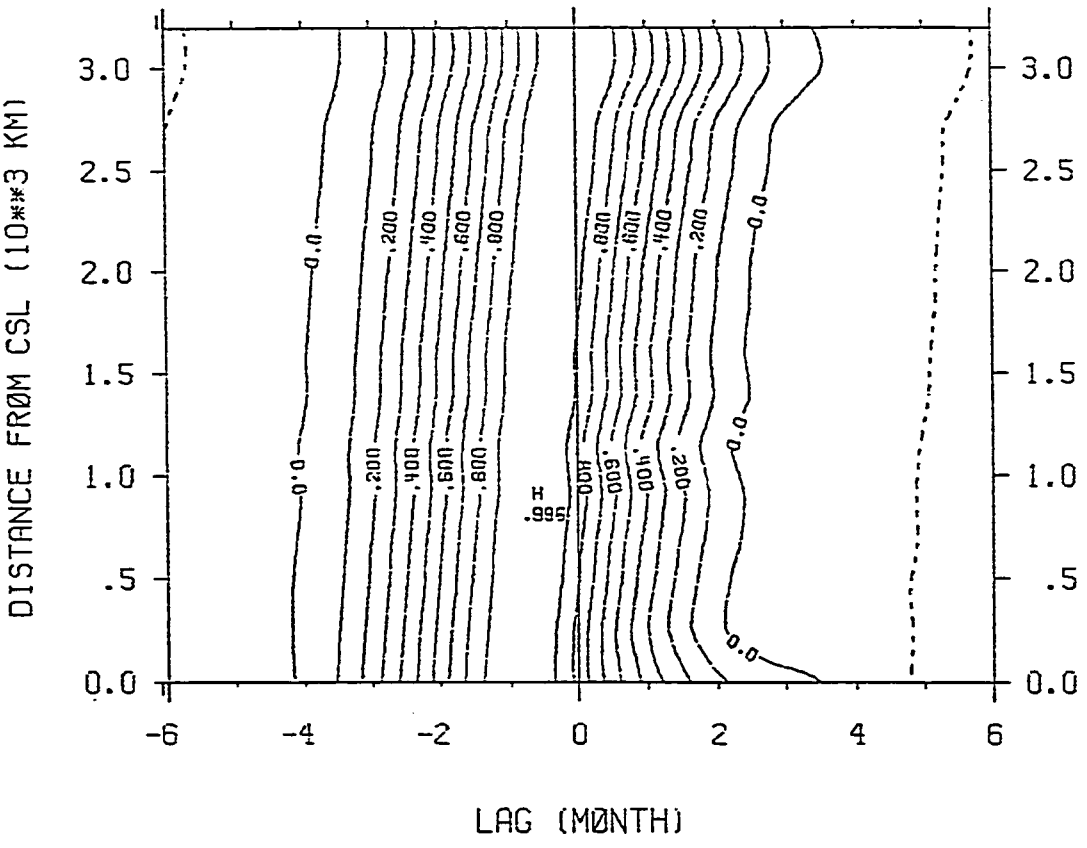

Fig. 22: Crosscorrelation matrix of ULT from the remote model. Correlation of time series at station 15 versus all other stations along the coast (see Table 1).

by the ULT crosscorrelation matrix (Fig. 22). The slope of the maximum correlation ridge, in contrast to that of the locally forced model (Fig. 18), does indicate a fast propagation in agreement with the theoretical Kelvin wave speed.

In the annual and interannual time scale sense, the coastal propagation is very fast. The difference in speed of propagation between coastal Kelvin waves and westward annual and interannual Rossby waves is such that, from the point of view of the latter, upwelling and downwelling disturbances appear almost simultaneously all along the coast. Fig. 21 shows a downwelling band a few degrees west of the coast. This event was at the coast the previous year. The time interval represented in Figure 21 is not large enough to show any propagation of this band but, by the latitudinal variation on the position and form of the disturbance, it can be identified as a westward propagating Rossby wave. Note the decrease in separation between the downwelling pattern and the coast from south to north. Once separated from the coast, the anomalies continue westward propagating in the form of free waves. Figs. 23-24 show two representative results from the remotely forced model. Both figures represent snap-shots of ULT anomalies for February 9; Fig. 23 is for 1968 and 24 for 1975. The pattern is very similar: meridional bands of positive and negative anomalies extending over the whole domain with its magnitude decreasing to the north and west. In both figures, for 1968 and 1975, there is a large positive anomaly more or less at

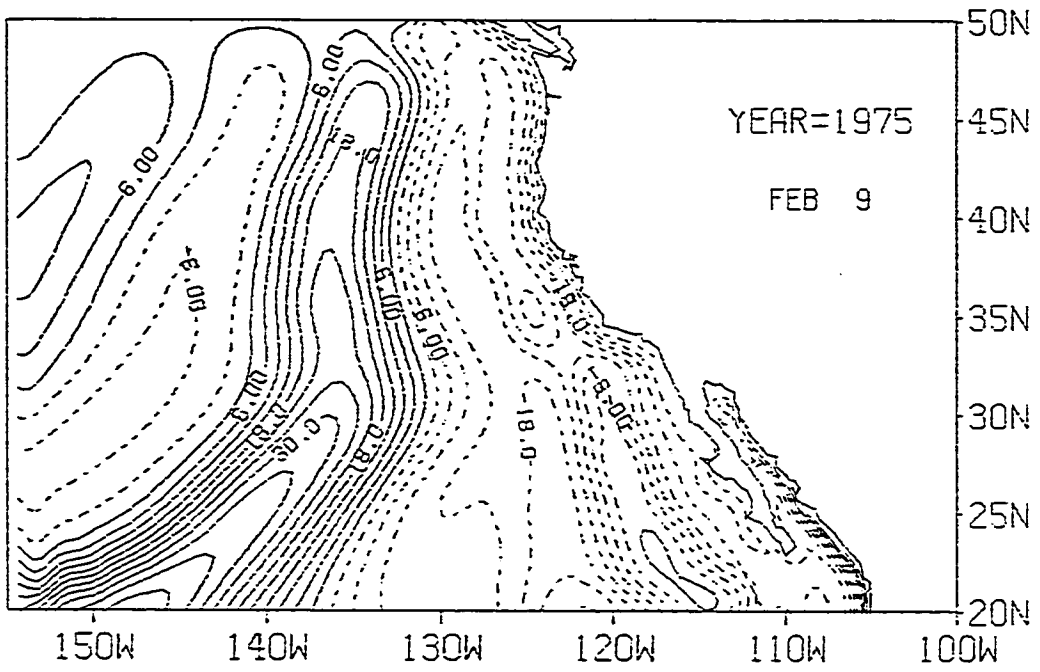

Fig. 23: Typical ULT contour from the remote model. Snap-shot for February 9, 1968.

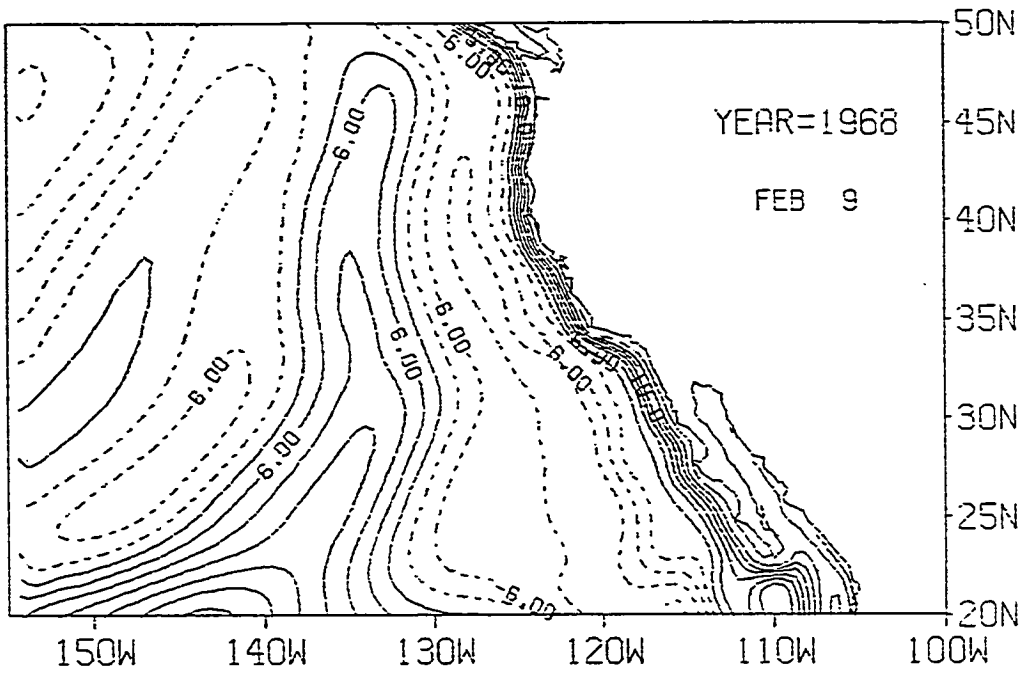

Fig. 24: Same as Fig. 23 but for February 9, 1975.

the center of the domain that corresponds to the large positive anomalies occuring at the coast in 1965 and 1972 respectively (i.e. El Niño events). The different speed of propagation with latitude is again evidenced by the sloping of the latitudinal bands. In Figure 23, a strong negative anomaly is observed at about 120-130°W; this corresponds to the strong downwelling event (anti-El Niño) occuring at the coast in 1973. The weak positive anomaly in the western region, starting at the western boundary at around 30°N and 40°N in Figure 23 and 24 respectively, corresponds to anomalies that were at the coast in 1963 and 1964 respectively.

All the information contained in these plots and in the remote model in general comes through only 500 km of the southern boundary, and this information (at least its low frequency) in turn is primarily of equatorial origin and more specifically generated at the western equatorial region by relaxation of the westerly winds. These results show a possible dynamic mechanism for the connection of equatorial El Niño event with north Pacific El Niños, i.e. an oceanic teleconnection.

The degree of correlation between our results and observed time series along the coast is analyzed in the next section, while in chapter V we discuss the westward propagation of energy.

c) Model/observations Intercomparison

Time series of monthly observed sea surface elevation at several stations along the coast were obtained (Wrytki, personal

communication). Four stations were used for the analysis: Crescent City (CC), Neah Bay (NB), San Francisco (SF) and San Diego (SD) (see Fig. 3). These stations were chosen because they have the longest records and represent the latitudinal variation of the area of interest. Lack of a long enough series prevents us from using other stations south of SD.

To compare with observations, model ULT anomaly data was transformed to sea surface elevation anomalies (SSHA) by multiplying by the density gradient between the two layers of the model, i.e.

$$SSHA = \frac{\Delta\rho}{\rho} \text{ (ULT anomaly)}$$

As an example of the resulting series, Crescent City's observed and model calculated SSHA are shown in Figure 25. The overall visual correlation in phase and amplitude is good in most years. Particularly good agreement of the amplitude and timing of the negative anomalies is evident. For example, the anomalous lows (more than 120 cm) in 1964, '68, '70, '73, '77, '78 coincide in both observations and model.

For a more effective visual comparison, the time series were divided in three parts:

1) the composite long term monthly means;
2) the low frequency series, in which the series is low passed filtered using an spectral filter with a stop frequency of 1 cycle/year and a pass frequency of .5 cycles/year.
3) the high frequency series, obtained by subtracting the low

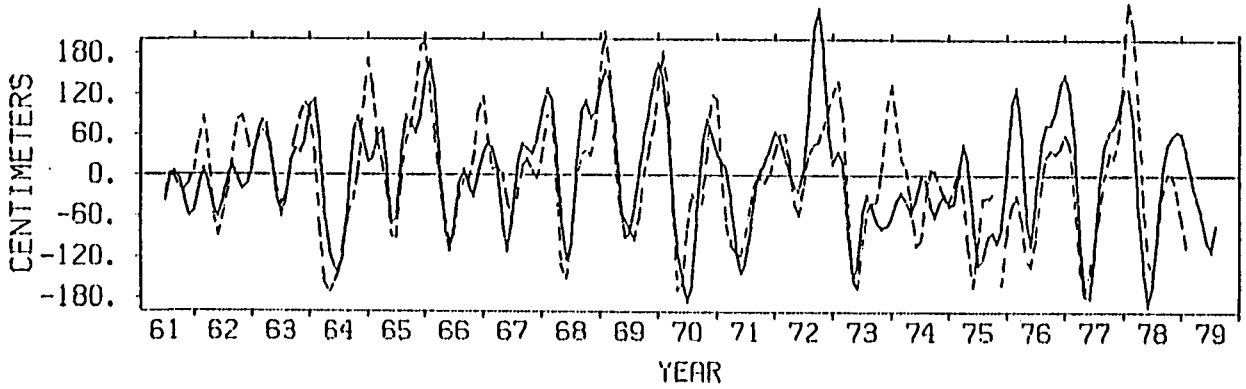

Fig. 25: Comparison of sea surface height anomalies observed (dashed line) and modelled for Crescent City.

frequency series from the total series.

Strong similarities between modeled and observed seasonal patterns are revealed. For SD, both model and observed SSH composite mean show a minimum in April-May and an increase to a maximum in August-September (Fig. 26); the observed SSH decreases monotonically from August to the April minimum; while in the model SSH it stays more or less constant until January and then decreases until April. The amplitudes are similar in both cases. For SF and CC, model and observed SSH annual cycle (Fig. 27 and 28) are remarkably similar both in phase and amplitude. There is a minimum of about 8-9 cm in April-May, an increase to a maximum in August-September and a second maximum in January. CC secondary peak is stronger than in SF, and it is well represented by the model. For NB (Fig. 29), the amplitude is bigger, and the minimum and zero crossing are shifted to the right (occurs later in the year) both in the observation and the model. The model misses the large peak in December shown in the observed data.

Using steric height anomalies, Reid and Martyla (1976) described the seasonal characteristics of sea surface elevation along the California coast. They showed that contrary to the eastern coast of the United States and further south in western America, the sea surface elevation annual cycle is out of phase with the heating-cooling cycle (i.e. maximum elevation in late summer or early fall and a minimum elevation in winter; Reid and Martyla, 1976). Simpson (1983) shows that the seasonal temperature anomalies in the California

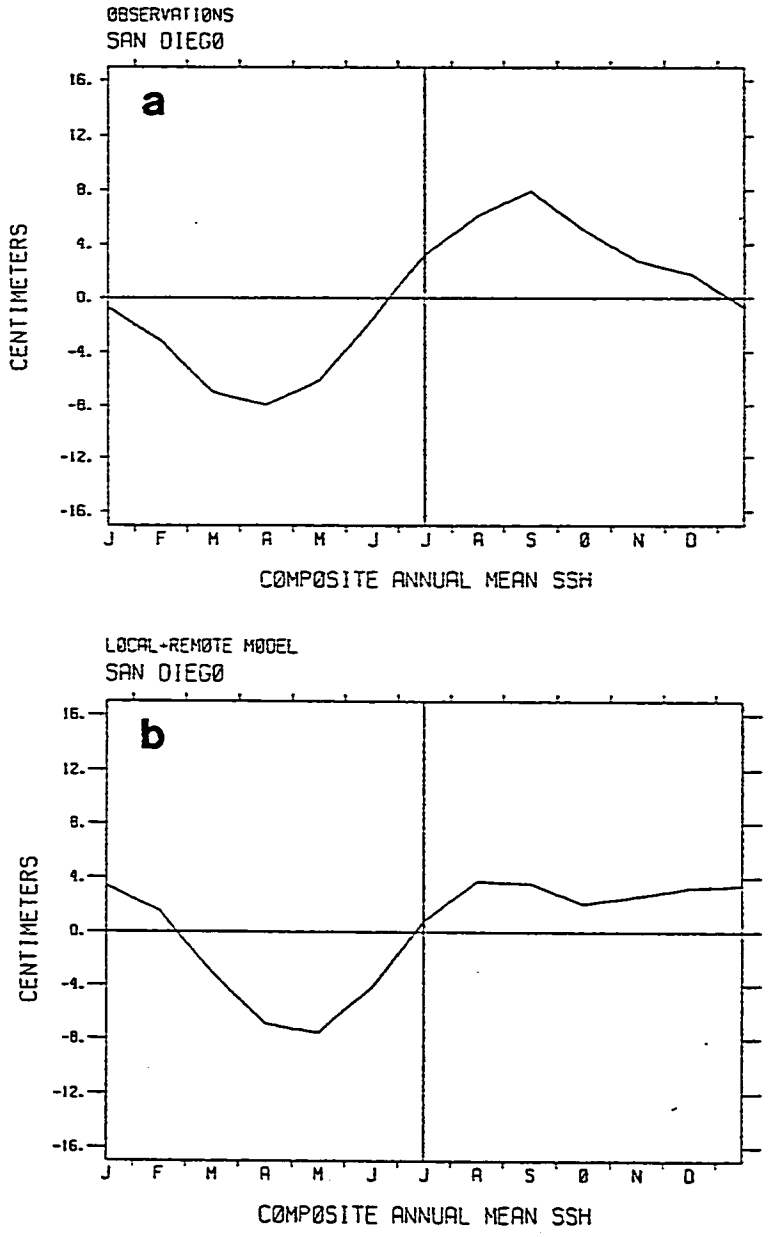

Fig. 26: San Diego's composite annual mean SSH anomalies from a) observations and b) local+remote model.

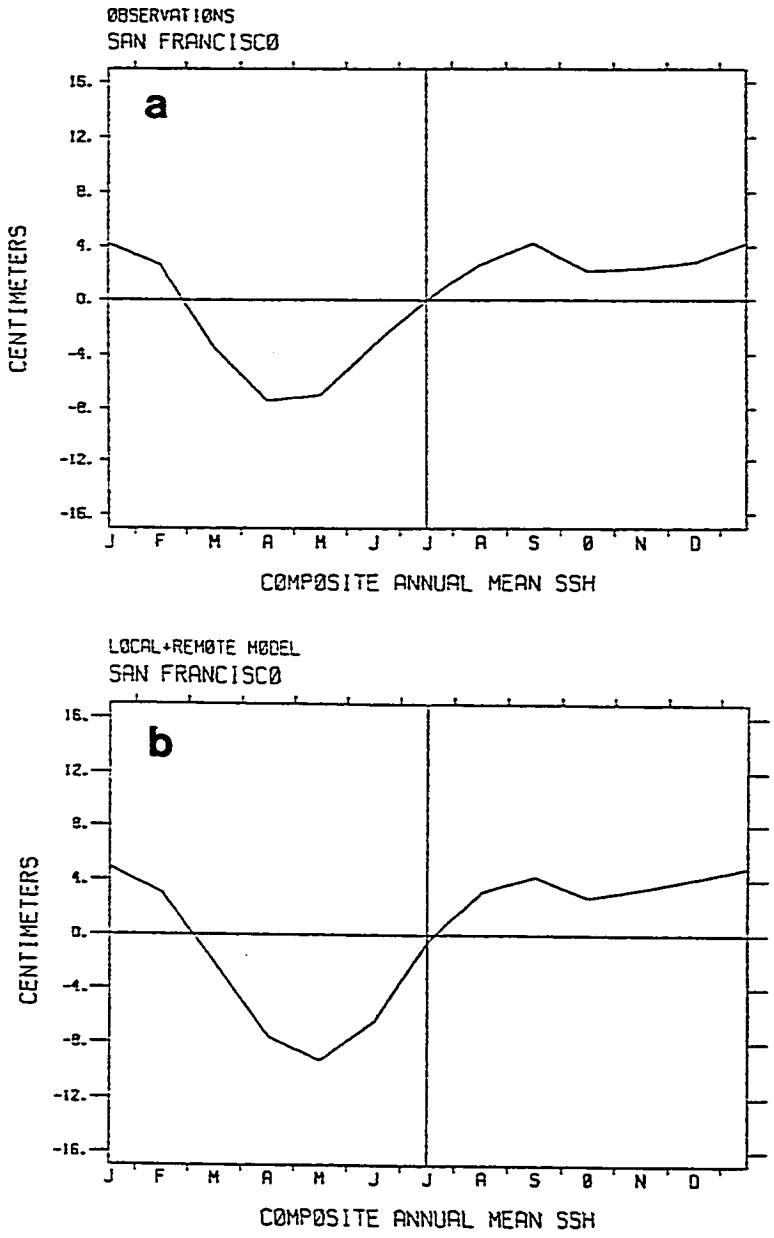

Fig. 27: Same as Fig. 26 but for San Francisco.

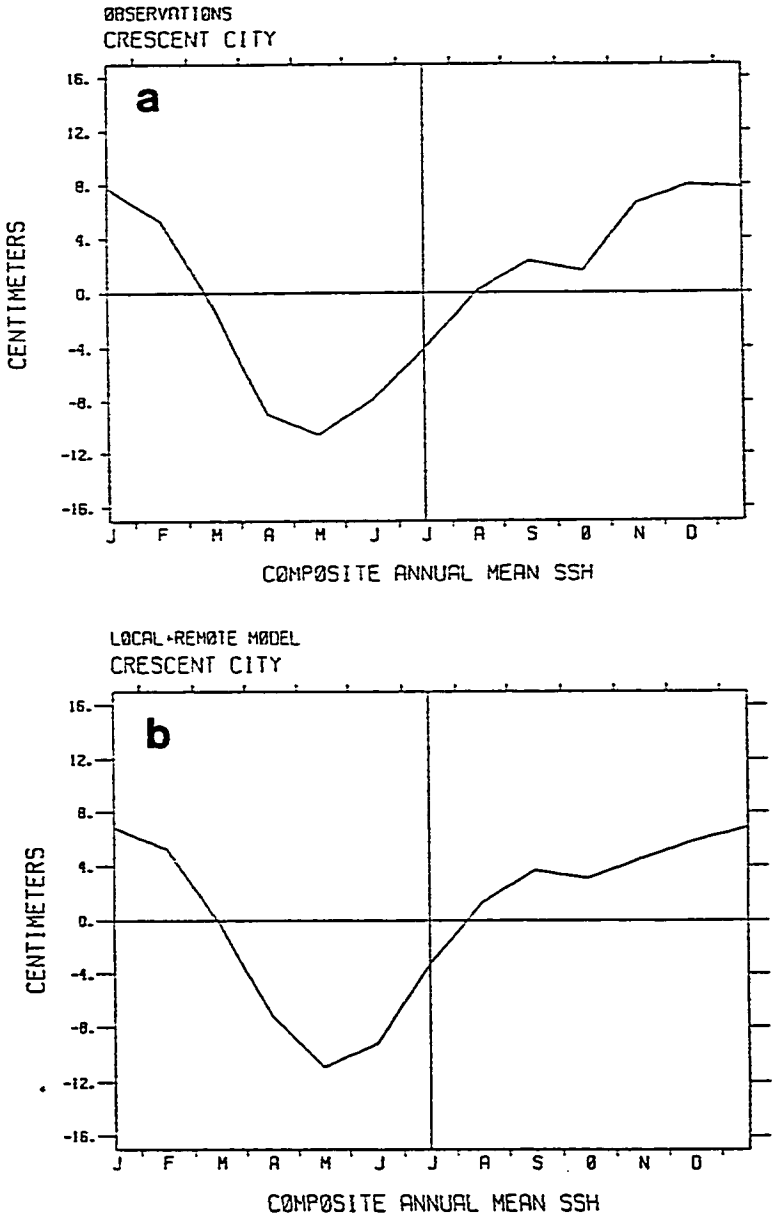

Fig. 28: Same as Fig. 26 but for Crescent City.

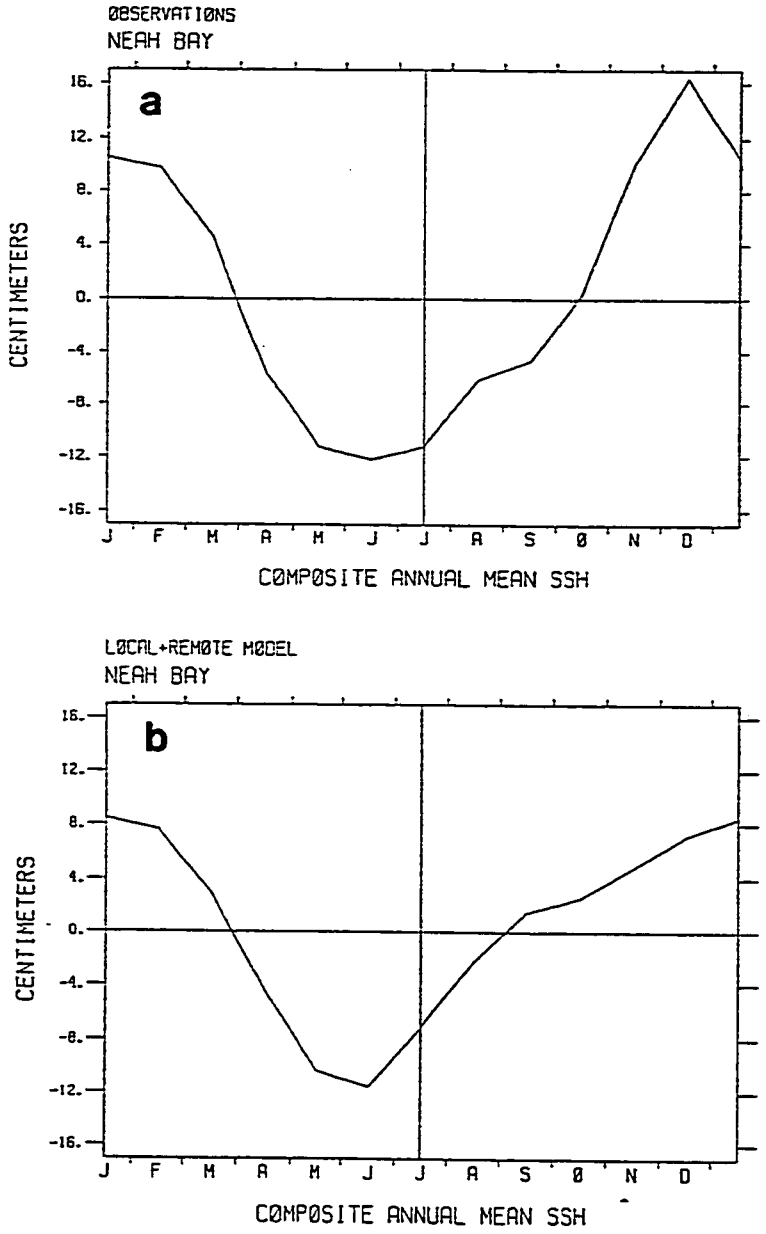

Fig. 29: Same as Fig. 26 but for Neah Bay.

Current, which follows the SSH seasonal cycle, were produced dynamically rather than thermodynamically.

The model seasonal pattern is completely due to dynamical mechanisms. The fact that the model reproduces the annual cycle so well supports the theory of the seasonal cycle of SSH along the western part of North America being mostly due to dynamical causes. This is true even for SD where the seasonal cycle "resembles the annual heating and cooling cycle" (Reid and Mantyla, 1976).

For most of the period, there is a high visual correlation at the four stations compared between the model and observed high passed filtered SSH series (Fig. 30). Especially well similated are the upwelling events in the northern stations (CC and NB) (Fig. 30c and 30d). This points to the importance of the equatorward wind forcing in the area and its proper implementation in the model. For most of the years the upwelling events (negative anomalies) have a shorter time scale and larger amplitude than the downwelling events (positive anomalies). This is also reflected in the composite means (Fig. 26-29) and is more evident in the two southern stations (SF and SD) where the two yearly maximums are more pronounced.

For year '74 and '75 the model results do not follow the observations. The annual cycle in our model breaks down for those years. At least in the SF series (Fig. 30b), it seems that this perturbation of the annual cycle is also present in the observed series. The amplitude and phase become erratic for 1974 and 1975 in

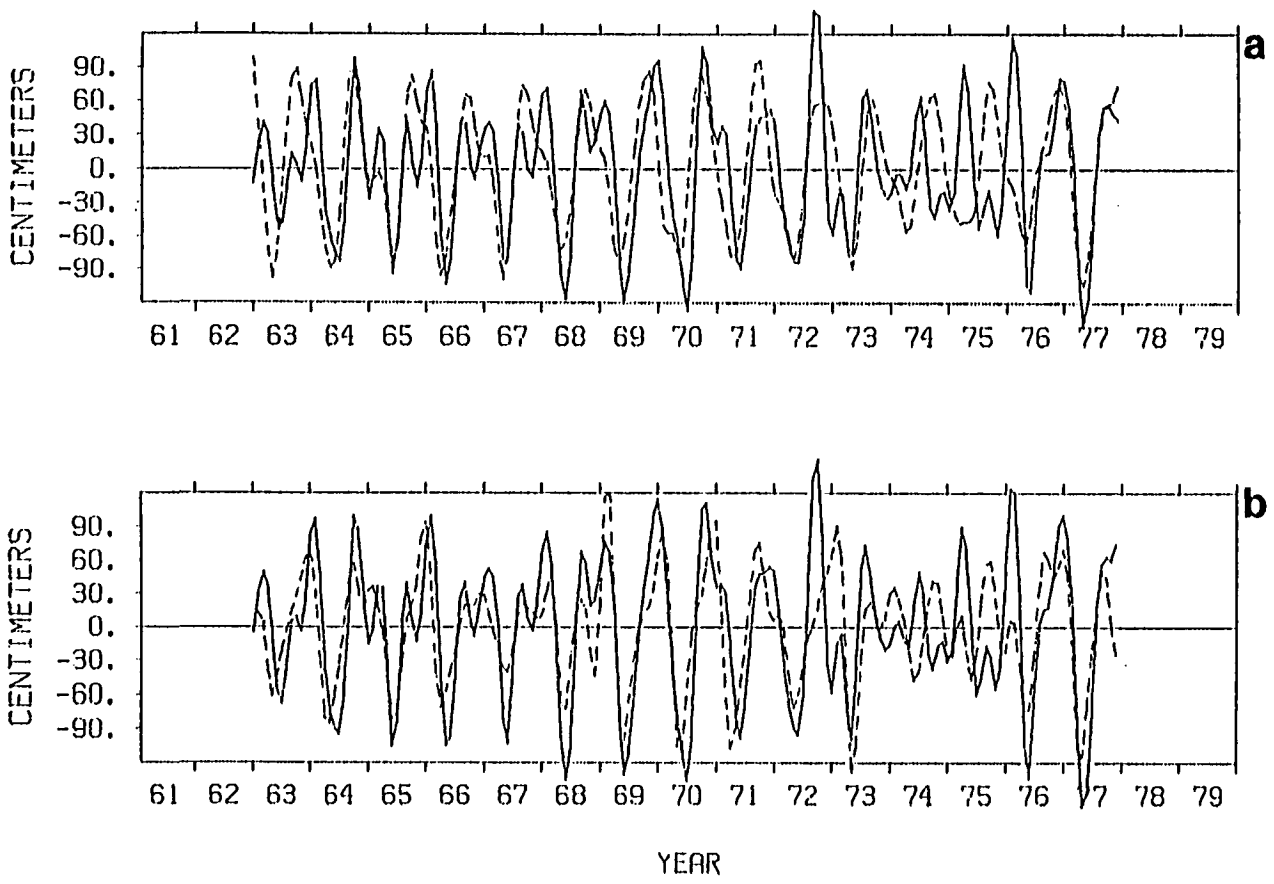

Fig. 30: Comparison of observations and model (dashed line) high pass filtered (total signal minus low pass filtered) series of SSH for a) San Diego, b) San Francisco, c) Crescent City, and d) Neah Bay. A low passed filter with a pass frequency of $2\pi/2$ years^{-1} and a stop frequency of $2\pi/1$ years^{-1} was used. Note different scale for Neah Bay.

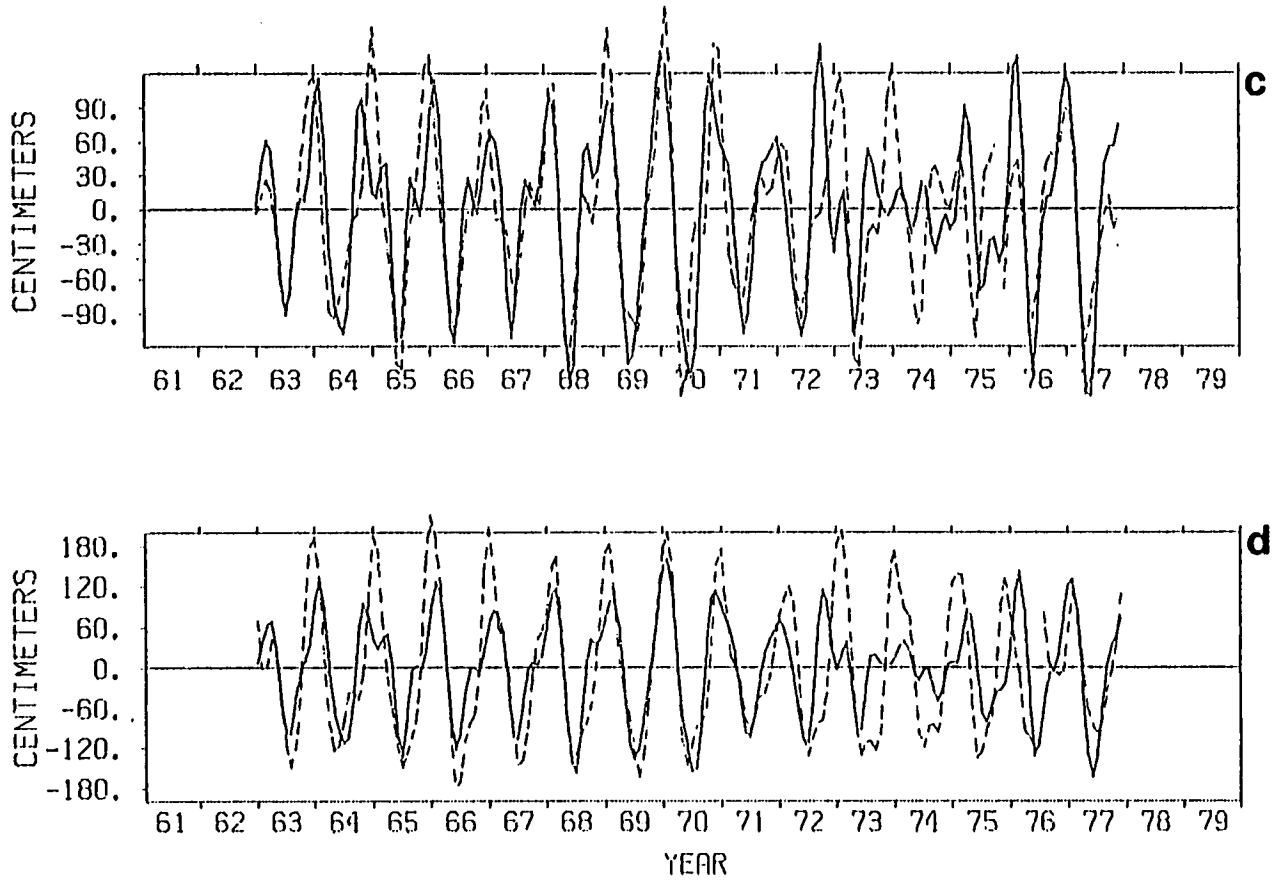
c
CENTIMETERS
90.
60.
30.
0.
-30.
-60.
-90.
61 62 63 64 65 66 67 68 69 70 71 72 73 74 75 76 77 78 79
d
CENTIMETERS
180.
120.
60.
0.
-60.
-120.
-180.
61 62 63 64 65 66 67 68 69 70 71 72 73 74 75 76 77 78 79
YEAR

both observations and model. In our model, this is the result of the local and remote seasonal cycle becoming out of phase. Indeed, from the separate contributions of each process (Fig. 31) it can be seen that the change at '74 and '75 is due to the cancelling effect of each signal. Most of the years both the local and remote signal reinforce each other, but for the '73-'74, '74-'75 period the remotely forced signal gets out of phase with the wind driven signal (which maintains its average amplitude and phase) and cancels the total signal. The fact that the observed annual cycle also shows symptoms of disturbance for those years might indicate that the linear cancellation (or reinforcement) mechanism between local and remote signals is a viable one in the California Current region. A complex de-modulation analysis of the series around the annual frequency could be useful to further analyze this point.

The amplitude of the annual signal due to each process is of comparable magnitude as seen from Fig. 31. From visual comparison it seems that there is more semiannual variability in the model than in the observations. Most of the semiannual variation in our model comes from the equatorial signal.

Low passed filtered time series of SSH anomalies are plotted in Figure 32. Again there is a good agreement between model and observations. El Niño events of 1964, '65-'66, '72 and '76 reflected in the data as positive anomalies are reproduced by the model. The largest anomaly in both series is at '72, year of the strongest El

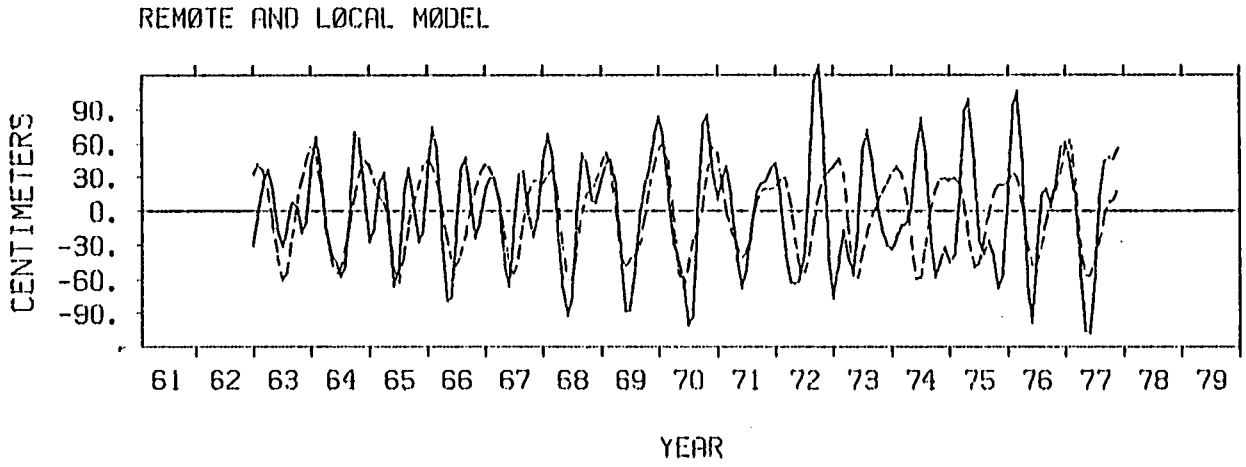

Fig. 31: Comparison of the contribution from the local (dashed line) and remote models to the high pass filtered SSH anomalies at Crescent City.

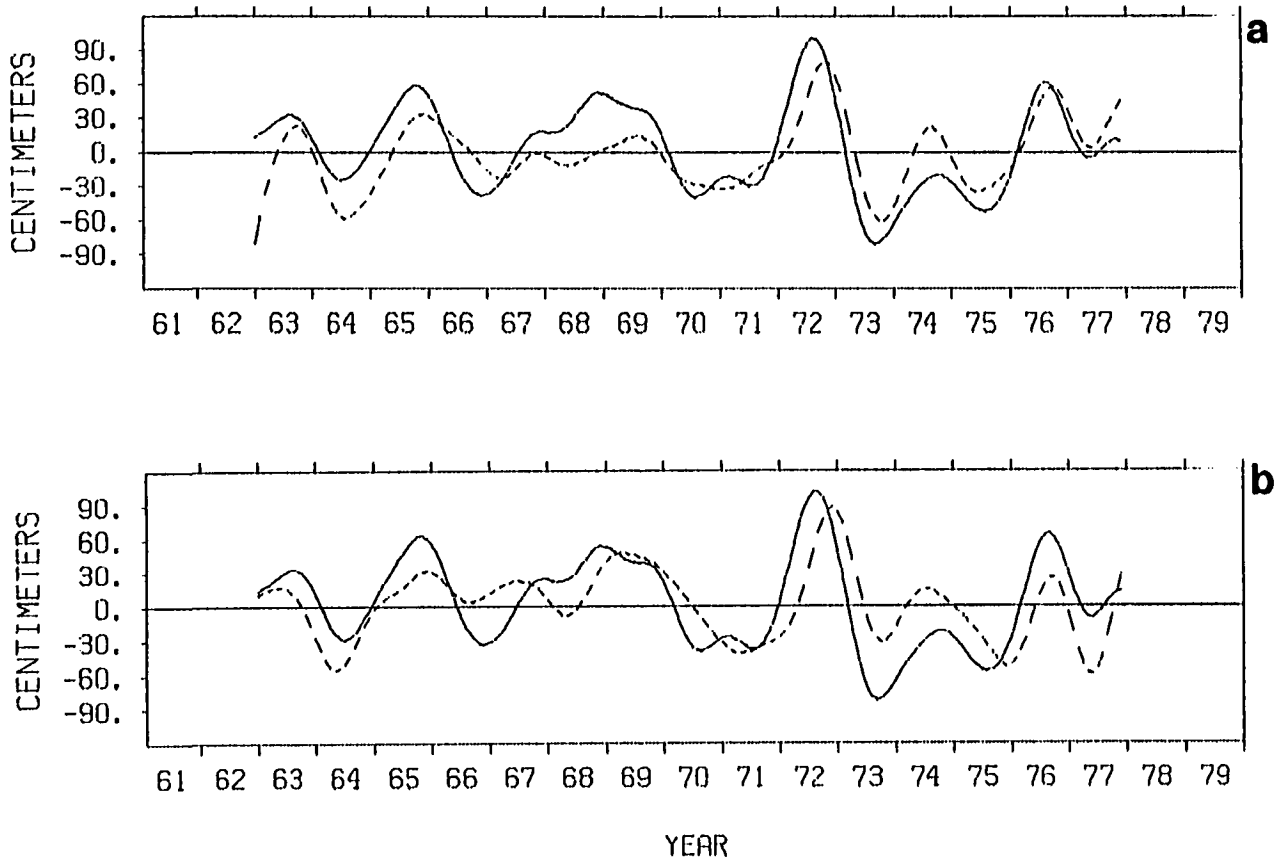

Fig. 32: Comparison of observations (dashed line) and model low pass filtered series of SSH for a) San Diego, b) San Francisco, c) Crescent City and d) Neha Bay. An spectral low pass filter with a stop frequency of $2\pi/1$ years^{-1} and a pass frequency of $2\pi/2$ years^{-1} was used.

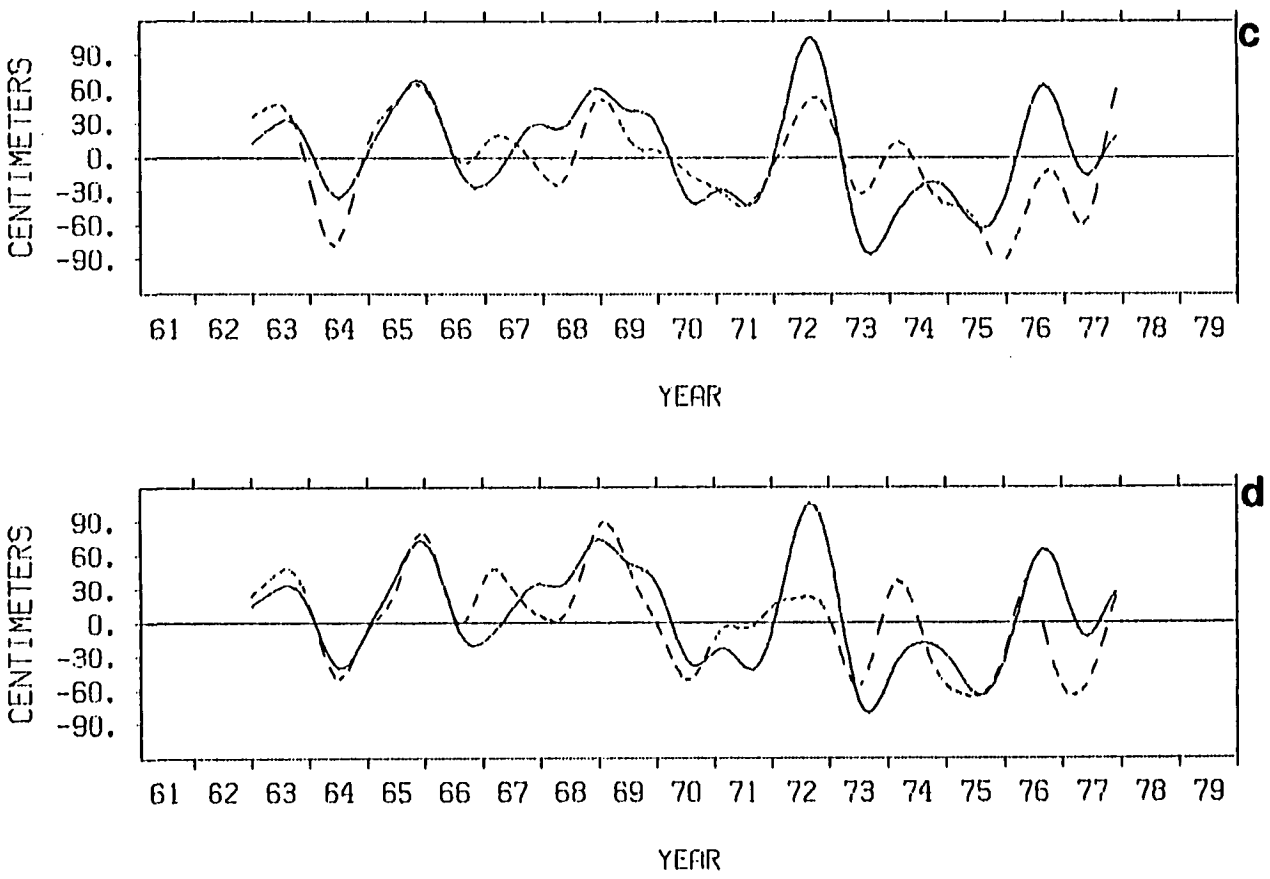
c
CENTIMETERS
90.
60.
30.
0.
-30.
-60.
-90.
61 62 63 64 65 66 67 68 69 70 71 72 73 74 75 76 77 78 79
YEAR
d
CENTIMETERS
90.
60.
30.
0.
-30.
-60.
-90.
61 62 63 64 65 66 67 68 69 70 71 72 73 74 75 76 77 78 79
YEAR

Niño before the 1982 event. For the two southern stations, the amplitude is very similar. A major difference between the two series is the consistently low model SSH at '66-'67, while the observed data shows near zero or even positive anomalies. This is more pronounced at the northern stations. Also, the magnitude of the 1972 event fails to diminish to the north as the observations do. It seems from visual inspection that the correlation of the low passed frequencies series decreases to the north.

Comparing the contribution to the low frequency anomalies from each mechanism (local vs. remote) (Fig. 33), it is evident that, in contrast to the annual frequency, most of the energy in the El Niño frequency band in the region is of equatorial origin.

To investigate this point further and quantify the different contributions, spectral and crossspectrum analysis were performed.

Spectra were calculated for each model (L, R, L+R) and observations time series at the four stations: NB, CC, SF and SD (Figs. 34-37). Standard smoothing in frequency was done using a 13 band-span Hanning window (26 d.f.) (eg. Bendat and Pearsol, 1971).

For the local model, at all the stations the dominant frequency is the annual with a smaller but significant peak at the semiannual frequency. The background spectrum is red (i.e. energy increases toward the low frequencies), and only at the annual frequency are the spectrum from the local and remote model of comparable magnitude. For the remote model, the energy at the semiannual, annual, and the 2-4

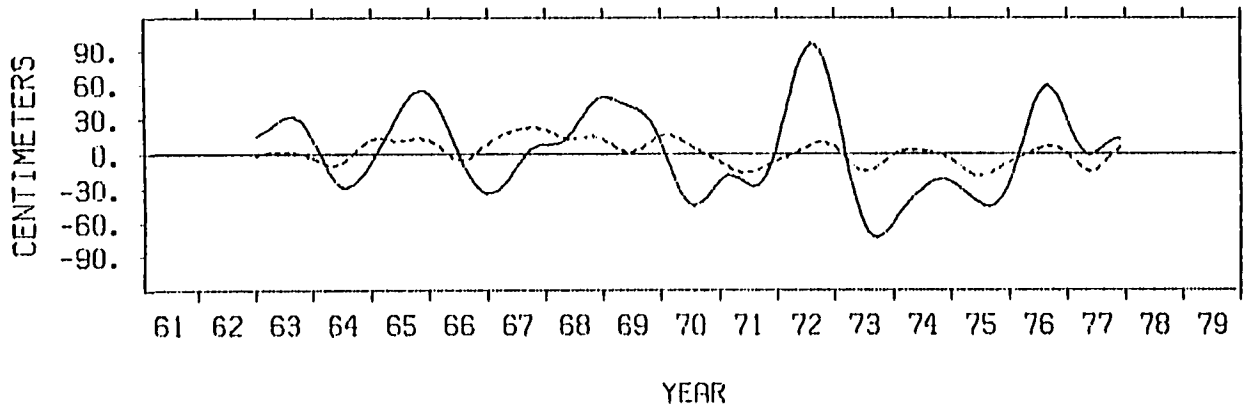

Fig. 33: Comparison of the contribution from the local (dashed line) and remote model to the low pass filtered SSH series at San Francisco.

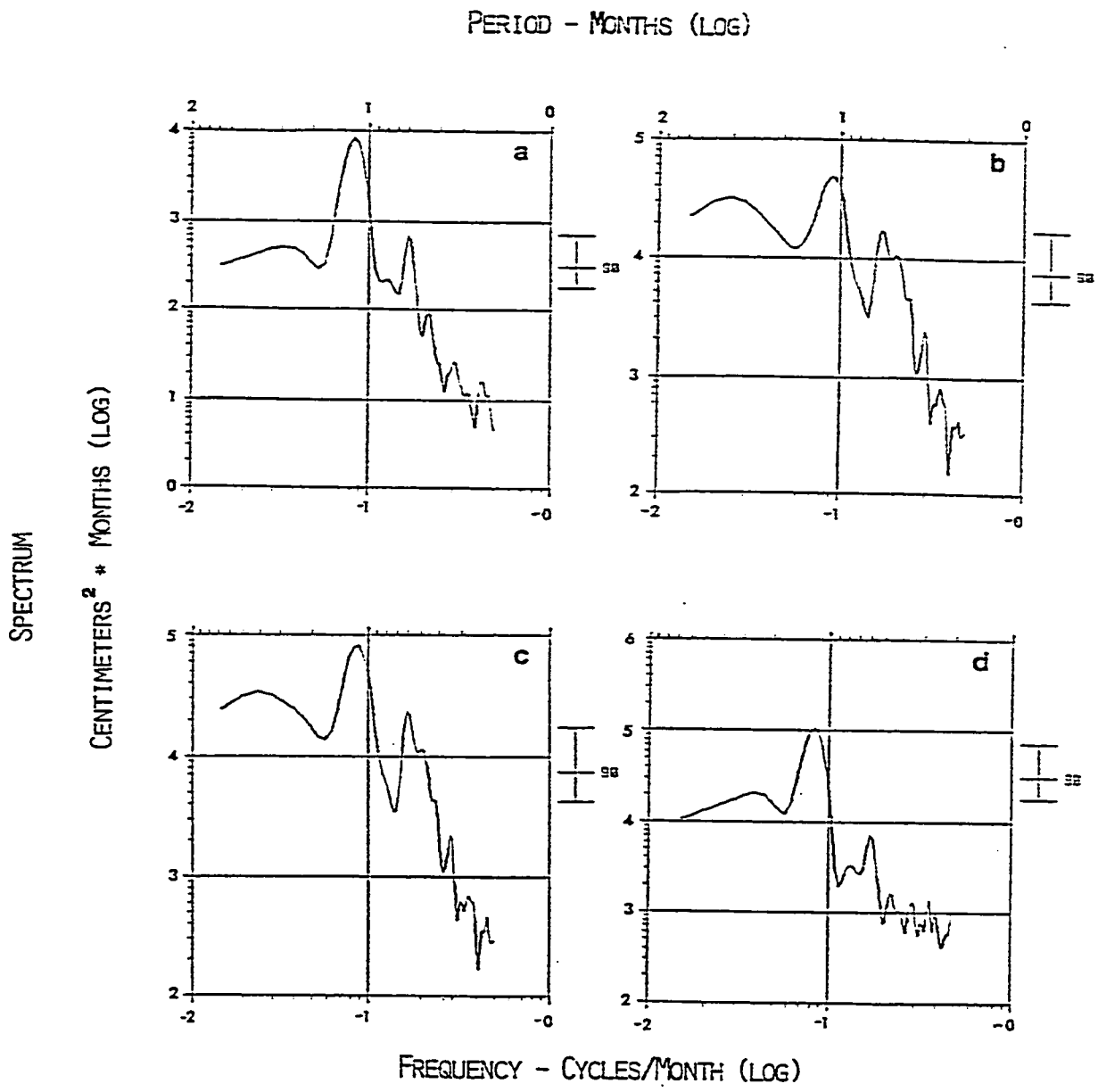

Fig. 34: San Diego's SSH spectra from a) local model, b) remote model, c) local+remote model and d) observations. Note that different scales were used for each spectrum. The 90% confident intervals are shown to the right of each spectrum.

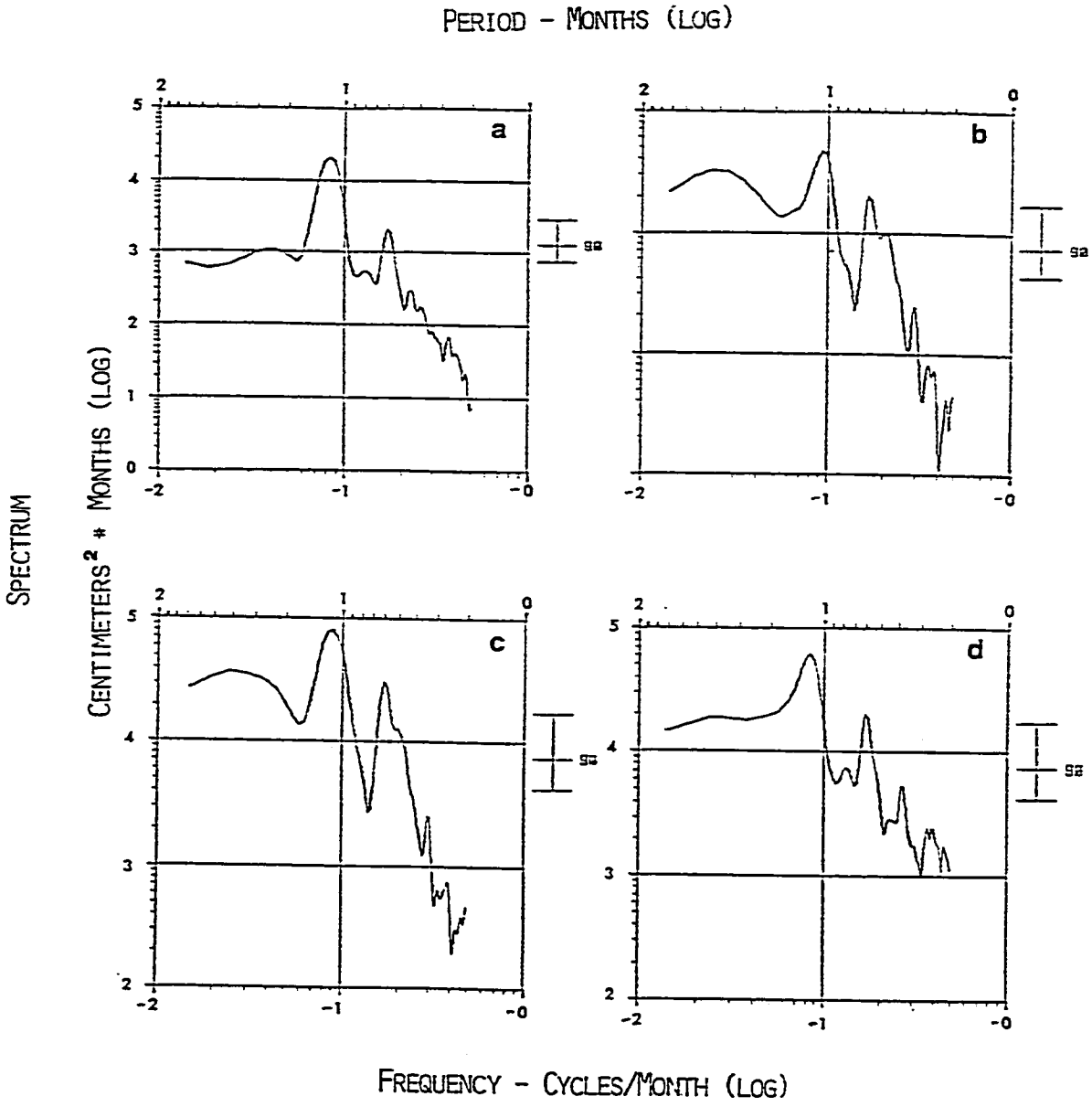

Fig. 35: Same as Fig. 34 but for San Francisco.

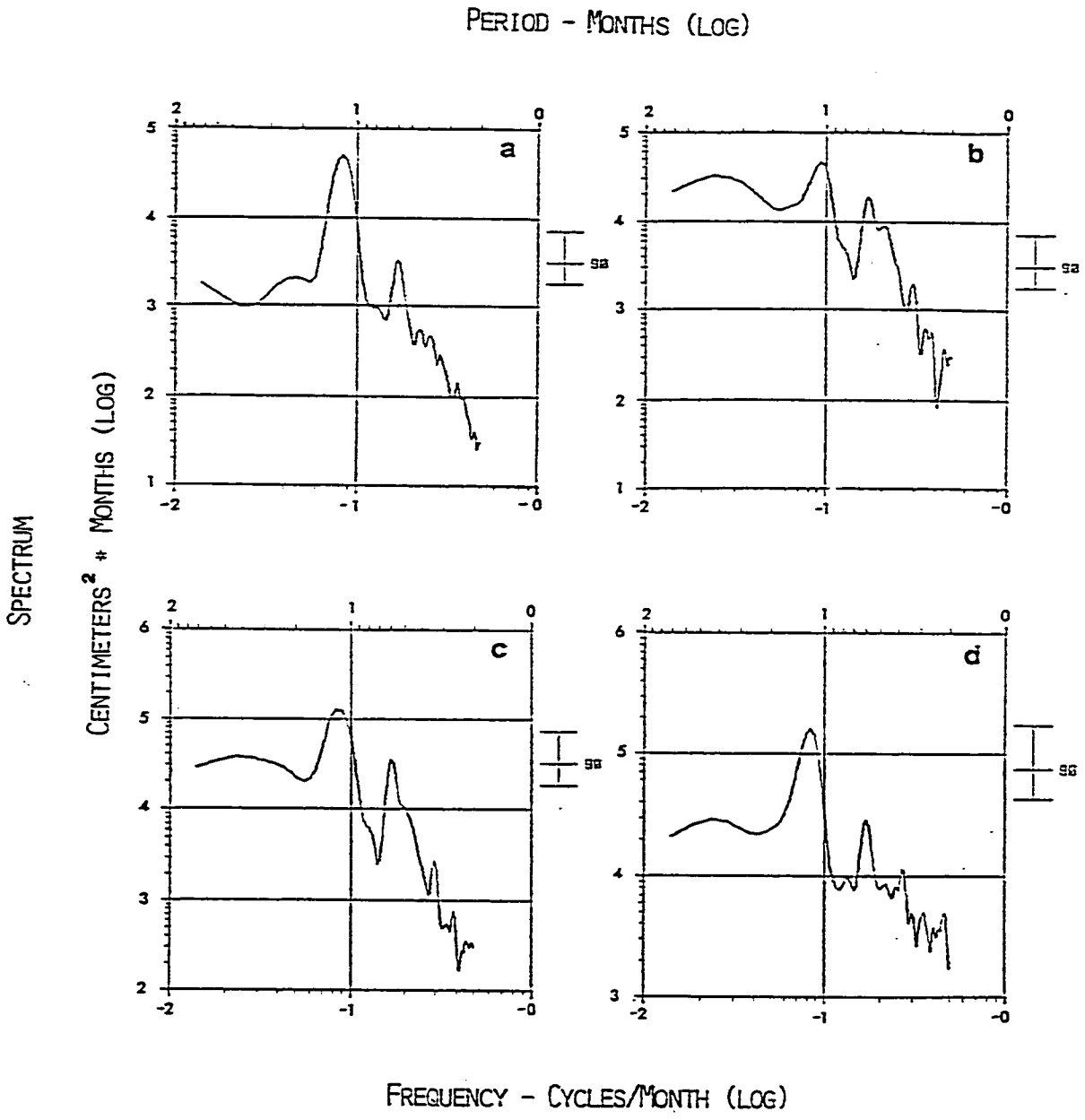

Fig. 36: Same as Fig. 34 but for Crescent City.

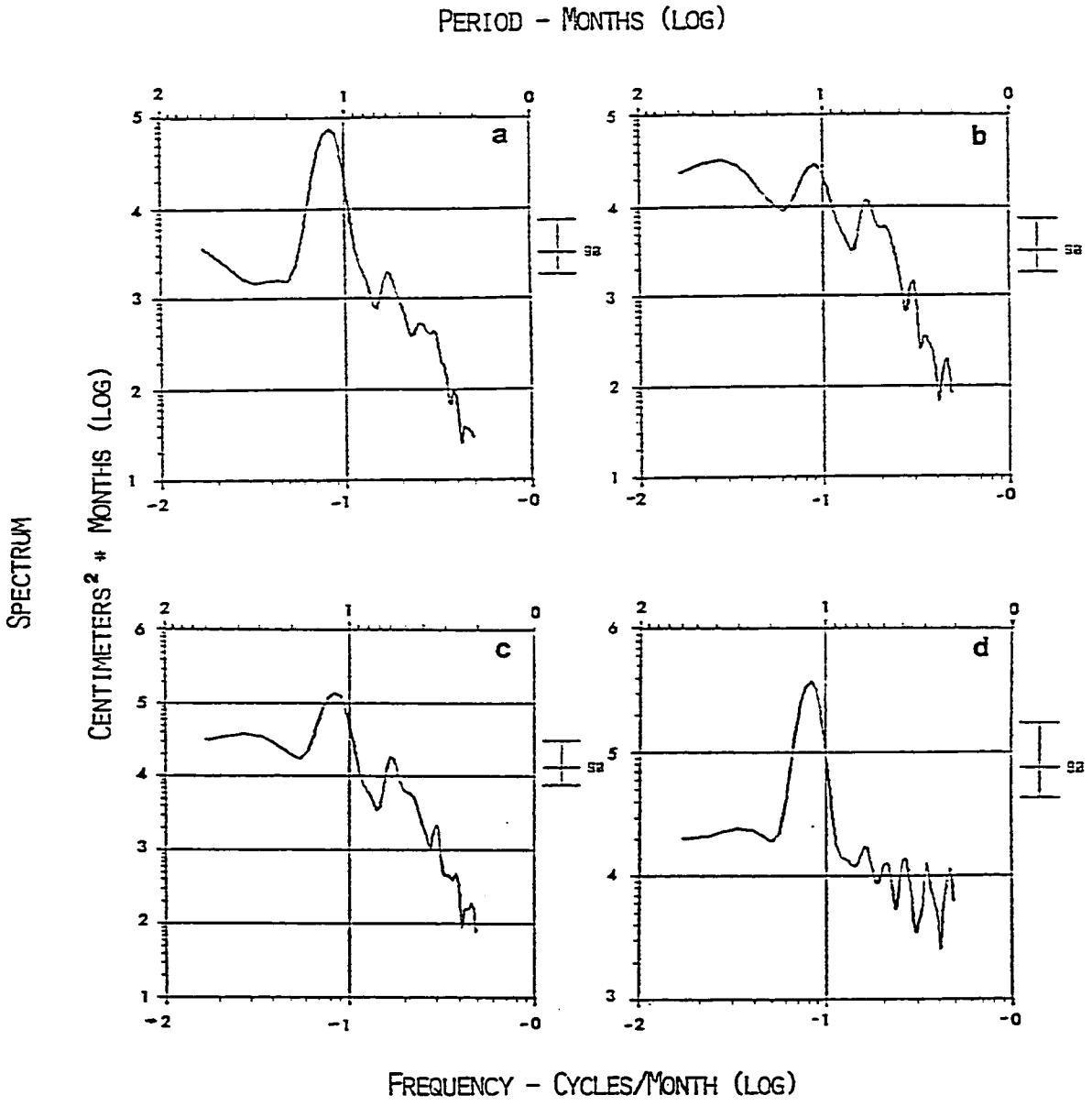

Fig. 37: Same as Fig. 34 but for Neah Bay.

cycles/year frequency band are of similar magnitude, the background energy, as for the local model, increases toward the low frequencies, but the amplitude is at least an order of magnitude bigger. This magnitude dissimilarity results in the L+R model spectrum being dominated by that of the R model, except at the annual frequency. For the semiannual and lower frequencies, the shape and magnitude of the L+R spectrum is similar to that of the observations, but for the higher frequencies (higher than semiannual), the energy drops much more in the first than in the later, evidencing the narrower frequency band response of the model.

The spectrum variation with latitude is mainly in the magnitude of the annual peak. The magnitude of the annual peak increases to the north in observations and model spectrum and, as could be expected, its increase in the model is due to an increase in the local wind-driven model.

Coherence square functions $\left(\gamma^2_{sq}(f)\right)$ and frequency response functions $\left(H_{sq}(f)\right)$ defined as:

$$\gamma^2_{sq}(f) = \frac{S^2_{sq}(f)}{S_{ss}(f)\, S_{qq}(f)} \qquad 16$$

$$|H_{sq}(f)|^2 = \frac{S_{qq}(f)}{S_{ss}(f)} \qquad 17$$

where $S_{sq}(f)$ is the cross spectrum between series s and q, were calculated. At each station (NB, CC, SF and SD) the cross-spectrum

functions γ^2 and H^2 were computed between the observed SSH time series as were:

1) SSH time series from the remotely forced model
2) SSH time series from the locally forced model
3) SSH time series from the local+remote model.

Figure 38 shows the results for San Diego. As expected, from the visual inspection for the El Niño frequency band (2-4 years), there is a large coherence square (≈ .80) between observed time series and the remotely forced model (Fig. 38a). For the annual frequency, although still significant, the coherence is smaller (≈ .60). For the local model series, the opposite is true; there is a very strong coherence between observed and model data at the annual frequency, but no significant (at 50%) coherence at the low frequency band (Fig. 38b). The frequency response function represents the power ratio between two series at a given frequency. From Figure 38e (and 38b) it is clear that though the locally forced model is very coherent at the annual frequency (Fig. 38b), its energy is small ($H_{\ell o}$=3) compared to the energy at that frequency from the observations. In other words, if we assume there is a linear relation between the model output and the observations, Fig. 38e shows that the local model spectrum is about 1/3 of the observed spectrum. The result from the local+remote model vs. observation comparison (Fig. 38f) shows that the annual frequency energy is actually due to both mechanisms. The frequency response function is very near one, while the coherence square is still

Fig. 38: Coherence square function (CSF) and frequency response function (frf) between model and observed SSH at San Diego. a) CSF between observations and remote model. b) CSF between observations and local model. c) CSF between observation and local+remote model. d) frf between observations and remote model. e) frf between observation and local model. f) frf between observations and local+remote model. For the frf, the time series of observed values is assumed to be linearly related to the model time series. A value of 1 in the frf at a given frequency indicates the model and observations spectra contains the same amount of energy at that frequency. A value greater than 1 indicates the model underestimates the energy of the observations. The 2-4 years band (El Niño band) was shadowed and a line at the annual frequency drawn as a visual aid.

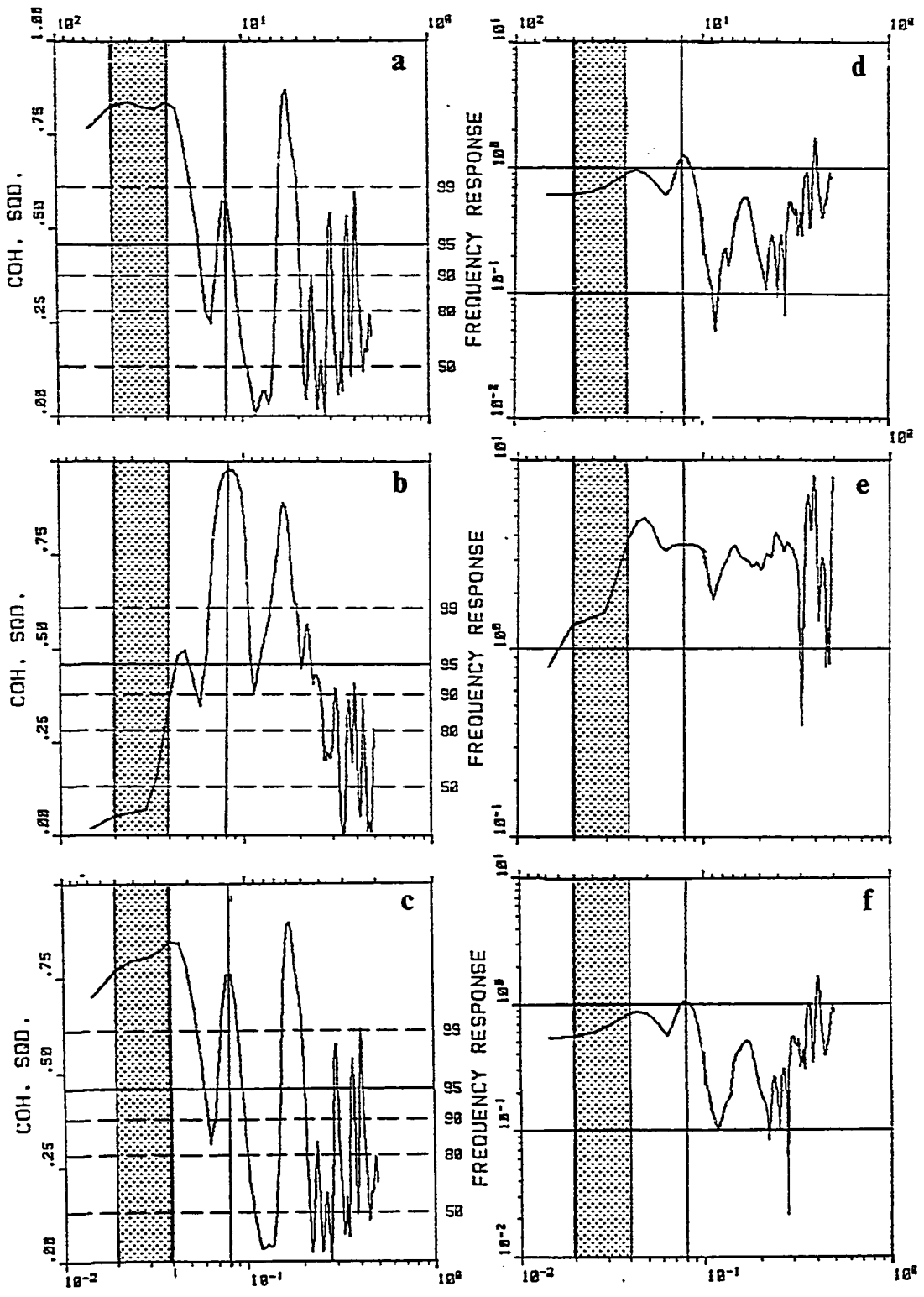
a
b
c
d
e
f
COH. SQD.
FREQUENCY RESPONSE

large (≈ .75). In summary, Figure 38f shows that the remotely forced model explains most of the variance (> 75%) in the observations in the El Niño frequency-band range, while for the annual frequency a combination of local and remotely forced signal explains also about 75% of the variance.

This general qualitative pattern of the coherence and frequency response function at San Diego is repeated in the other stations (Figs. 39-41). The remote model explains a large percentage of the variance in the low frequency band, and both remote and local explain the energy at the annual frequency. As hinted by the visual inspection of the SSHA series, Figure 38-41 show that for the local model the annual contribution becomes more important and the coherence increases to the north, while for the low frequency the coherence decreases. At Neah Bay the coherence square is still significant (> .40, significant at 90% PCC) for the El Niño frequency band while for the annual frequency it has gone up to more than .8 (Fig. 41c).

d) Westward Propagation of Energy

As shown in the monthly averaged SSH anomalies (Fig. 13), disturbances at the coast, either locally generated or propagated to the region in the form of coastally trapped waves, can radiate to the west and become a source of energy to the ocean interior. Observational evidence has demonstrated that most of the mesoscale variability in the thermocline of the mid-latitude Pacific is associated with long baroclinic Rossby waves (eg. Emery and Magaard,

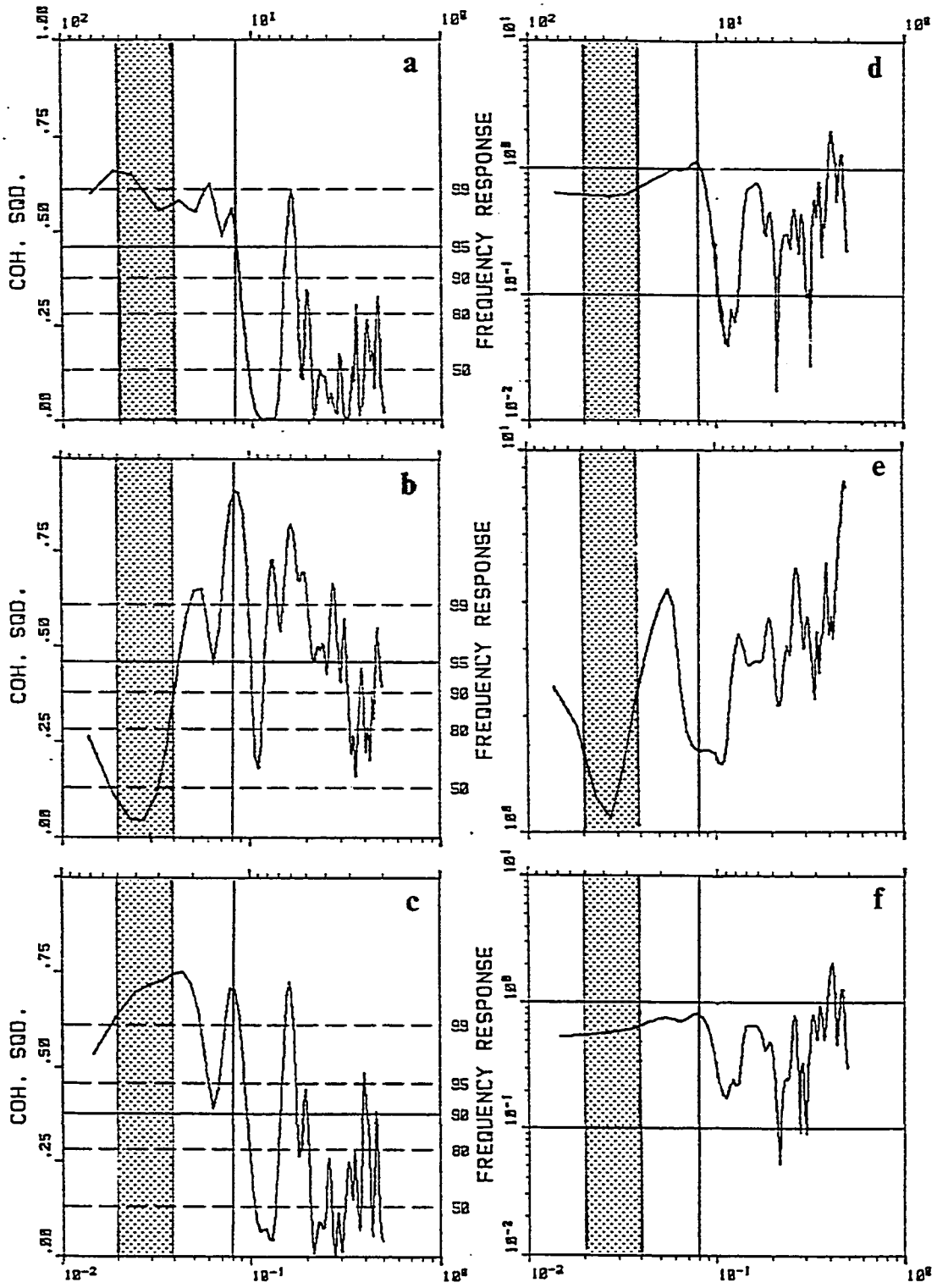

Fig. 39: Same as Fig. 38 but for San Francisco.

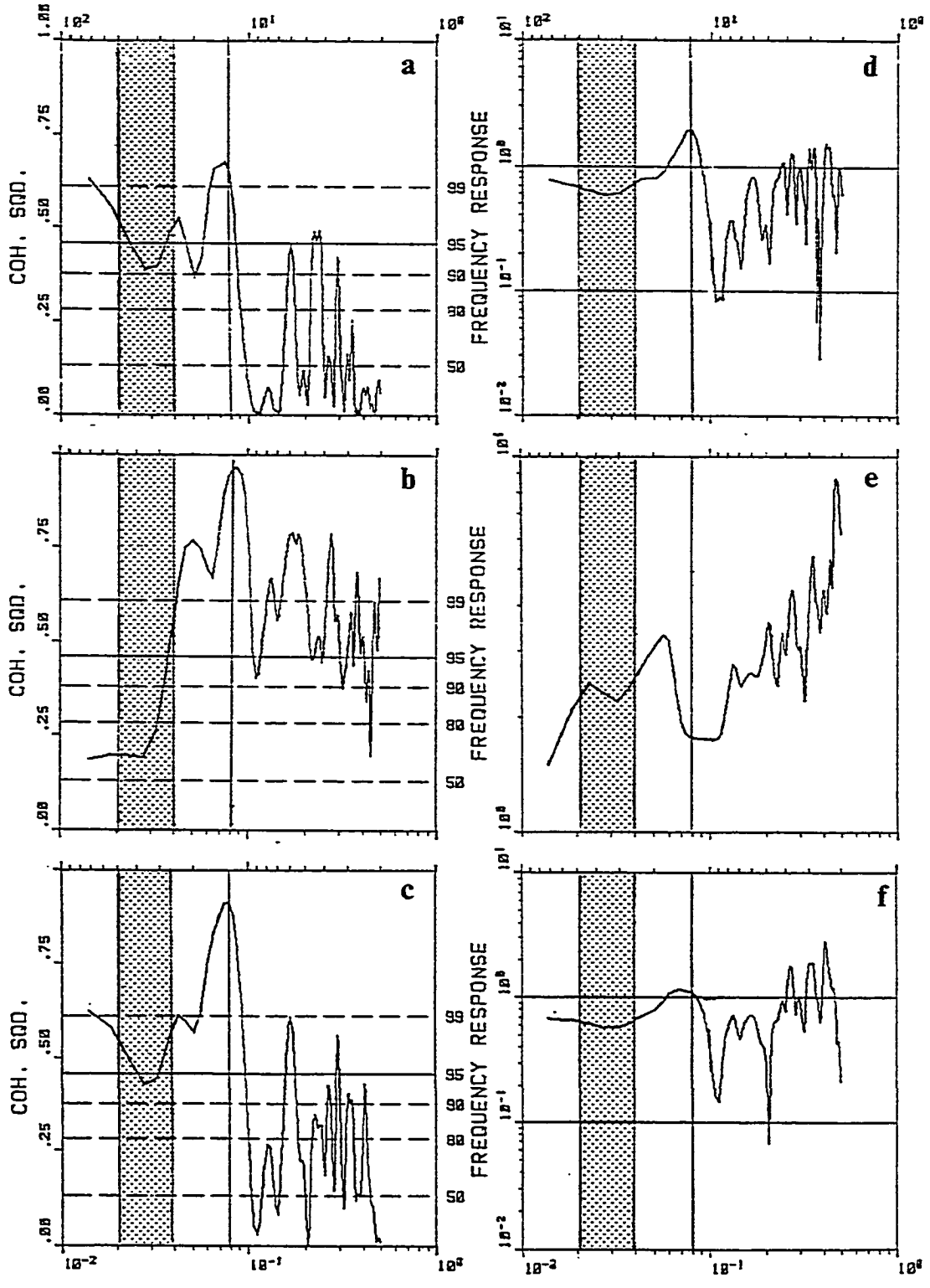

Fig. 40: Same as Fig. 38 but for Crescent City.

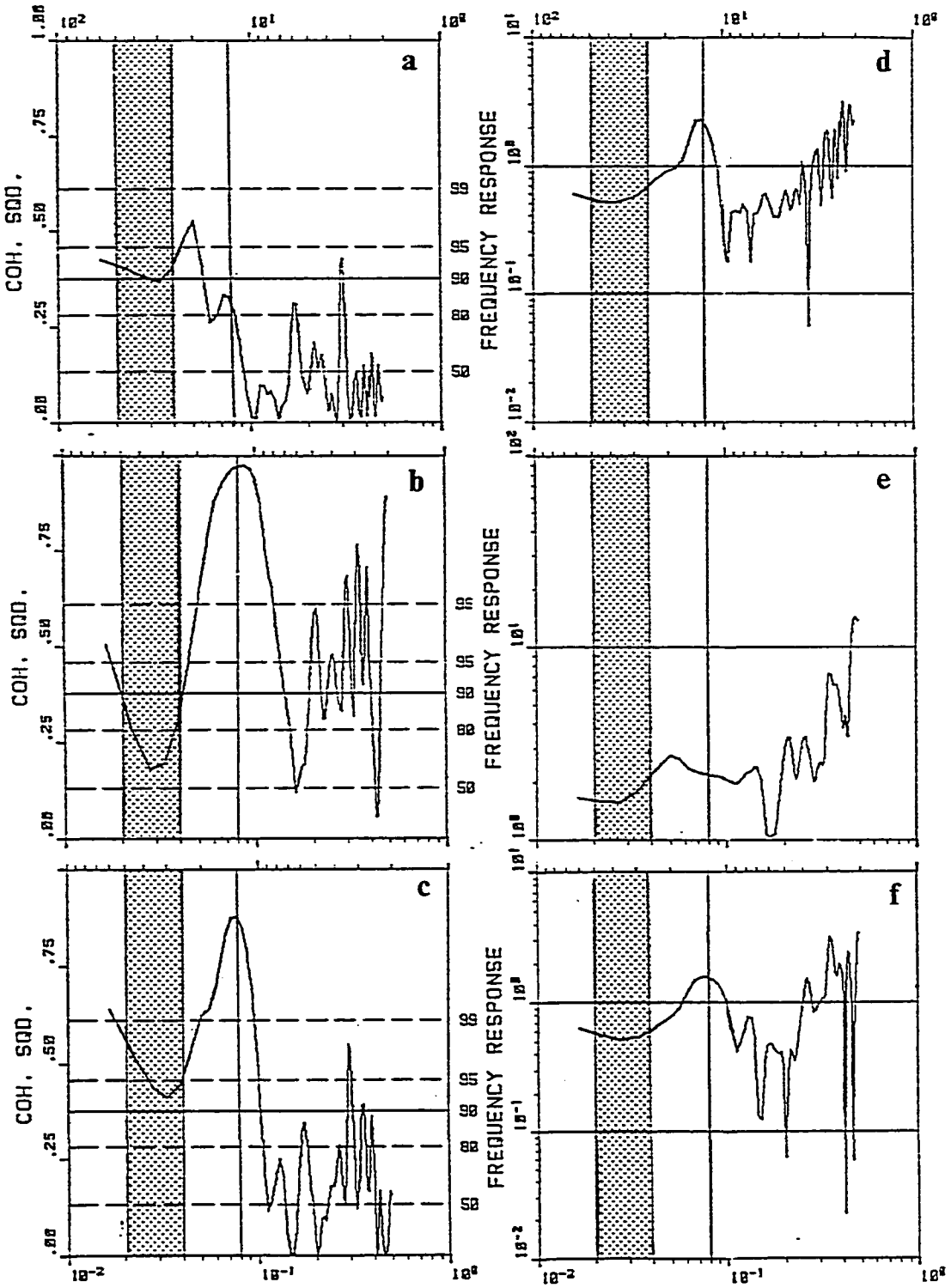

Fig. 41: Same as Fig. 38 but for Neah Bay.

1976; Price and Magaard, 1980; White and Saur, 1981). White (1985) classified the source of their generation in two types: 1) that due to Ekman pumping by wind stress curl and 2) that due to eastern boundary influence induced either locally or associated with remotelly forced variability.

Mysak (1983) proposed a mechanism by which the north-south fluctuation of the Eastern Boundary Current off Vancouver Island can efficiently generate first baroclinic mode Rossby waves throughout the central north Pacific. White and Saur (1981) used subsurface temperature and surface salinity observations along the great circle transect between San Francisco and Honolulu to investigate the source of annual baroclinic long waves in the eastern north Pacific. Their study demonstrates the importance of large-amplitude fluctuations of the wind curl in the vicinity of the eastern boundary as a source mechanism for Rossby wave energy. They do not rule out the possibility of some energy contribution by locally generated upwelling and/or internal Kelvin wave propagation. More recently, Cummins et al. (1986) simulated the annual Rossby wave field over a large part of the eastern north Pacific Ocean. Through numerical integration of the linearized, reduced gravity vorticity equation in spherical coordinates, they were able to indentify three dominating sources of Rossby wave energy: two along the coast, previously identified by other authors, and a mid-oceanic generation region. Their model includes realistic representation of the eastern boundary geometry.

Whatever their generation mechanism, away from the source the waves attain the form of free propagating Rosby waves whose characteristics, in a reduced gravity model, are given by eq. 14. The phase speed depends on latitude through the Coriolis parameter, i.e., for long waves:

$$C_{ph} = -\beta g' H \qquad 16$$

Killworth (1979) shows that the main effect of non-linearity in the east-west propagation is through variations in H. A negative wind curl, for example, increases H through Ekman pumping so that the phase speed is larger than in the linear case. The main effect of an east-west pressure gradient is through the established Sverdrup balance. Waves slow down or speed up as they travel westward depending on the increase or decrease of H. In our model, this implies an increase in the propagation speed for waves generated south of about 40°N where the east-west averaged pressure gradient is negative.

Westward propagation is evident in the longitude-time plots of ULT displayed in Figures 42a-d. For these figures the remotely forced model was sampled longitudinally at latitudes: 24°N, 33°N, 38°N and 43°N. The ULT values were averaged in space (1/2 degrees) and time (1 month). To avoid the zone of high variability and different dynamics near the coast (i.e. coastally propagating waves and events constrained to a radius of deformation from the boundary), data for the longitude-time plots was extracted starting 3 degrees away from

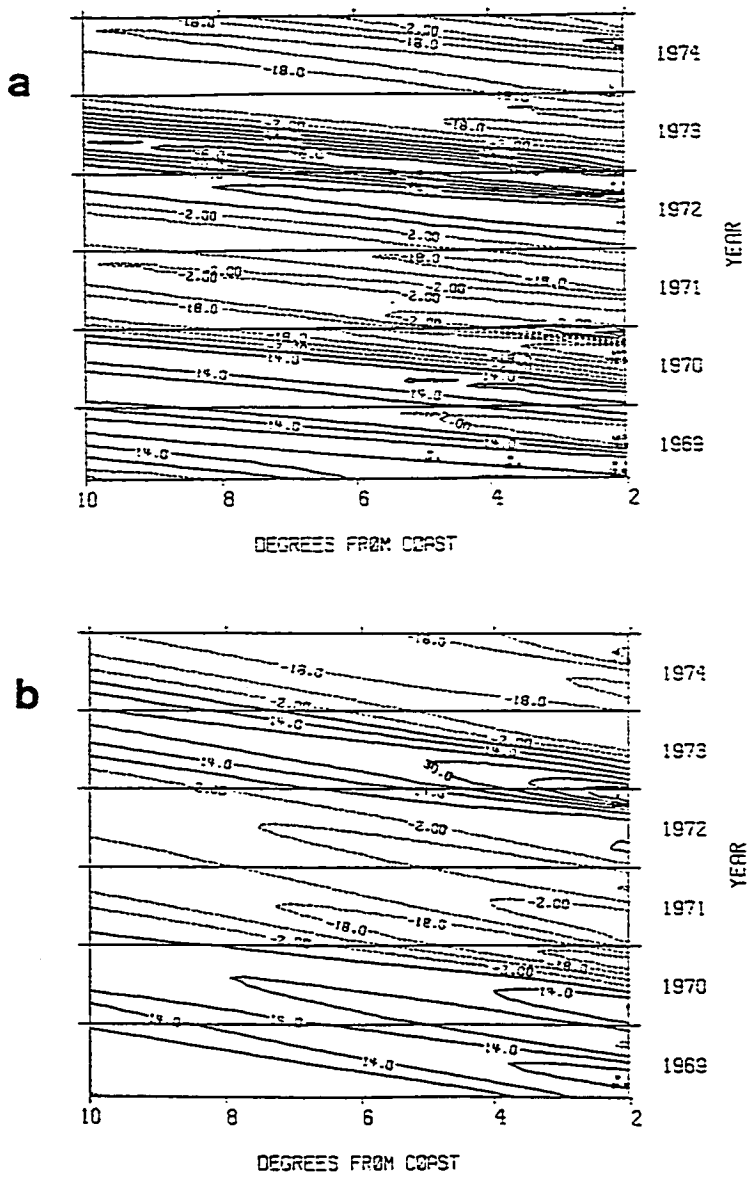

Fig. 42: Longitude-time plot of ULT from the remote model at a) 24°N, b) 33°N, c) 38°N and d) 43°N. Units are meters. Contour intervals are 8m for a and b and 4m for c and d.

c

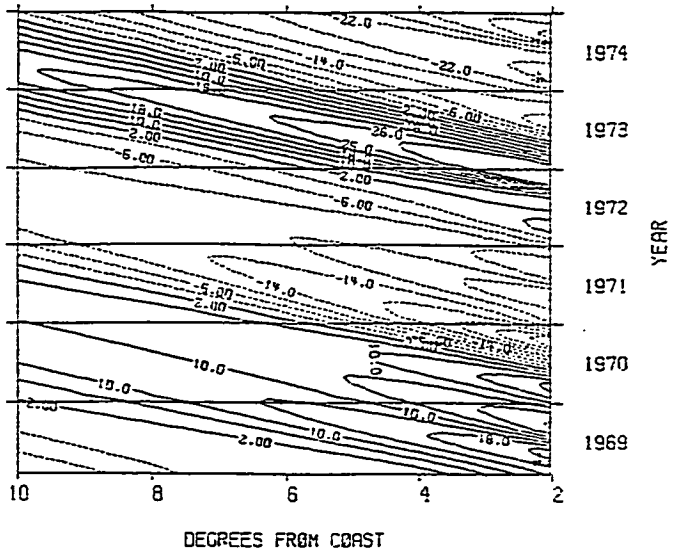
1974
1973
1972
1971
1970
1969
YEAR
10
8
6
4
2
DEGREES FROM COAST

d

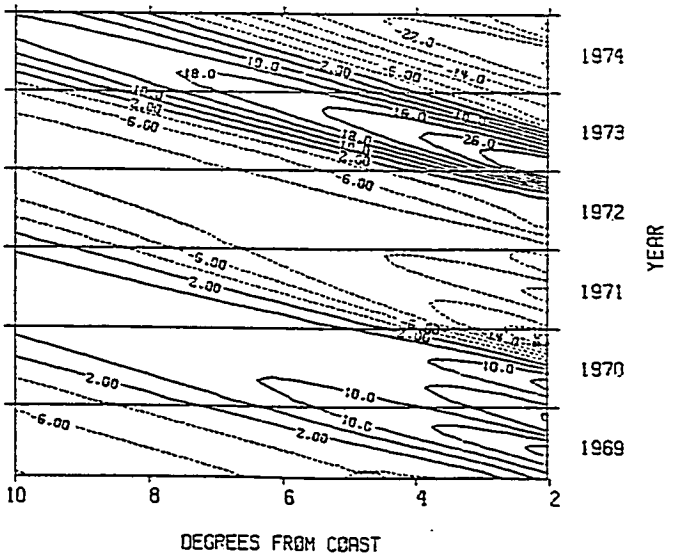
1974
1973
1972
1971
1970
1969
YEAR
10
8
6
4
2
DEGREES FROM COAST

the coast. The period shown (1969-1974) was chosen to emphasize the interannual variation of the data by including the extreme 1969 and 1972 events.

Waves emanating from the coast and going into the interior are clearly shown in Figures 42. The velocity of propagation indicated by the slope of the contours decreases to the north in accordance with eq. 16. Approximate velocities of propagation from Figure 42 are 1.0, .61, .46, and .37 d/m for latitudes 24, 33, 38 and 43°N respectively. These velocities are to be compared to those calculated from eq. 16; using the average ULT for each latitude and $\beta = 2 \times 10^{-1}\ m^{-1}\ s^{-1}$ and g' = .03; the following velocities are obtained: .95, .57, .47, and .41 d/m for 24°, 33°, 38° and 43°N respectively. Also the distance a disturbance travels decreases to the north; this is a direct consequence of travelling at a slower speed and allowing more time for dissipation to take effect.

Although it is possible to distinguish (visually) an annual signal in the data (Fig. 42), it seems that the dominant energy is at lower frequencies. This is in contrast to the strong energy at the annual and semiannual frequency found at the coast (eg. Figs. 34-37). Clarke (1983) has shown that at a given latitude, coastal sea level field can attain characteristics of both Kelvin poleward propagating and Rossby westward propagating waves depending on their frequencies. This could explain the dominance of the low frequencies away from the coast, in spite of the fact that at the coast a large

percentage of the energy is at the annual frequency.

Wave number frequency spectrum (WFS) of ULT for the three models are presented in Figures 43-46. The spectrum were constructed from longitude-time matrices like those shown in Figs. 42 (i.e. at latitudes 24°, 33°, 38° and 43°N) after normalization by the root mean square (RMS). Due to lateral friction, the amplitude of the disturbances decreases as they propagate westward; normalization is needed to eliminate spatial changes in variance prior to computing the WFS (eg. White and Tabata, 1986). Figure 43a, 43b, and 43c are (the logarithm of) WFS at latitude 24°N for the local, remote, and local+remote models respectively. Similarly, Figures 44, 45, 46 are the WFS for latitudes 33°, 38°, and 43°N respectively. To avoid spurious contributions from the initial unspun-up north-western region, only the last 15 years were used. Two-dimensional FFT and Hanning smoothing in frequency were used to calculate the spectrum estimates. On each WFS plot, the theoretical Rossby wave dispersion curve (eq. 14b) for the corresponding latitude and average ULT was drawn.

At all latitudes and for the three models (1+R, R and 1), the WFS is dominated by a low frequency-small wavenumber band contribution and a distinctive and smaller peak at the annual frequency (Fig. 43-46). The relative importance of each one changes with latitude and from model to model. At latitude 24°N, for example, the 1+R model shows two distinctive peaks (Fig. 43a): one at the low frequency-small

Fig. 43: Frequency-wavenumber spectra (FWS) for transect at 24°N. a) FWS from local model, b) FWS from remote model and c) FWS from local+remote model. The theoretical Rossby wave dispersion curve for each model is drawn on the figures. The average ULT for each model was used to calculate the theoretical dispersion curves.

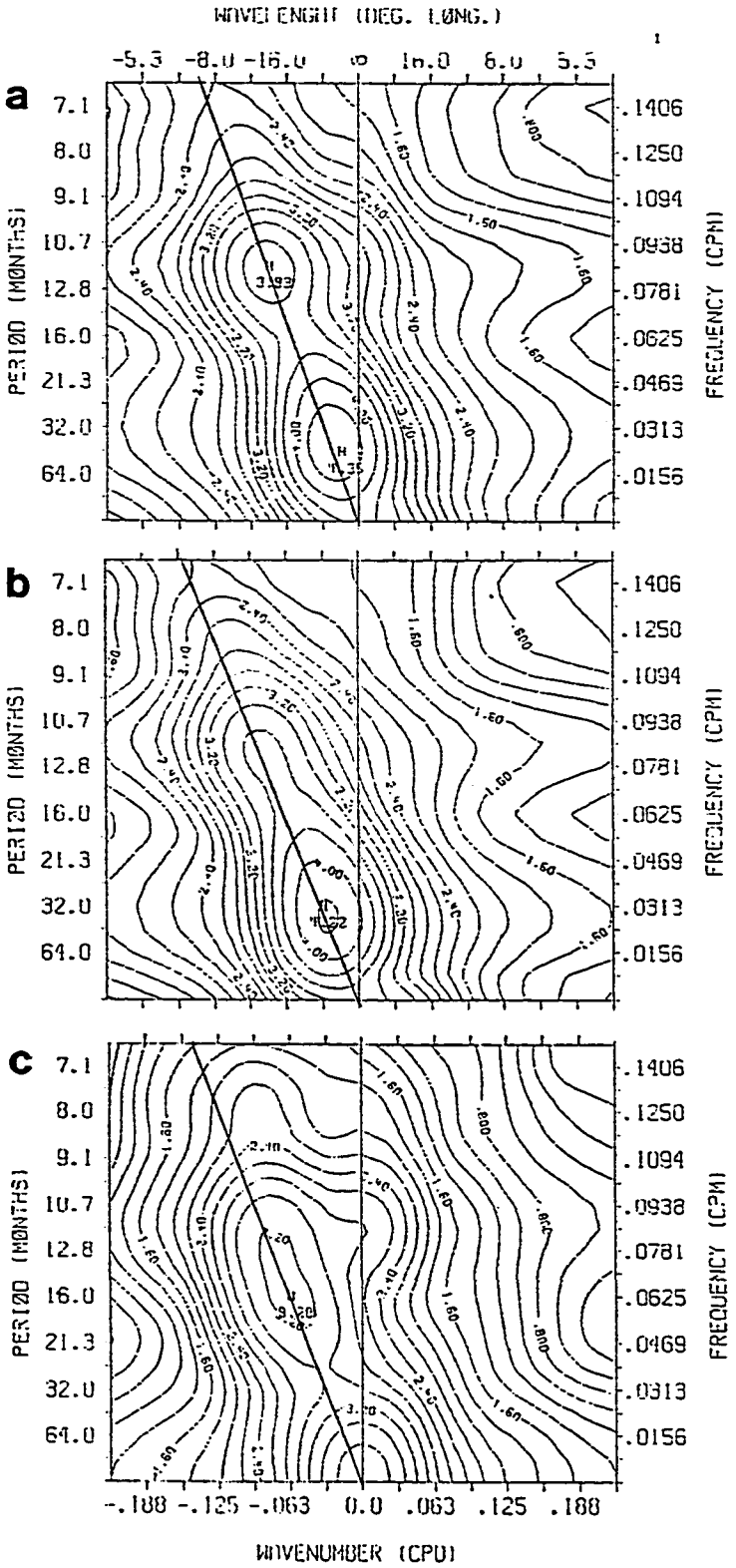
WAVELENGTH (DEG. LONG.)
-5.3 -8.0 -16.0 ∞ 16.0 8.0 5.3
a
b
c
PERIOD (MONTHS)
7.1
8.0
9.1
10.7
12.8
16.0
21.3
32.0
64.0
FREQUENCY (CPM)
.1406
.1250
.1094
.0938
.0781
.0625
.0469
.0313
.0156
-.188 -.125 -.063 0.0 .063 .125 .188
WAVENUMBER (CPD)

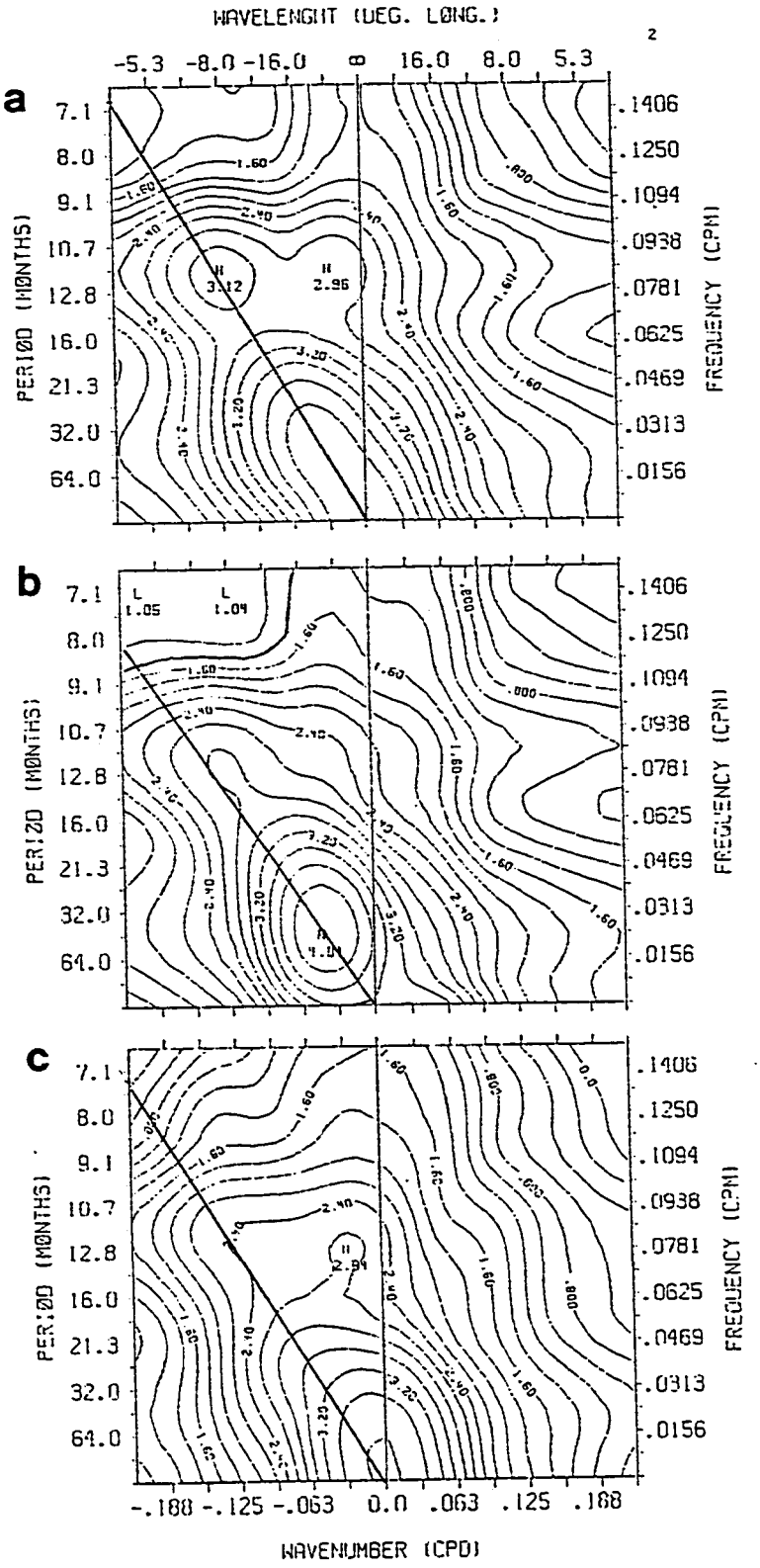

Fig. 44: Same as Fig. 43 but for transect at 33°N.

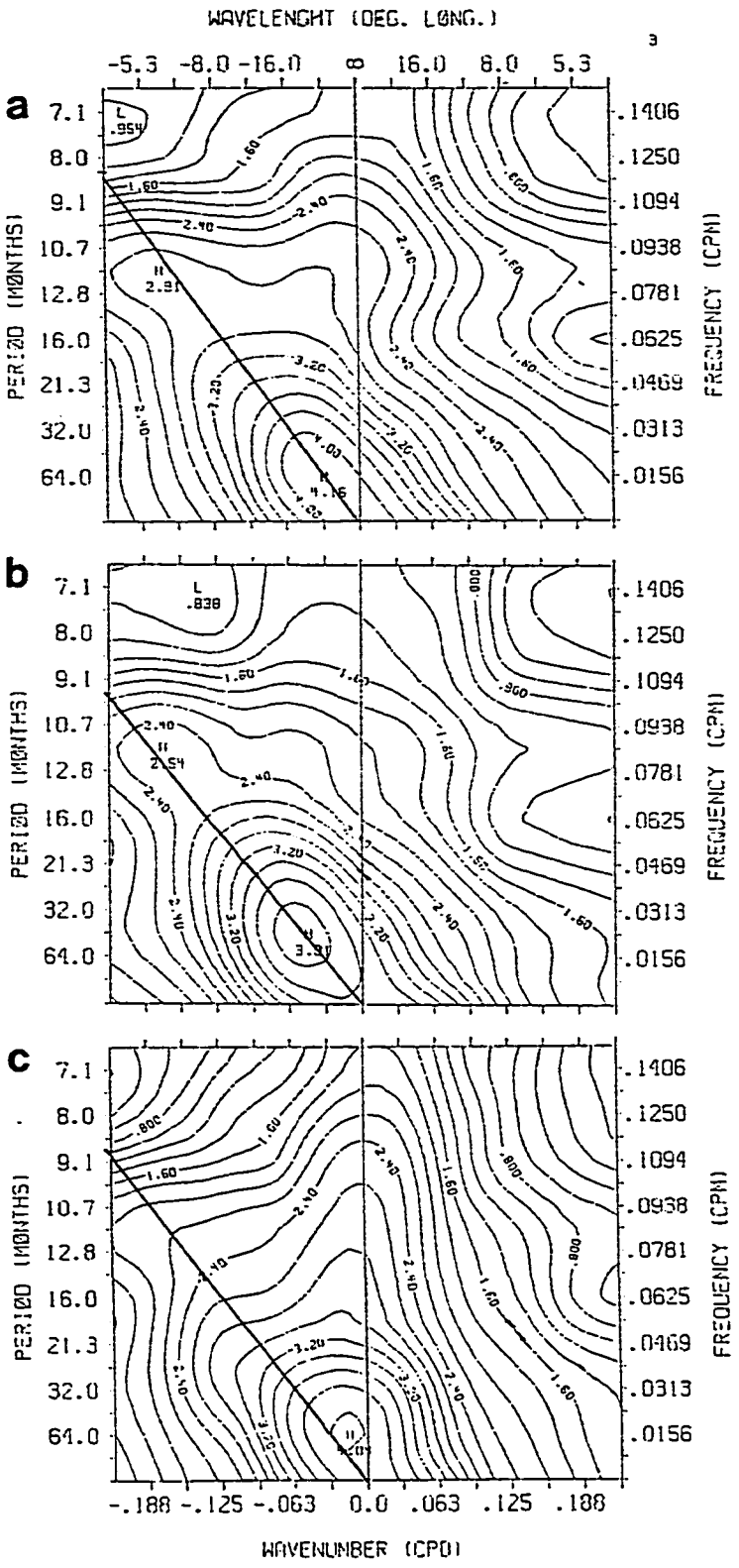

Fig. 45: Same as Fig. 43 but for transect at 38°N.

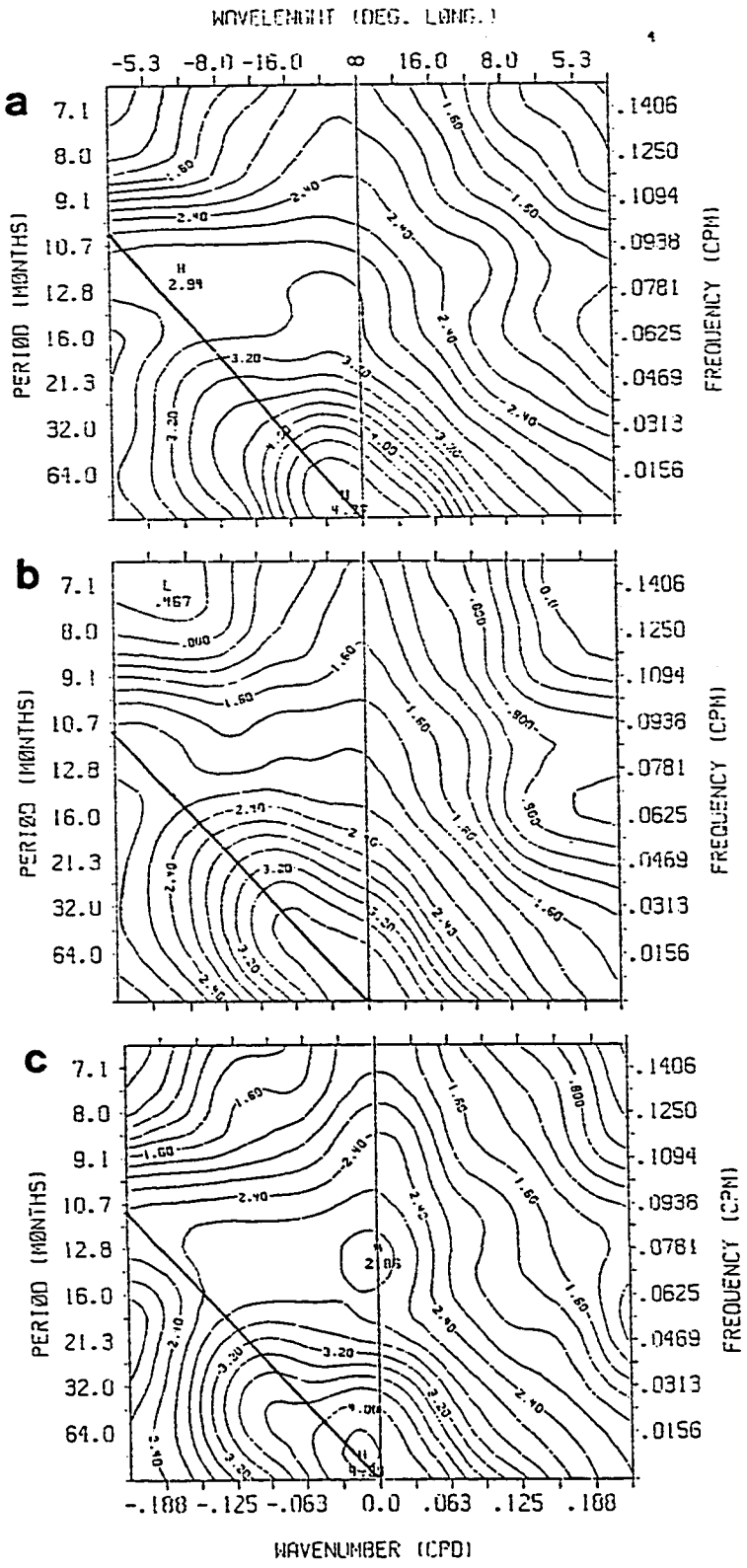

Fig. 46: Same as Fig. 43 but for transect at 43°N.

wavenumber range (64-25 months: ∞ - 16 degrees) that can be identified with El Niño activity and one around the annual frequency (10 - 14 months: 16-9 degrees). For this latitude it seems that a larger amount of the energy in the El Niño band is due to the contribution from the remote model (Fig. 43b) compared to that of the local model (Fig. 43c). For the annual peak the contributions from the local and remote models are of comparable magnitude. The same conclusion can be drawn from the 33° latitude WFS (Fig. 44). For the two northernmost sections (Fig. 45 and 46) the contribution to the El Niño peak comes from both the local and remote model at similar proportions.

The amount of energy in the low frequency band available at the coast that was contributed from the remote model is at least an order of magnitude bigger than that contributed by the local model (eg. Fig. 34). The fact that the WFS shows similar magnitudes for the local and remote models indicates that the former is more efficient in radiating the energy westward, i.e. wind induced current reversal (eg. Mysak, 1983) and/or direct wind curl forcing at the coast (eg. White, 1985) is a more efficient mechanism at producing westward propagating disturbances than poleward propagating Kelvin waves, although the total energy is the sum of both mechanism.

It is clear from the WFS plots that most of the model's ocean interior response is in the form of westward (negative wavenumber) propagating Rossby waves. This is demonstrated by the maximum

spectral energy occurring mostly along the Rossby wave dispersion curve. For example, at latitude 24°N, (Fig. 43) the annual peak has an associated wavelength between 11-16 degrees of longitude, while for the same model at latitude 38°N (Fig. 45) the annual peak is shifted in the negative wavenumber direction to a corresponding 6-5 degrees wavelength. These values give an approximate wave speed of about 12.8 degrees/year and 5.8 degrees/year at 24°N and 38°N respectively. The pattern of maximum energy along the Rossby wave dispersion curve is common to the three models. This indicates that once a disturbance is generated at a given latitude, either by coastally propagating waves (remote model) or by wind stress curl at the boundary (local model), at least some of its energy is propagated to the model interior in the form of Rossby waves.

A conspicuous exception to the above described pattern is the peak at the annual frequency at a wavelength longer than that dictated by Rossby wave dynamics. This peak is more evident at the 38°N plot (Fig. 45), but it is also present at the 33° and 43°N plots (Fig. 44-46). For the 24°N plot it becomes indistinguishable from the Rossby wave annual peak. Variability at this frequency-wavenumber range is most probably imposed directly by the local wind stress curl. The very small wavenumber indicates a large scale phenomenon in the longitudinal sense, and, since it is present at all latitudes, it is probably the result of a global annual variation in the wind forcing. For the 33° and 43° sections it is more evident in the WFS

plots that the contribution to this secondary annual peak (non-Rossby wave) is due to the local model.

V. SUMMARY OF RESULTS

A reduced gravity model that incorporates the geometry of western North America has been used to study the dynamics of the California Current System (CCS). Three experiments were implemented: first the model was run using 19 years of wind stress from the Comprehensive Ocean-Atmosphere Data Set (local model); a second experiment (remote model) consisted of forcing the model through its southern boundary using the results of a similar reduced gravity equatorial model; in a third experiment, both forcings were used simultaneously (local+remote model). The main objective of this work was to analyze the low frequency variability on the CCS in terms of its contributions from remote and local forcing.

Several aspects of the large scale circulation are reproduced by the model. Away from the coast, the basic state is determined by the predominantly negative wind curl. The model is in Sverdrup balance, i.e. the negative wind curl is compensated by an east to west pressure gradient that geostrophically drives an equatorward current. The main part of the California Current can be identified with this mechanism.

For the local model, Ekman on-offshore transport driven by alongshore winds largely dominates the dynamics near the coast. Seasonal variations on the strength and direction of the winds determine the annual ULT variability there. During spring and summer,

strong northwesterly winds drive an offshore Ekman transport that causes the model pycnocline to become shallow near the coast. Associated equatorward geostrophic currents develop reinforcing the larger scale (Sverdrupian) equatorward California Current. Weakening of the alongshore winds and actual reversal north of 40° during fall and winter cause the upwelling region near the coast to relax and the coastal countercurrent to develop.

Crosscorrelation analysis shows that the ULT signal in the local model slowly propagates from south to north at a speed too slow to represent first baroclinic Kelvin waves. It is shown that this motion is in direct response to wind pattern poleward propagation. On the other hand, several features of the ULT-wind correlation analysis suggest that the maximum response in the ULT signal occurs later in time and several hundred kilometers poleward from those of the wind events. This later phenomenon has been identified as evidence of coastal wave propagation (eg. Halliwell and Allen, 1984).

For the remote model, most of the response along the boundary corresponds to poleward propagating waves. Upwelling and downwelling events and associated geostrophic currents succeed each other appearing at the southern boundary and propagating along the coast with the speed and offshore scale characteristics of coastally trapped first baroclinic Kelvin waves.

Time series of sea level data from San Diego, San Francisco, Crescent City and Neha Bay were used to validate the model. There is

good visual correlation between the sea level time series and the scaled model ULT. By separating the low and high frequency information for each model, we were able to determine that most of the correlation in the large time scale (El Niño time scale) is due to the signal coming from the equator propagated to the region in the form of coastally trapped Kelvin waves. On the other hand, both models (remote and local) are responsible for the model-observation correlation at the annual frequency.

Spectral and crosspectral analysis were used to quantitatively corroborate the visual comparison. As expected, time series from the wind forced model are very well correlated (high coherence square) with observed sea level data at the annual frequency but poorly correlated at low frequencies. For the remote model, the coherence is low (but significant) at the annual frequency, but high at the low frequencies, which strongly suggests that most of this energy is of equatorial origin. The remote model explains more than 75 percent of the variance in the low frequency sea level variability at San Diego and San Francisco. For the two northernmost stations, the coherence between remote model and observations diminishes for the El Niño band while the local-observations coherence at the annual frequency increases.

Wavenumber-frequency spectrum is used to investigate the mesoscale variability in the model interior. The spectrums are dominated by two maxima: one at the low frequency-small wavenumber

end and another at the annual frequency. The ridge of maximum energy lies along the theorectical Rossby wave dispersion curve for all three models, which indicates that most of the ULT variability in the model interior can be associated with westward propagating first baroclinic Rossby waves emanating from the eastern boundary. The spectra also shows a secondary peak at the annual frequency that is not related to Rossby wave activity. It seems that this secondary maximum is a direct response to wind forcing at that frequency.

VI. DISCUSSIONS AND CONCLUSIONS

The results presented in this thesis have demonstrated that a significant amount of the sea level interannual variability in the California current region can be explained by the poleward propagation of Kelvin waves along the coast. This work supports the hypothesis of an oceanic teleconnection as the principal mechanism for the co-occurrence of tropical and mid-latitude El Niño phenomena.

The effect of a basin-wide enhancement of the atmospheric circulation during a tropical warming event (atmospheric teleconnection) is recognized as an important mechanism for augmenting the basic response. However, this later effect is thought to be more important for the annual time scale than for the interannual (El Niño variability) (see Figs. 31 and 33).

It seems plausible for the local wind driven contribution to become the dominant force for specific events. Simpson (1983, 1984a, b), for example, argued that for the 1982-83 event, the observations are incompatible with most of the requirements of the theory of coastally trapped waves. Other authors (eg. Huyer and Smith, 1985; Rienecker and Mooers, 1986) have concluded that, though the initial signals of 1982-83 northeastern El Niño arrived by an oceanic path, the initial effects were greatly enhanced by anomalous local atmospheric conditions.

Huyer and Smith concluded that the manifestation of the 1982-83

El Niño off Oregon was associated with both distant and local causes. They show that the atmospheric forcing became anomalous only after (2-3 months) the initial high sea level developed.

One of the main objections to the oceanic teleconnection hypothesis is the small cross-shelf length scales of the coastal waves (≈ 35km). Anderson and Rowlands (1976) theoretical work demonstrated how planetary waves lead to a westward broadening of the upwelling fields. Philander and Yoon (1982) showed that for long periods (> 200 days) the appropriate offshore scale is not the radius of deformation but the distance a Rossby wave travels in a given time.

Our results reflect this condition. Once an upwelling (or downwelling) event has propagated poleward along the coast, a westward shedding of energy occurs (Figs. 13, 23a, 23b). This causes, first, a broadening of the area of influence of the coastal phenomenon and, second, an actual export of energy to the model interior. The time scales of these two phenomena are very different. Coastal propagation time scales are of the order of days, while the broadening of the coastal disturbance by planetary waves is of the order of months (Philander and Yoon, 1982). This latter is certainly fast enough to influence the coastal low-frequency El Niño events (2-5 years).

The remote model does not completely determine the model variability. In fact, besides the low frequency coastal variations, most of the model response, including the long term average circulation and the annual variability at the coast (and at the

interior), is determined by the local model through the curl of the wind stress and the variability of the alongshore winds.

The resulting long term average ULT and geostrophic currents are encouraging. A very realistic current structure develops in which a Sverdrup balance is established. The main geostrophic equatorward currents dominate the response away from the coast. The model reproduces several peculiar features of the geostrophic circulation, most conspiciously the shoreward sweep of the southeastward flowing waters at about 32°N (see Fig. 9). This feature, observed by Reid and Schwartzlose (1963) and described by Pavlova (1966), consists of a permanent shoreward bend in the main southward flowing current near 32°N.

Pavlova (1966) suggests that at some distance from the coast, the eastward current divides into a northward component that feeds the California Countercurrent and the southern California eddy and a southward component that is part of the main southward flow (Hickey, 1979). This description could have been drawn from our Fig. 9. Pavlova (1966) speculates about the eastward rotation being caused by features of the bottom topography and to the pattern of prevailing wind along the coast. The fact that our model so consistently reproduces this feature dismisses topography as the main cause (our model does not include any topographic effects), leaving the second explanation as the most probable. In particular it seems that the minimum in the tangential winds (magnitude of the projected winds in

the general direction of the coast), around 34°N due to the westward bend of the coast at the California bight, causes the splitting of the equatorward currents. This is done by abruptly diminishing the large scale Ekman onshore transport and coastal downwelling at the bight.

For the local model, coastal waves propagation seems to be masked by Ekman advection. Crosscorrelation analysis of the ULT signal along the boundary indicates a propagation speed that is too slow for baroclinic Kelvin waves. The ULT signal probably reproduces the propagation of the wind pattern through direct Ekman forcing (see Figs. 17a, 17b). Information in the remote model, on the other hand, propagates poleward freely along the eastern boundary. The speed, as implied by the ULT crosscorrelation matrix (Fig. 22) coincides with the theoretical Kelvin wave speed.

Time-longitude matrices of both the local and remote model clearly show waves emanating from the eastern boundary (Fig. 42). Wavenumber-frequency spectra suggest that most of this energy is associated with long planetary waves, i.e. the ridge of maximum energy in the WFS lies along their theoretical dispersion curve. The phase speed increases with decreasing latitude producing a refraction from the initial direction normal to the coast.

There are two main peaks on the WFS, one at the annual period and one at a period ranging from 2-5 years. This pattern is common to both local and remote models indicating two possible sources for the mesoscale activity at the ocean interior.

Each model seems to contribute a comparable amount of energy to the total WFS. However, as shown in the spectra of the ULT at the coast (Figs. 38-41), the available energy at the low frequencies is at least an order of magnitude higher for the remote model than for the local. This fact suggests the wind driven disturbances as a more efficient mechanism for the generation of low frequency variability at the ocean interior.

Based on the analysis of dynamic thickness series along the Honolulu-San Francisco transect, White and Saur (1983) concluded that the variability south of 30°N was principally due to the effects of sea level changes along the coast, whereas north of it, it may have been principally due to the effect of wind stress curl. Our results are consistent with these findings. It seems that for the two northernmost stations (at 43° and 38°N) the contribution from the wind forced model to the low frequency peak in the WFS is larger than the contribution from the remote model. For the two southern time series (at 24° and 33°N) the opposite is true. The actual difference is not big and may not be significant.

Even though the overall performance of the model is very good and there is a good agreement between observations and model, there are some limitations to this work.

The vertical resolution is poor due to the vertical averaging associated with the reduced gravity equations. This limitation results in one of the main constituents of the California Current

system, i.e. the California undercurrents, which cannot be considered as a separate entity. The influence of the undercurrent, however, in as much as its vertical integrated effect is concerned, is included in the model. In fact, it may be that the somehow longer than observed persistence of the countercurrent in the model is the result of the contribution of what otherwise would be an undercurrent. The mechanism for generation of an undercurrent, i.e. region of positive curl along an eastern boundary (Pedlosky, 1974; McCreary et al., 1987), in our model generates only a countercurrent.

A second limitation is the absence of bottom topography. This suppresses the possibility of having the topographic Rossby wave mode complimenting the internal Kelvin waves along the eastern boundary (eg. Gill and Clarke, 1974; Allen, 1975). Evidence of this hybrid (part Kelvin and part shelf) wave activity in the eastern Pacific has been presented by Clarke (1977), Christensen et al. (1983), and Wang and Mooers (1977) among others. The theory of hybrid waves, however, has been most successfully used in explaining the character of wind-forced variability at much higher frequencies (hours-days) than those considered in this work (seasonal and interannual). It is not clear how much the presence of the shelf and slope would affect the long-scale-low-frequency event we had analyzed.

Large scale topography features like the Mendocino scarpement presumably could influence the response by providing a mean for scatter of poleward propagation waves (eg. Chao et al., 1979; Hsueh,

1980) or by acting as a wave guide (eg. Longuet-Higgins, 1968). The actual result of the above mechanisms would be to diminish the amount of energy transmitted north of Cape Mendocino. This could be the reason why the magnitude of the interannnual signal does not decrease poleward as much as is suggested by the observations, for example in the 1972 event.

The effect of submarine ridges and valleys on the upwelling pattern was demonstrated in a numerical study by Peffley and O'Brien (1976). They show that bottom relief can be important in causing localized upwelling.

REFERENCES

Allen, J. S., 1975: Coastal trapped waves in a stratified ocean, Journal of Physical Oceanography, 5, 300-325.

Allen, J. S. and D. W. Denbo, 1984: Statistical characteristics of the large scale response of coastal sea level to atmospheric forcing, Journal of Physical Oceanography, 14, 1079-1094.

Anderson, D. L. T., and P. B. Rowlands, 1976: The role of inertia-gravity and planetary waves in the response of a tropical ocean to the incidence of an equatorial Kelvin wave on a meridional boundary, Journal of Marine Research, 34, 295-312.

Anderson, D. L. T. and A. E. Gill, 1975: Spin-up of a stratified ocean with applications to upwelling, Deep-Sea Research, 22, 583-596.

Bang, N. D. and W. R. H. Andrews, 1974: Direct current measurements of a shelf-edge frontal jet in the southern Beonguela system, Journal of Marine Research, 32, 405-417.

Bendat, J. S. and A. G. Piersol, 1971: Random data: Analysis and Measurement Procedures, Wiley-Interscience, New York, N.Y.

Bjerkness, J., 1966: A possible response of the atmospheric Hadley circulation to equatorial anomalies in ocean temperature, Tellus, 18, 820-829.

Brink, K. N., 1987: Coastal ocean physical processes, Reviews of Geophysics, 25, 204-216.

Camerlengo, A. L. and J. J. O'Brien, 1980: Open boundary conditions in rotating fluids, Journal of Computational Physics, 35, 12-35.

Chao, S-Y., J. Pietrafesa and G. S. Janowitz, 1979: The scattering of continental shelf waves by an isolated topographic irregularity, Journal of Physical Oceanography, 9, 687-695.

Chelton, D. B. and R. E. Davis, 1982: Monthly mean sea level variability along the west coast of North America, Journal of Physical Oceanography, 12, 757-784.

Christensen, N., R. De La Paz and G. Gutierrez, 1983: A study of sub-inertial waves off the west coast of Mexico, Deep-Sea Research, 30, 835-850.

Clarke, A. J., 1977: Observational and numerical evidence for wind-forced coastal trapped long waves, Journal of Physical Oceanography, 7, 231.

Clarke, Allan J., 1983: The reflection of equatorial waves from oceanic boundaries, Journal of Physical Oceanography, 13, 1193-1207.

Cummins, P. F., L. A. Mysak and K. Hamilton, 1986: Generations of annual Rossby waves in the North Pacific by the wind stress curl, Journal of Physical Oceanograpy, 16, 1179-1189.

Emery, W. J. and K. Hamilton, 1985: Atmospheric forcing of interannual variability in the Northeast Pacific Ocean: Connections with El Niño, Journal of Geophysical Research, 90, 857-868.

Emery, W. J. and L. Magaard, 1976: Baroclinic Rossby waves as inferred from temperature in the eastern Pacific, Journal of Marine Research, 34, 365-385.

Enfield, D. B. and J. S. Allen, 1980: On the structure and dynamics of monthly mean sea level anomalies along the Pacific coast of North and South America, Journal of Physical Oceanography, 10, 557-578.

Gill, A. E., 1982: Atmosphere-Ocean Dynamics, 30, Academic Press, International Geophysics Series, London, 662 pp.

Gill, A. E. and A. J. Clarke, 1974: Wind-induced upwelling, coastal current and sea level changes, Deep Sea Research, 21, 325-345.

Halliwell, G. R. and J. S. Allen, 1984: Large-scale sea level response to atmospheric forcing along the west coast of North America, summer 1973, Journal of Physical Oceanography, 14, 864-886.

Halliwell, G. R. and J. S. Allen, 1987: The large-scale coastal wind field along the west coast of North America, 1981-1982, Journal of Geophysical Research, 92, 1861-1884.

Hickey, B. M., 1979: The California current system - hypothesis and facts, Progress in Oceanography, 8, 279 pp.

Huyer, A. and R. L. Smith, 1985: The signature of El Niño off Oregon, 1982-1983, Journal of Geophysical Research, 90, 7133-7142.

Hurlburt, H. E., and J. D. Thompson, 1973: Coastal upwelling on a beta-plane, Journal of Physical Oceanography, 3, 16-32.

Hsueh, Y., 1980: Scattering of Continental shelf waves by longshore variations in bottom topography, Journal of Geophysical Research, 85, 1147-1150.

Killworth, P. D., 1979: On the propagation of stable baroclinic Rossby waves through a mean shear flow, Deep-Sea Research, 26A, 997-1031.

Longuet-Higgins, M. S., 1968: Double Kelvin waves with continuous depth profiles, Journal of Fluid Mechanics, 34, 49-80.

Luther, M. E. and J. J. O'Brien, 1985: A model of the seasonal circulation in the Arabian Sea forced by observed winds., Progress in Oceanography, 14, 353-385.

McCreary, J., 1976: Eastern tropical ocean response to changing wind stress systems: with application to El Niño, Journal of Physical Oceanography, 6, 632-649.

McCreary, J. P., P. K. Kundu and S. Chao, 1987: On the dynamics of the California Current System, Journal of Marine Research, 45, 1-32.

Moore, D. W., 1968: Planetary-gravity waves in an equatorial ocean, Ph.D. dissertation, Harvard University, Cambridge, MA, 207 pp.

Moore, D. W. and S. G. Philander, 1977: Modelling of the tropical ocean circulation, The Sea, 6, E. D. Goldberg and Co-Editors, Wiley-Interscience.

Munk, W. H., 1980: On the wind-driven ocean circulation, Journal of Meteorology, 7, 79-93.

Mysak, L. A., 1983: Generation of annual Rossby waves in the North Pacific, Journal of Physical Oceanography, 13, 1908-1923.

Nelson, C. S., 1977: Wind stress and wind stress curl over the California current, NOAA Technical Report NMFS SSRF-714, U.S. Department of Commerce.

Namias, J., 1976: Some statistical and synoptic characteristics associated with El Niño, Journal of Physical Oceanography, 6, 130-138.

Norton, J., D. McLain, R. Brainard and D. Husby, 1985: The 1982-83 El Niño event off Baja and Alta California and its ocean climate context, El Niño North, W. S. Wooster and D. L. Fluharty (Ed.), 313 pp.

Pavlova, Yu. V., 1966: Seasonal variations of the California current, Oceanology, 6, 806-814.

Pearcy, W. G. and A. Schoener, 1986: Changes in the marine Biota coincident with the 1982-83 El Niño in the northeastern subartic Pacific Ocean, Journal of Geophysical Research.

Pedlosky, J., 1974: Longshore currents, upwelling and bottom topography, Journal of Physical Oceanography, 4, 214-226.

Peffley, M. B. and J. J. O'Brien, 1976: A three-dimensional simulation of coastal upwelling off Oregon, Journal of Physical Oceanography, 6, 164-180.

Philander, S. G. H. and J. H. Yoon, Eastern boundary currents and coastal upwelling, Journal of Physical Oceanography, 12, 862-879.

Price, J. M. and L. Magaard, 1980: Rossby wave analyses of baroclinic potential energy in the upper 500m of the north Pacific, Journal of Marine Research, 38, 249-264.

Quinn, W. H., D. O. Zopf, K. S. Short and R. T. W. Kuo Yang, 1978: Historical trends and statistics of the southern oscillation, El Niño, and Indonesian droughts, Fisheries Bulletin, 76, 663-678.

Reid, J. L., 1962: Measurements of the California countercurrent at a depth of 250m, Journal of Marine Research, 20, 134-137.

Reid, J. L. and A. Mantyla, 1976: The effect of the geostrophic flow upon coastal sea elevations in the northern North Pacific Ocean, Journal of Geophysical Research, 81, 3100-3110.

Reid, J. L. and R. A. Schwartzlose, 1962: Direct measurements of the Davidson Current off Central California, Journal of Geopysical Research, 67, 2491-2497.

Reid, J. L. and R. A. Schwartzlose, 1963: Direct measurements of a small surface eddy off northern Baja California, Journal of Marine Research, 21, 205-218.

Reid, J. L., G. L. Roden and J. G. Wyllie, 1958: Studies of the California Current System, Progress Report, 1 July 1956 to January 1958.

Rienecker, M. M. and C. N. K. Mooers, 1986: The 1982-1983 El Niño signal off northern California, Journal of Geophysical Research, 91, 6597-6608.

Simpson, J. J., 1984a: El Niño-induced onshore transport in the

California current during 1982-83, Geophysical Research Letter, 11, 233.

Simpson, J. J., 1984b: A simple model of the 1982-83 Californian "El Niño", Geophysical Research Letter, 11, 243-246.

Simpson, J. J., 1983: Large-scale thermal anomalies in the California Current during the 1982-1983 El Niño, Geophysical Research Letter, 10, 937-940.

Sverdrup, H. U., M. W. Johnson and R. H. Fleming, 1942: The ocean, their physics, chemistry and general biology, Prentice-Hall, Inc., Englewood Cliffs, N. J., 1087 pp.

Wang, D. P. and C. N. K. Mooers, 1976: Coastal-trapped waves in a continously stratified ocean, Journal of Physical Oceanography, 6, 853-863.

White, W. B., 1985: The resonant response of interannual baroclinic Rossby waves to wind forcing in the eastern midlatitude North Pacific, Journal of Physical Oceanography, 15, 403-415.

White, W. B. and J. F. T. Saur, 1981: A source of annual baroclinic waves in the eastern subtropical North Pacific, Journal of Physical Oceanography, 11, 1452-1462.

White, W. B. and S. Tabata, 1987: Interannual westward-propagating baroclinic long-wave activity on line P in the eastern midlatitude North Pacific, Journal of Physical Oceanography, 17, 385-396.

Wooster, W. S. and David L. Fluharty, 1985: El Niño North: Niño

effects in the eastern subartic Pacific Ocean, Washington Sea Grant Prog., Univ. Wash., Seattle, WA, 313 pp.

Wooster, W. S. and Reid, J. L., 1963: Eastern boundary currents, The Sea, (M. N. Hill, ed.), 2, Wiley-Interscience, New York, pp. 253-280.

APPENDIX A

Values of parameters used in the model.

Name	Symbol	Value
Radius of earth	a	6.3784×10^6 m
Coefficient of Eddie Viscosity	A	350 m^2/s
Drag Coefficient	C_D	1.5×10^{-3}
Reduced Gravity	g'	.03 m/s^2
Initial Lager Depth	H	200m
Time Step	Δt	20 minutes
Grid size (Lat. and Long.)	$\Delta\theta, \Delta\phi$ $\Delta\theta, \Delta\phi$	1/12 degrees
Density of Seawater	ρ	1.025×10^3 kg/m^3
Density of Air	ρ_A	1.2 kg/m^3
Earth's Rotation	Ω	$.729 \times 10^{-4}$ s^{-1}